The Planet-Disk Connection: From Protoplanetary Disks to Planetary Atmospheres

Thesis by
Nicole L. Wallack

In Partial Fulfillment of the Requirements for the
Degree of
Doctor of Philosophy

Caltech

CALIFORNIA INSTITUTE OF TECHNOLOGY
Pasadena, California

2022
Defended May 27, 2022

Nicole L. Wallack
ORCID: 0000-0003-0354-0187

ACKNOWLEDGEMENTS

I am truly forever grateful to all of those who have supported me throughout my graduate school journey. I have had the true privilege of being advised by Heather Knutson, whose encouragement and guidance has been incredibly invaluable. Heather is an incredible role model and the type of scientist and mentor that I aspire to be, and I cannot thank her enough. I can say for certain that I would not be where I am now without her incredible support. I also want to thank Dimitri Mawet for advising me through an incredibly vast observing endeavor and for trusting me to lead such a massive undertaking. I also want to thank Geoff Blake for not only chairing my thesis committee, but also for the fascinating and enriching scientific discussions while observing. To the rest of my thesis committee, Yuk Yung and Konstantin Batygin, I greatly appreciate both of your scientific insights and perspectives throughout graduate school. I would also like to thank the GPS Division staff members, especially Julie Lee, Ulrika Terrones, Margaret Carlos, Ruth Loisel, and Loreta Young.

This work would not have been possible without the support of many colleagues and coauthors. I especially want to thank all of the Knutson Group and Exoplanet Technology Laboratory for their insight and wisdom. I have learned so much from you all.

To all of the officemates, friends, and roommates that I've had throughout my time in graduate school, your kindness and friendship has meant the world to me and has made graduate school so special. You all know how much you mean to me.

To my family, especially my parents and brother, I am so lucky to have your incredible and unwavering love and support. This would not have been possible without you.

ABSTRACT

When gas giant planets form, they influence the structure of the surrounding gas disk, which in turn shapes the final compositions of their gas envelopes. My thesis work combines two distinct techniques in order to better understand planet formation and evolution. As a planet accretes its atmosphere, information about its formation history is encoded in its composition (metallicity and C/O ratio). Taking advantage of equilibrium chemistry expectations of carbon bearing molecules for cool ($T_{equ} \lesssim$1000K) planets, in Chapter 2 we probe the atmospheric metallicities of this population of planets using Spitzer secondary eclipses. Expanding this sample set to all short-period gas giant planets with Spitzer thermal emission detections in Chapter 3, we can further explore which system parameters had the most impact on the infrared spectral slopes of these objects. In parallel with these projects, I also carried out a search for planets in protoplanetary disks using direct imaging in Chapter 4. As these planets accrete gas, they also carve out gaps in the protoplanetary disk, leaving hints as to where in the disk they formed. We conducted a multi-year direct imaging survey of more than 40 stars hosting protoplanetary disks in order to detect embedded gas giant planets and better constrain planet-disk interactions. These two approaches represent two distinct, yet complementary, methods of studying the formation histories of giant planets.

PUBLISHED CONTENT AND CONTRIBUTIONS

Wallack, N. L., Knutson, H. A., & Deming, D. (2021). Trends in Spitzer Secondary Eclipses. *The Astronomical Journal*, *162*(1), 36. https://doi.org/10.3847/1538-3881/abdbb2.
N.L.W. reduced and analyzed the data, and wrote the manuscript.

Wallack, N. L., Knutson, H. A., Morley, C. V., Moses, J. I., Thomas, N. H., Thorngren, D. P., Deming, D., Désert, J.-M., Fortney, J. J., & Kammer, J. A. (2019). Investigating Trends in Atmospheric Compositions of Cool Gas Giant Planets Using Spitzer Secondary Eclipses. *The Astronomical Journal*, *158*(6), 217. https://doi.org/10.3847/1538-3881/ab2a05.
N.L.W. reduced and analyzed the data, and wrote the manuscript.

TABLE OF CONTENTS

Acknowledgements iii
Abstract iv
Published Content and Contributions v
Table of Contents v
List of Illustrations vii
List of Tables xix
Chapter I: Introduction 1
Chapter II: Investigating Trends in Atmospheric Compositions of Cool Gas Giant Planets Using *Spitzer* Secondary Eclipses 5
  2.1 Introduction 5
  2.2 Observations and Data Analysis 9
  2.3 Results 19
  2.4 Discussion 21
  2.5 Conclusions 34
  2.6 Appendix 36
Chapter III: Trends in *Spitzer* Secondary Eclipses 49
  3.1 Introduction 49
  3.2 Observations and Data Analysis 52
  3.3 Results 57
  3.4 Discussion 63
  3.5 Conclusions 70
  3.6 Appendix 71
Chapter IV: Survey of Protoplanetary Disks Using the Keck/NIRC2 Vortex Coronagraph 76
  4.1 Introduction 76
  4.2 Observations 78
  4.3 Results 80
  4.4 Discussion 91
  4.5 Conclusions 95
  4.6 Appendix 96
Chapter V: Conclusions 106
Bibliography 108

LIST OF ILLUSTRATIONS

Number *Page*

1.1 A cartoon of the geometry of a transiting planet. A transmission spectrum would be taken when the light from the host star passes through the blue region. Dayside emission spectra would be taken when the red planet passes behind the host star. 3

1.2 Mass versus period by detection method for planets detected via the direct imaging or transit methods according to the NASA Exoplanet Archive. 4

2.1 Phased light curves for each planet from the simultaneous fits with instrumental effects removed. We show data binned in ten-minute intervals (black filled circles) with error bars corresponding to the scatter in each bin, and overplot the best-fit eclipse model in each bandpass for comparison (red lines). The 2σ upper limits for the best-fit eclipse depths of the 3.6 μm and 4.5 μm bandpasses for HAT-P-15b (see Section 2.2 for more details), the 4.5 μm bandpass for HAT-P-17b, and the 3.6 μm bandpass for HAT-P-26b are shown. . . 14

2.2 Posterior probability distribution for the secondary eclipse center time and depth in both bands from a joint fit with a Gaussian prior derived from the RV constraints on the eclipse center time for HAT-P-15b. Contours indicate the 1σ, 2σ, and 3σ bounds on these parameters. . 17

2.3 Posterior probability distribution for the secondary eclipse center time and depth in both bands from a joint fit with a relatively broad uniform prior of -0.07 to 0.07 days on the eclipse center time for HAT-P-18b. Contours indicate the 1σ, 2σ, and 3σ bounds on these parameters, while the red lines show the prior constraints used in our final version of the fits for this planet. 18

2.4 Heat map (left) showing the spectral slope expected for equilibrium chemical models with varying C/O ratios and metallicities for HAT-P-17b. Each black point represents a forward model, where we interpolate between models to generate the heat map. We indicate the region of parameter space consistent with this planet's measured spectral slope at the 2σ level or better with black diagonal lines. The pie charts (right) show the abundances of H_2O, CH_4, CO_2, and CO at a pressure representative of those probed in our observations for select models. 23
2.5 Heat map (left) showing the spectral slope expected for equilibrium chemical models with varying C/O ratios and metallicities for WASP-69b. Each black point represents a forward model, where we interpolate between models to generate the heat map. We show the best-fit value of this planet's measured spectral slope in red and show the region of parameter space consistent at the 1σ level or better with black diagonal lines. The pie charts (right) show the abundances of H_2O, CH_4, CO_2, and CO at a pressure representative of those probed in our observations for select models. 23
2.6 Heat map (left) showing the spectral slope expected for equilibrium chemical models with varying C/O ratios and metallicities for HAT-P-26b. Each black point represents a forward model, where we interpolate between models to generate the heat map. We indicate the region of parameter space consistent with this planet's measured spectral slope at the 2σ level or better with black diagonal lines. The pie charts (right) indicate the relative abundances of H_2O, CH_4, CO_2, and CO at a pressure representative of those probed in our observations for select models. 24
2.7 Comparison of chemical abundances of H_2O, CH_4, CO_2, and CO from the equilibrium chemical models (left) and disequilibrium chemical models (right) for $1\times$ solar metallicity models (top) and $100\times$ solar metallicity models (bottom) all with solar C/O ratios (C/O=0.6) at 130 mbar for our coolest planet, HAT-P-17b. 26

2.8 Comparison of the relative abundances of H_2O, CH_4, CO_2, and CO from the equilibrium chemical models (left) and disequilibrium chemical models (right) for 1$\times$ solar metallicity models (top) and 100$\times$ solar metallicity models (bottom) all with solar C/O ratios (C/O=0.6) at 130 mbar for our hottest planet, HAT-P-26b. 27

2.9 Planet-star flux ratios as a function of wavelength from 1D atmosphere models for all five planets. We show 1$\times$ solar and 100$\times$ solar metallicity models with either efficient (purple and blue, respectively) or inefficient (red and orange, respectively) redistribution of energy to the planet's nightside. Our measured eclipse depths for each planet are shown as black circles, and we plot the corresponding band-integrated flux values from the models as filled squares. For HAT-P-15b (3.6 μm only; see Section 2.2 for more details), HAT-P-17b (4.5 μm only), and HAT-P-26b (3.6 μm only) we show the 2σ upper limit on the eclipse depth. We also overplot the IRAC 3.6 and 4.5 μm response functions in gray in the bottom panel for comparison. 29

2.10 Measured 4.5-3.6 μm brightness temperature ratio as a function of (a) equilibrium temperature, (b) stellar metallicity, (c) planetary mass, and (d) bulk metallicity for all planets with published *Spitzer* eclipse depths and equilibrium temperatures less than 1100 K. We show four planets from this study (HAT-P-17b, HAT-P-18b, HAT-P-26b, and WASP-69b) as well as nine previously published planets (see Table 2.4 for the full list of planets and corresponding references). For planets with no eclipse detected in the 3.6 (4.5) μm bands we plot 2σ lower (upper) limits, respectively. 32

2.11 Measured 4.5 μm to 3.6 μm brightness temperature ratio as a function of stellar metallicity. We create 10^6 simulated data sets by sampling from posterior probability distributions for the reported brightness temperatures and stellar metallicities, and show a random subset of the resulting distribution of linear fits as gray lines. We indicate the median linear solution in red, and plot the corresponding distributions in y intercept and slope below. 35

2.12 Simulated JWST observations of a single secondary eclipse observation of WASP-69b using the NIRSpec G395 grism (black points). We use our best-fit 100× solar metallicity model for this simulation and overplot models with 1×, 3×, 10× and 30× solar metallicities for comparison (all with solar C/O ratios). The IRAC 3.6 and 4.5 μm response functions are shown in gray and our measured eclipse depths in the two *Spitzer* bands are shown as filled black stars. 37
2.13 Raw *Spitzer* photometry for each visit of HAT-P-26b. The normalized flux binned in ten-minute intervals is shown in black and the thirty-second binned flux is shown in gray. Overplotted is the best-fit instrumental model in red. Observations are shown in chronological order across each row. 38
2.14 Raw *Spitzer* photometry for each visit of HAT-P-18b and WASP-69b. The normalized flux binned in ten-minute intervals is shown in black and the thirty-second binned flux is shown in gray. Overplotted is the best-fit instrumental model in red. Observations are shown in chronological order across each row. 38
2.15 Raw *Spitzer* photometry for each visit of HAT-P-15b and HAT-P-17b. The normalized flux binned in ten-minute intervals is shown in black and the thirty-second binned flux is shown in gray. Overplotted is the best-fit instrumental model in red. Observations are shown in chronological order across each row. 39
2.16 Individual light curves for each visit of HAT-P-26b. The ten-minute binned normalized flux in shown in black with error bars showing the standard error of the flux in each bin. The instrumental best-fit parameters are unique to each visit and have been divided out. The red lines are the light curves with the best-fit parameters from the joint fits. Observations are shown in chronological order across each row. The 2σ upper limits for the best-fit eclipse depths of the 3.6 μm visits are shown. 40

2.17 Individual light curves for each visit of HAT-P-18b and WASP-69b. The ten-minute binned normalized flux in shown in black with error bars showing the standard error of the flux in each bin. The instrumental best-fit parameters are unique to each visit and have been divided out. The red lines are the light curves with the best-fit parameters from the joint fits. Observations are shown in chronological order across each row. 41

2.18 Individual light curves for each visit of HAT-P-15b and HAT-P-17b. The ten-minute binned normalized flux in shown in black with error bars showing the standard error of the flux in each bin. The instrumental best-fit parameters are unique to each visit and have been divided out. The red lines are the light curves with the best-fit parameters from the joint fits. Observations are shown in chronological order across each row. The 2σ upper limits for the best-fit eclipse depths of all visits of HAT-P-15b (see Section 2.2 for more details), and the 4.5 μm visits of HAT-P-17b are shown. 42

2.19 Standard deviation of the residuals of each visit of HAT-P-26b after removing the best-fit instrumental and astrophysical models as a function of bin size. The solid lines show the photon noise limits as a function of bin size scaled by $1/\sqrt{N}$. Observations are shown in chronological order across each row. 43

2.20 Standard deviation of the residuals of each visit of HAT-P-18b and WASP-69b after removing the best-fit instrumental and astrophysical models as a function of bin size. The solid lines show the photon noise limits as a function of bin size scaled by $1/\sqrt{N}$. Observations are shown in chronological order across each row. 43

2.21 Standard deviation of the residuals of each visit of HAT-P-15b and HAT-P-17b after removing the best-fit instrumental and astrophysical models as a function of bin size. The solid lines show the photon noise limits as a function of bin size scaled by $1/\sqrt{N}$. Observations are shown in chronological order across each row. 44

2.22 Mixing ratio profiles derived using the same framework as presented in Moses et al. (2011), Moses, Line, et al. (2013), and Moses et al. (2016) for relevant species of interest for a 1× solar metallicity equilibrium (solid lines) and disequilibrium (dashed lines) model with solar C/O ratios for HAT-P-17b. 45

2.23 Mixing ratio profiles derived using the same framework as presented in Moses et al. (2011), Moses, Line, et al. (2013), and Moses et al. (2016) for relevant species of interest for a 100× solar metallicity equilibrium (solid lines) and disequilibrium (dashed lines) model with solar C/O ratios for HAT-P-17b. 46

2.24 Mixing ratio profiles derived using the same framework as presented in Moses et al. (2011), Moses, Line, et al. (2013), and Moses et al. (2016) for relevant species of interest for a 1× solar metallicity equilibrium (solid lines) and disequilibrium (dashed lines) model with solar C/O ratios for HAT-P-26b. 47

2.25 Mixing ratio profiles derived using the same framework as presented in Moses et al. (2011), Moses, Line, et al. (2013), and Moses et al. (2016) for relevant species of interest for a 100× solar metallicity equilibrium (solid lines) and disequilibrium (dashed lines) model with solar C/O ratios for HAT-P-26b. 48

3.1 Raw *Spitzer* photometry for each visit of HAT-P-5b, HAT-P-38b, WASP-7b, WASP-72b, and WASP-127b. The normalized flux binned in 5 minute intervals is shown as black filled circles and the 30 second binned flux is shown as gray filled circled. The best-fit instrumental model is overplotted in red. Observations of HAT-P-38b are shown chronologically down each column. 58

3.2 Normalized light curves for each visit of HAT-P-5b, HAT-P-38b, WASP-7b, WASP-72b, and WASP-127b from the simultaneous fits with instrumental effects removed. We show data binned in five-minute intervals (black filled circles) with error bars corresponding to the scatter in each bin divided by the square root of the number of points in each bin, and we overplot the best-fit secondary eclipse model in red. Observations of HAT-P-38b are shown chronologically down each column. The 2σ upper limits for the best-fit eclipse depths of the 4.5 μm visits of HAT-P-38b and the 3.6 μm visit of WASP-72b are shown. 59

3.3 Band-averaged light curves for HAT-P-38b from the simultaneous fits with instrumental effects removed. We show data binned in five-minute intervals (black filled circles) with error bars corresponding to the scatter in each bin divided by the square root of the number of points in each bin, and overplot the best-fit eclipse model in each bandpass for comparison (red lines). The 2σ upper limit for the best-fit eclipse depth of the 4.5 μm data is shown. 60

3.4 Standard deviation of the residuals as a function of bin size after removing the best-fit instrumental and astrophysical models. The solid lines show the predicted photon noise limit as a function of bin size, which follows a $1/\sqrt{N}$ scaling. Observations of HAT-P-38b are shown chronologically down each column. 61

3.5 Left: Measured 4.5 μm brightness temperature versus 3.6 μm brightness temperature for the sample of all planets with published detections in both bands as well as three new planets from this study. Planets with blackbody-like spectra will lie close to the black dashed line, which corresponds to a 1:1 brightness temperature ratio in the two bands. We highlight points that deviate from this line by greater than 3σ (i.e., planets with non-blackbody emission) with black outlines. The color of the points indicates the predicted equilibrium temperature assuming efficient day-night circulation and zero albedo. Right: The error weighted average of the brightness temperatures measured in the 3.6 μm and 4.5 μm bandpasses versus the predicted equilibrium temperature. Planets that deviate by more than 3σ from the dashed black line (the expected brightness temperature for efficient heat recirculation and zero albedo) are outlined in black. 64

3.6 Change in 3.6−4.5 μm slope as a function of equilibrium temperature, where slopes have been normalized by the equilibrium temperature to keep the scale consistent across the full temperature range. The best fit linear trend is overplotted as a red line with a random sampling of the fit lines from the Monte Carlo shown as gray lines (see §3.4 for a description of the Monte Carlo simulations). 67

3.7 The difference in the two bandpasses, each normalized by equilibrium temperature, versus the planet gravity, divided into temperature bins. The red lines are the best fit from the Monte Carlo simulations and a random sampling of the fit lines from the Monte Carlo are shown as gray lines (see §3.4 for a description of the Monte Carlo simulations). 68

3.8 The difference in the two bandpasses, each normalized by equilibrium temperature, versus the stellar metallicity, divided into temperature bins. The red lines are the best fit from the Monte Carlo simulations and a random sampling of the fit lines from the Monte Carlo are shown as gray lines (see §3.4 for a description of the Monte Carlo simulations). 69

4.1 Optimal contrast curves for our sample of protoplanetary disks colored by L′ magnitude. Each line is the most optimal 5σ contrast for a different disk. 81

4.2 A comparison of the contrasts achieved using the `pyKLIP` and `VIP` reductions. The solid lines are the median contrasts of all of the contrast curves and the shaded regions represent the range of contrasts. We use ADI for the `pyKLIP` reductions and a combination of ADI and RDI for the `VIP` reductions. 82

4.3 Comparison of the planet-to-star flux ratio of the point sources in Figure 4.11 determined from the `VIP` reductions versus the planet-to-star flux ratio in the same location in the `pyKLIP` reductions. A perfectly consistent flux ratio is designated by the dotted line. 84

4.4 The disks in our survey that show evidence of structure which is indicative of scattered light disks. We show the 1σ (solid lines), 2σ (dashed lines), and 3σ (dotted lines) ALMA contours (from references in Table 4.1) overlaid on our 3.8 micron images for reference. North is up and east is left in all of the images. We show the reduction method and number of principal components that optimizes the appearance of the extended structure. 86

4.5 We show a comparison of the mass estimates from the ALMA data and our observational mass limits for the subset of our systems observed as part of the DSHARP Survey (Andrews et al., 2018) or the survey of the Taurus star-forming region (Long et al., 2018). We show the ALMA derived planet masses (in M_{Jup}) as the points with the mass estimates derived using the AMES-Cond models from our 5σ contrast limits shown as the orange bars for each observed gap from the ALMA data (specified in au as the numbers above each system designation). The lengths of the bars incorporate the 1σ uncertainties on the ages, stellar host magnitudes, and distances. The ages for Elias 2-20 and Elias 2-24 are lower than the youngest age in the grids. Therefore, we show the masses assuming 1 Myr as upper limits to the ages, as younger systems would result in smaller masses. The 1σ lower limit on the age of Elias 2-27 is also lower than the youngest age in the AMES-Cond grid, so we show the 1σ upper limit instead of a bar. We also show the associated masses assuming the AMES-Dusty models when the masses were within the grid in purple. 89

4.6 We show the mass estimates derived from our 5σ contrast limits (in M_{Jup}) in each gap/cavity (specified in au above each system designation) as the bars colored by radial distance from the host star. The lengths of the bars incorporate the 1σ uncertainties on the ages, stellar host magnitudes, and distances. The ages for HL Tau, ISO-Oph 2, and SR 21 are lower than the youngest age in the grids, therefore we show the masses assuming an age of 1 Myr as an upper limit to the ages, as a younger system would correspond to smaller mass. We also show the associated masses assuming the AMES-Dusty models when the masses were within the grid in purple. There is a subset of systems that have estimates of planetary masses not ascertained via the Lodato et al. (2019), S. Wang et al. (2021), and S. Zhang et al. (2018) methods. The putative companion at 15 au in 2MASS J16042165-2130284 is detailed in Canovas et al. (2017), the putative companion at 25 au in CQ Tau is detailed in Wölfer et al. (2021), the putative companion in HD 141569 is detailed in Konishi et al. (2016), and the putative companion in GM Aur at 3 au is detailed in Rice et al. (2003). The putative companions in each of the two gaps in HD 169142 have mass estimates of between 0.1-1M_{Jup} for the inner planet and 1-10M_{Jup} for the outer planet, so we show the upper limits for these masses (Fedele et al., 2017). The putative companion in TW Hya is detailed in Dong and Fung (2017). We show the expected planet masses as the circles. In cases where a planet was hypothesized to be creating the observed substructure, but is not thought to be present in the location of the gap, we designate the location with a star next to the radial location. 91
4.7 Companion mass upper limits as a function of separation (in au) for the systems studied herein which did not have clear locations where a planet would be present. 92
4.8 A map of the average sensitivity of our survey in planet mass (calculated using the AMES-Cond and AMES-Dusty models) versus separation in au calculated using `Exo_DMC` (Bonavita, 2020). 92

4.9 Expected planet masses from S. Wang et al. (2021) (diamonds) and S. Zhang et al. (2018) (circles), using different values for the disk viscosity, α, are shown as black and gray points. We show our planet mass detection limits for comparison using the AMES-Cond and AMES-Dusty models (Allard et al., 2012; Baraffe et al., 2003) for the subset of our systems observed as part of the DSHARP survey (Andrews et al., 2018) or the survey of the Taurus star-forming region (Long et al., 2018). The ages for Elias 2-20 and Elias 2-24 are lower than the youngest age in the grids. Therefore, we show the masses assuming 1 Myr as upper limits to the ages, as younger systems would result in smaller masses. The 1σ lower limit on the age of Elias 2-27 is also lower than the youngest age in the grids, so we show the 1σ upper limit instead of a bar. Otherwise, the lengths of the bars account for the 1σ spread in the mass limits owing to the uncertainties on the system ages, stellar host magnitudes, and system distances. 93

4.10 Upper limits on the mass accretion rates as a function of circumplanetary disk radius, R_{in}, for the subset of our systems observed as part of the DSHARP Survey (Andrews et al., 2018) or the survey of the Taurus star-forming region (Long et al., 2018), derived from Zhu (2015) and determined from our contrast limits (and the AMES-Cond models) and masses from S. Wang et al., 2021 (diamonds) and S. Zhang et al., 2018 (circles) assuming a disk viscosity of α=10^{-3}. . . 95

4.11 Left: Locations of all point sources detected in our observations with SNR >5. The central 0."15 and separations> 1."6 are hatched and represent the regions where we do not search for point sources. Right: A histogram, weighted by area, of the separations of the detected point sources. 100

4.12 Similar to Figure 4.5, but showing the mass estimates derived from our 5σ contrast limits for a number of different system ages for systems observed as part of the DSHARP survey (Andrews et al., 2018) or the survey of the Taurus star-forming region (Long et al., 2018). We show the ALMA derived planet masses (in M_{Jup}) as the points with our mass estimates using the AMES-Cond model shown as bars colored by system age. We specify the radial locations of the gaps that we are probing as numbers (in au) above each system name. There are a number of gaps where the derived masses are outside of the AMES-Cond model grid for certain ages and are therefore not shown. 103
4.13 Similar to Figure 4.6, but showing the mass estimates derived from our 5σ contrast limits for a number of different system ages. We show our mass estimates using the AMES-Cond model as bars colored by system age. We specify the radial locations of the gaps that we are probing as numbers (in au) above each system name. There are a number of ages for the multiple gaps in TW Hya which produce mass limits outside of the AMES-Cond model grid, so we do not show those limits. In cases where a planet was hypothesized to be creating the observed substructure, but is not thought to be present in the location of the gap, we designate the location with a star next to the radial location. 104
4.14 Similar to Figure 4.9, expected planet masses from S. Wang et al. (2021) (diamonds) and S. Zhang et al. (2018) (circles) for the subset of our systems observed as part of the DSHARP survey (Andrews et al., 2018) or the survey of the Taurus star-forming region (Long et al., 2018) calculated using different values for the disk viscosity, α, are shown as black and gray points. We show the planet mass estimates derived from our 5σ contrast limits for comparison using the AMES-Cond models (Baraffe et al., 2003). There are a number of gaps where the derived masses are outside of the AMES-Cond model grid for certain ages and are therefore not shown. 105

LIST OF TABLES

Number *Page*

2.1 System Properties 8
2.2 *Spitzer* Observation Details 11
2.3 Best-fit Eclipse Parameters 20
2.4 Brightness Temperature Ratios 30
3.1 System Properties for New Planets in this Study 51
3.2 *Spitzer* Observation Details 53
3.3 Best Fit Eclipse Parameters 62
3.4 Brightness Temperatures and System Parameters 75
4.1 System Parameters 99
4.2 Observation Log 102

Chapter 1

INTRODUCTION

The Importance of Gas Giant Planets

Gas giant planets leave an indelible fingerprint on the planetary systems in which they form. The most massive planets in a system shape the dynamical evolution and availability of planetary building blocks for all of their sibling planets. The delivery of water to the Earth may be the product of interactions between Jupiter and the solar system's natal disk material, allowing for life on our pale blue dot (Raymond & Izidoro, 2017). Therefore, understanding the formation histories of the most massive bodies in a planetary system can help to paint a more complete picture of the formation histories of all of the planets in a system.

When the first exoplanet (a planet outside of our solar system) around a Sun-like star was discovered in 1995, our understanding of massive planets was forever changed (Mayor & Queloz, 1995). While these first detections were of Jupiter mass planets, they were completely unlike our own Jupiter in many ways. These extrasolar planets, or exoplanets, whizzed around their host stars on orbital periods more akin to Mercury's than to Jupiter's. As a result of their short orbital periods, these exoplanets were not only decidedly hotter than our own Jupiter (and therefore deemed "hot Jupiters"), but also were tidally locked, only showing their host stars the same side, affecting the dynamics and chemistries of their atmospheres (Showman et al., 2015). More than 20 years later, we still do not understand the differences between the formation and migration histories of hot Jupiters and more conventional Jupiter analogues.

Gas Giant Planet Formation

There are thought to be two primary formation mechanisms for gas giant planets. Planets that form via core accretion undergo three different sequential stages of formation (Lambrechts & Johansen, 2012; Pollack et al., 1996). The first stage is when a solid core forms from material present in the disk surrounding the host star. The second stage involves the slow accretion of both solids and gas onto the forming planet. When the mass of the envelope is comparable to the mass of the core, the runaway gas accretion phase begins, and the planet rapidly accretes the majority of its gaseous envelope. While the vast majority of the accreted material is primordial gas from the disk, both upward mixing from the core and late stage accretion of solid material via ablation can drive up the metal content (astronomically defined as species other than hydrogen or helium) of the atmosphere. Due to the radial temperature gradient in a protoplanetary disk (which also changes as a function of time), the locations where different molecular species condense in the disk vary. This means that the relative amounts of different molecules in the gas versus solid phase will vary as a function of location in the disk and time (e.g., Espinoza et al., 2017; Öberg et al., 2011). Therefore, once solids are accreted, the atmospheric composition of a planet can leave a fingerprint as to the local availability of solids while the planet was forming.

The second formation mechanism for gas giant planets, disk instability, involves the rapid collapse of the local disk due to gravitational instability, which forms a giant planet out of the primordial material in the disk (Boss, 1997). This process is only thought to occur in the outer parts of the disk, and is therefore a leading candidate to explain the population of directly imaged planets (Boss, 1998). The atmospheres of planets formed in this way are thought to remain primordial, lacking in metals. Therefore, the atmospheric compositions of these objects can also be used to disentangle different formation pathways.

Atmospheric Characterization of Gas Giants

Most of the currently known exoplanetary systems were detected using the transit technique. This approach allows us to detect planets that pass in front of their host star as seen from the Earth. We can take advantage of this line of sight geometry to also probe the planet's atmosphere. If an exoplanet has an atmosphere, it will appear opaque at some wavelengths and transparent at others. This wavelength-dependent transit depth, also known as a transmission spectrum, allows us to characterize the atmospheric compositions of these planets. However, the ubiquitous presence of clouds in the day-night terminator region, can lead to degeneracies in the interpretations of composition and cloud properties with lower signal-to-noise observations (Benneke & Seager, 2012). Thermal emission spectroscopy provides us with a complementary method for studying transiting planet atmospheres that is not as impacted by clouds (Fortney, 2005). A thermal emission spectrum is taken when the planet passes behind the host star (secondary eclipse), where the star blocks the planet's light. We can use this technique to measure the dayside emission spectra of these tidally locked planets, allowing us to constrain their circulation patterns and day-night temperature contrasts (Figure 1.1). This thesis utilizes mid-infared secondary eclipse measurements using the recently decommissioned *Spitzer Space Telescope*. This telescope observed at wavelengths between 3-24 microns, which are not easily accessible from the ground. Indeed, *Spitzer* provided an invaluable first-look at the primary factors that govern the atmospheric properties of close-in giant planets. In Chapters 2 and 3 of this thesis, we investigate atmospheric constraints on the thermal emission of close-in gas giant exoplanets from *Spitzer* observations.

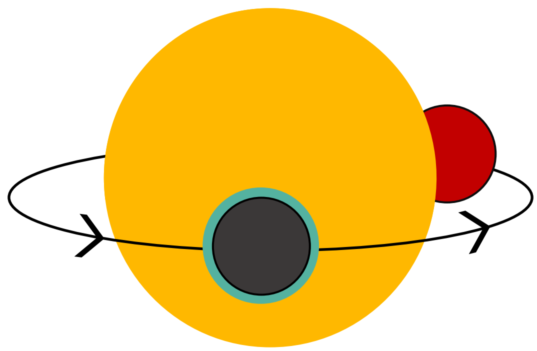

Figure 1.1: A cartoon of the geometry of a transiting planet. A transmission spectrum would be taken when the light from the host star passes through the blue region. Dayside emission spectra would be taken when the red planet passes behind the host star.

Complementary Constraints from Direct Imaging

Direct imaging represents a different, but complementary method of studying exoplanetary systems. This technique seeks to spatially resolve the light from the planet separate from that of its host star and is sensitive to planets on relatively wide orbits as opposed to the close-in transiting planets usually studied in depth using the transit method. The angular resolution of a telescope is directly related to the diameter of its primary mirror, therefore, direct imaging planet searches are generally done using large ground-based facilities such as Keck, Gemini, or the Very Large Telescope. These ground based facilities require adaptive optics systems, which allow for the real-time correction of the effect of the Earth's atmosphere on the observations through the use of deformable mirrors.

Direct imaging searches are typically carried out at near-infrared wavelengths, so they are most sensitive to young, hot gas giant planets that are still radiating away residual heat from their formation. This technique therefore provides an invaluable look at the properties of young planetary systems. Therefore, the direct imaging and transit methods represent complementary ways of understanding different sub-populations of gas giant planets (Figure 1.2).

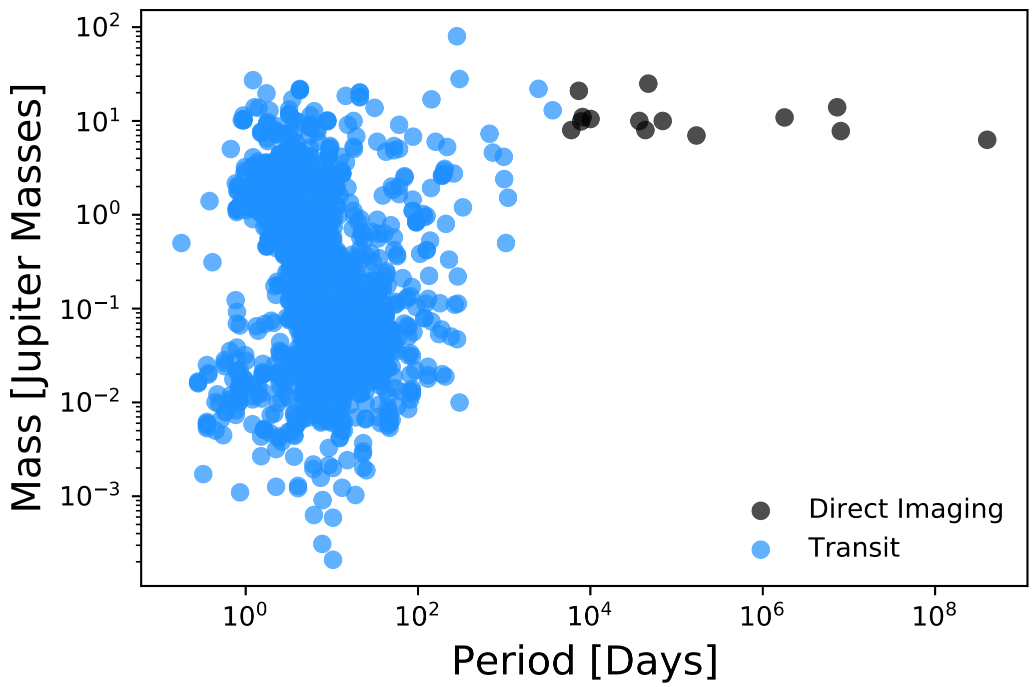

Figure 1.2: Mass versus period by detection method for planets detected via the direct imaging or transit methods according to the NASA Exoplanet Archive.

Because they are also sensitive to the disk structure, direct imaging surveys can also be used to put these young (sometimes still actively accreting their atmospheres) planets into the context of their formation environments. PDS 70 is one of the best-studied examples of this kind of system (Keppler et al., 2018). It contains two wide-separation gas giant planets, one visibly embedded in its natal disk. PDS 70c is still actively accreting its atmosphere, allowing for direct constraints on the accretion rates of forming planets (Benisty et al., 2021; Haffert et al., 2019). There are relatively few systems like this currently known, and in order to better understand this population it is invaluable that we continue to search for and find more young planets through direct imaging. Moreover, gaps in protoplanetary disks seem to be common (eg., Andrews et al., 2018; Long et al., 2018), and if they are caused by young planets, suggest that systems like PDS 70 might be common around young stars. In Chapter 4 of this thesis, we utilize direct imaging in order to place constraints on the masses of planets in protoplanetary disks.

Chapter 2

INVESTIGATING TRENDS IN ATMOSPHERIC COMPOSITIONS OF COOL GAS GIANT PLANETS USING *SPITZER* SECONDARY ECLIPSES

Wallack, N. L., Knutson, H. A., Morley, C. V., Moses, J. I., Thomas, N. H., Thorngren, D. P., Deming, D., Désert, J.-M., Fortney, J. J., & Kammer, J. A. (2019). Investigating Trends in Atmospheric Compositions of Cool Gas Giant Planets Using Spitzer Secondary Eclipses. *The Astronomical Journal*, *158*(6), 217. https://doi.org/10.3847/1538-3881/ab2a05.

2.1 Introduction

Observations of the ever-expanding ensemble of exoplanetary systems provide unique statistical insights into the formation and evolution of planetary systems. This is perhaps best illustrated by the classic correlation between gas giant planet frequency and host star metallicity (Fischer & Valenti, 2005), which suggests that these planets most likely formed via core accretion (e.g., Pollack et al., 1996; Johansen and Lambrechts, 2017). Observations of the masses and radii of extrasolar gas giant planets also indicate that, like the giant planets in our solar system, the average densities of these planets tend to increase with decreasing mass (Miller and Fortney, 2011; Thorngren et al., 2016). These trends are consistent with a picture in which Jovian-mass planets were able to accrete substantially more gas from the protoplanetary disk than Neptune-mass planets, either because their cores reached the critical mass for gas accretion earlier or because they formed in a region of the disk with a higher gas surface density (e.g., at shorter orbital periods).

The atmospheric compositions of gas giant planets should in theory allow us to distinguish between these two scenarios, as the incorporation of solids into the growing planet's atmosphere will enrich its bulk metallicity and leave a unique compositional fingerprint that will vary according to its formation location and epoch (e.g., Öberg et al., 2011; Espinoza et al., 2017). In the solar system, Jupiter has both a smaller core mass fraction and a lower atmospheric carbon-to-hydrogen ratio than Neptune (e.g., Lodders, 2003). However, with only one planetary system it is difficult to determine the relative importance of the formation location in determining atmospheric metallicity. If we instead consider the broader population of exo-

Jupiters and exo-Neptunes, which presumably originate from a variety of formation locations, we can ask whether exo-Neptunes consistently exhibit higher atmospheric metallicities than exo-Jupiters (and therefore whether such enhancement is largely independent of formation location) or whether both populations span a wide range of atmospheric metallicities that reflect their varied formation locations and accretion histories (Humphries & Nayakshin, 2018).

In principle, we can directly determine the mean molecular weights and corresponding metallicities of transiting planet atmospheres by measuring their wavelength-dependent transit depths or transmission spectra (e.g., Seager and Sasselov, 2000). However, a majority of the gas giant planets observed to date have clouds in their day-night terminator region that attenuate the amplitude of the expected absorption features (e.g., Sing et al., 2016; Barstow et al., 2017), leading to degeneracies between cloud-top pressure and atmospheric metallicity for observations with low signal-to-noise detections (e.g., Benneke and Seager, 2012). This problem is especially acute for exo-Neptunes, which typically have smaller planet-star radius ratios and higher surface gravities than their Jovian counterparts, both of which make it more challenging to detect atmospheric absorption during the transit. There are currently only three exo-Neptunes with published transmission spectra (GJ 436b, Knutson, Benneke, et al., 2014; HAT-P-11b, Fraine et al., 2014; and HAT-P-26b, Wakeford et al., 2017), and of these three, HAT-P-26b is the only one with a relatively clear atmosphere and correspondingly strong constraints on its atmospheric metallicity. Interestingly, this planet appears to have an atmospheric metallicity substantially lower than that of Neptune (Wakeford et al., 2017).

Although clouds are problematic for transmission spectroscopy, observations of the thermal emission spectra of these same cloudy planets indicate the presence of strong molecular absorption features (e.g., HD 189733b, Crouzet et al., 2014, Todorov et al., 2014; GJ 436b, Morley et al., 2017). This is due in part to the shorter path length for thermal emission as compared to transmission spectroscopy, which minimizes the scattering opacity (Fortney, 2005). We also expect that these tidally locked planets should exhibit day-night temperature gradients that might prevent clouds condensing in the cooler terminator region from extending into the hotter dayside region (e.g., Demory et al., 2013; Parmentier et al., 2016), although meridional advection of cloud particles may also affect the observed cloud properties (Lee et al., 2016; Lines et al., 2018). Secondary eclipse observations of the Neptune-mass planet GJ 436b ($<$800 K) indicate that it has strong molecular features in its emission spectrum that can only be matched by a substantially metal-enriched atmosphere (200 – 1000× solar; Stevenson et al., 2010, Moses, Line, et al., 2013, Lanotte et al., 2014, Morley et al., 2017).

In Kammer et al. (2015) we used broadband emission spectroscopy in the same 3.6 and 4.5 μm bands to constrain the atmospheric compositions of five transiting gas giant planets with temperatures cooler than 1200 K and masses ranging between 0.3 and 3 M_{Jup}. For these relatively cool hydrogen-rich atmospheres, models predict that the ratio of methane to carbon monoxide and carbon dioxide should act as a sensitive barometer of atmospheric metallicity and the carbon-to-oxygen ratio (Moses, Line, et al., 2013). Kammer et al. (2015) leveraged the fact that the 3.6 μm *Spitzer* band is sensitive to CH_4 absorption while the 4.5 μm band is sensitive to CO and CO_2 absorption. The ratio of the measured eclipse depths in these two bands can therefore be used to provide constraints on relative trends in atmospheric composition. Although these measurements hinted at a possible trend in atmospheric metallicity versus planet mass, our sensitivity was limited by the large measurement errors characteristic of these types of observations and our relatively small sample size.

In this study, we utilize the Infra-Red Array Camera (IRAC) on board the *Spitzer Space Telescope* to obtain a combined total of 28 3.6 μm and 4.5 μm secondary eclipse observations for a sample of five additional transiting gas giant planets with temperatures below ~1000 K and masses between 0.05 and 2.0 M_{Jup} (see Table 2.1 for more information). Our targets in this study include HAT-P-15b (Kovács et al., 2010), HAT-P-17b (Howard et al., 2012), HAT-P-18b (Hartman, Bakos, Sato, et al., 2011), HAT-P-26b (Hartman, Bakos, Kipping, et al., 2011), and WASP-69b (Anderson et al., 2014). Of these five planets, HAT-P-26b is the only one with published constraints on its atmospheric metallicity from transmission spectroscopy (Wakeford et al., 2017), with a range of 0.8 – 26× solar (1σ). Optical transmission spectroscopy of HAT-P-18b between 475 and 925 nm from the William Herschel Telescope indicates that it has a featureless spectrum consistent with Rayleigh scattering in this wavelength range (Kirk et al., 2017), but this result is still consistent with a wide range of atmospheric metallicities. Casasayas-Barris et al. (2017) detected sodium absorption at high spectral resolution in the transmission spectrum of WASP-69b, but did not place any constraints on its atmospheric metallicity.

	HAT-P-15b	HAT-P-17b	HAT-P-18b	HAT-P-26b	WASP-69b
T_* (K)	5568±90	5246±80	4803±80	5011±55	4715±50
Mass (M_{Jup})	$1.949^{+0.08}_{-0.078}$	0.537±0.017	0.200±0.019	0.059±0.007	0.250±0.023
Radius (R_{Jup})	1.072±0.043	1.010±0.029	0.995±0.052	$0.565^{+0.072}_{-0.032}$	1.057±0.047
T_{eq} (K)[a]	902±27	791±17	822±22	1028±21	961±20
e[b]	$0.200^{+0.026}_{-0.028}$	0.3417±0.0036	<0.087(<0.16)	$0.14^{+0.12}_{-0.08}$	<0.11(<0.23)
ω (deg)[b]	$262.5^{+2.4}_{-2.9}$	200.5±1.3	...	46^{+33}_{-71}	...
Period (days)[c]	10.863502(37)	10.3385230(90)	5.5080291(42)	4.2345023(15)	3.868138(17)
T_c(BJD-2,450,000)[c]	4638.56094(48)	4801.17018(20)	4715.02254(39)	5304.65218(25)	5748.83422(18)
References	1,2,3	3,4,5,6	3,7,8,9	6,10,11,12	3,13

Table 2.1: System Properties

[a]Calculated assuming planet-wide heat circulation and zero albedo. Uncertainties on the temperature calculated from the uncertainties on a/R_* and T_*. The semi-major axis and R_* values and their corresponding uncertainties for HAT-P-15b, HAT-P-17b, and WASP-69b are taken from reference 3 and for HAT-P-18b from reference 9. R_* and semi-major axis for HAT-P-26b are from Wakeford et al. (2017).
[b]The orbital eccentricity e and longitude of periapse ω are derived from fits to radial velocity data.
[c]Uncertainties on the last two digits are parenthesized.

References. (1) Kovács et al. (2010), (2) Torres et al. (2012), (3) Bonomo et al. (2017), (4) Howard et al. (2012), (5) Fulton et al. (2013), (6) Mortier et al. (2013), (7) Hartman, Bakos, Sato, et al. (2011), (8) Kirk et al. (2017), (9) Seeliger et al. (2015), (10) Hartman, Bakos, Kipping, et al. (2011), (11) Knutson, Fulton, et al. (2014), (12) Stevenson et al. (2016), (13) Anderson et al. (2014)

In Section 2.2, we describe our photometric extraction and model fits. In Sections 2.3 and 2.4, we compare our results to atmosphere models and discuss the corresponding implications for our understanding of trends in atmospheric composition.

2.2 Observations and Data Analysis

Photometry and Initial Model Fits

We obtained a minimum of two visits each in the IRAC 3.6 and 4.5 μm bands (Fazio et al., 2004) for all planets in our sample, with additional observations for lower signal-to-noise targets. A majority of these observations were observed in the 32×32 pixel subarray mode with an initial thirty-minute observation to allow for settling of the telescope followed by a peak-up pointing adjustment prior to the start of the science observation (Ingalls et al., 2012). The only exceptions are the 3.6 μm 2011 November observation of HAT-P-15b, the 3.6 μm 2012 January and 4.5 μm 2012 February observations of HAT-P-17b, and the 4.5 μm 2011 August observation of HAT-P-18b, which did not include this initial 30-minute observation and subsequent pointing adjustment. The 2011 observation of HAT-P-15b was also obtained in full-array mode instead of subarray mode. See Table 2.2 for additional details.

Target	λ (μm)	UT Start Date	Length (h)	t_{int}(s)[a]	t_{trim}(h)[b]	r_{pos}[c]	r_{phot}[d]	n_{bin}[e]	RMS[f]
HAT-P-15b	3.6	2011 Nov 27	7.8	6.0	1.5	2.5	2.1	4	1.40
	3.6	2012 May 8	7.9	2.0	0.5	2.5	2.2	16	1.13
	3.6	2014 Apr 25	11.35	2.0	1.0	4.0	2.0	8	1.15
	4.5	2012 Apr 27	7.9	2.0	0.0	4.0	2.6	2	1.14
	4.5	2012 Nov 19	7.9	2.0	2.0	2.5	2.3	2	1.09
	4.5	2014 May 27	11.35	2.0	1.5	4.0	2.2	8	1.10
HAT-P-17b	3.6	2012 Jan 25	7.9	2.0	0.0	4.0	2.0	2	1.14
	3.6	2012 Aug 29	7.9	2.0	2.0	3.0	2.5	64	1.10
	3.6	2014 Sep 02	8.6	2.0	2.0	3.5	2.4	4	1.21
	4.5	2012 Feb 04	7.9	2.0	0.5	4.0	2.7	32	1.12
	4.5	2012 Sep 08	7.9	2.0	2.0	3.0	2.4	128	1.10
	4.5	2012 Sep 22	8.6	2.0	2.0	3.5	2.4	4	1.22
HAT-P-18b	3.6	2012 May 19	7.9	2.0	1.5	4.0	2.0	2	1.13
	3.6	2014 May 22	5.8	2.0	2.0	3.0	2.0	4	1.12
	4.5	2011 Aug 28	11.9	2.0	1.5	4.0	2.5	64	1.15
	4.5	2014 Jun 2	5.8	2.0	0.5	4.0	2.0	4	1.09

Target	λ (μm)	UT Start Date	Length (h)	t_{int}(s)[a]	t_{trim}(h)[b]	r_{pos}[c]	r_{phot}[d]	n_{bin}[e]	RMS[f]
HAT-P-26b	3.6	2014 Apr 11	7.4	2.0	1.5	2.5	2.0	2	1.13
	3.6	2014 Apr 24	7.4	2.0	1.0	3.5	2.0	2	1.16
	3.6	2014 Sep 10	7.4	2.0	1.0	4.0	2.3	512	1.22
	3.6	2014 Sep 27	7.4	2.0	1.0	3.5	2.2	2	1.21
	4.5	2014 Apr 15	7.4	2.0	2.0	4.0	2.8	8	1.14
	4.5	2014 May 06	7.4	2.0	1.0	3.5	2.4	2	1.11
	4.5	2014 Sep 15	7.4	2.0	0.0	3.5	2.0	2	1.20
	4.5	2014 Oct 02	7.4	2.0	2.0	4.0	2.1	64	1.19
WASP-69b	3.6	2014 Jul 22	9.8	0.4	2.4	3.5	2.0	2	1.15
	3.6	2014 Jul 29	9.8	0.4	2.0	3.5	2.0	8	1.13
	4.5	2014 Aug 18	9.8	0.4	0.0	3.5	2.3	2	1.16
	4.5	2015 Jan 08	9.8	0.4	2.0	3.5	2.3	2	1.13

Table 2.2: *Spitzer* Observation Details

[a]Integration time
[b]Initial trim duration
[c]Radius of the aperture (in pixels) used to determine the location of the star on the array
[d]Radius of the aperture (in pixels) used for the photometry
[e]Bin size used for fits
[f]Ratio of measured RMS to the photon noise limit

We utilize the standard Basic Calibrated Data (BCD) images for our analysis and extract photometric fluxes as described in our previous studies (i.e., Knutson et al., 2008; Kammer et al., 2015; Morley et al., 2017). We first calculate the BJD_{UTC} mid-exposure times for each image. We then estimate the sky background in each image by masking out a circular region with a radius of 15 pixels centered on the position of the star, iteratively trimming 3σ outliers, and fitting a Gaussian function to a histogram of the remainder of the pixels. For the full-array observation of HAT-P-15b, we determine the sky background using the median flux in an annulus with radii between 15 and 37 pixels centered on the position of the star. We determine the location of the star on the array using flux-weighted centroiding (e.g., Knutson et al., 2008; Deming et al., 2015) with a circular aperture. We consider aperture radii ranging between 2.5 and 4.0 pixels in 0.5 pixel steps and optimize our choice of aperture as described below. We then extract the total flux in a circular aperture centered on the position of the star using the `aper` routine in the `DAOPhot` package (Stetson, 1987). We consider aperture sizes ranging from 2.0 to 3.0 pixels in steps of 0.1 pixels and from 3.0 to 5.0 pixels in steps of 0.5 pixels.

Some visits also display a ramp-like behavior at early times, which we mitigate by trimming up to two hours from the start of our time series. As discussed in Deming et al. (2015) and Kammer et al. (2015), we find that binning our data before fitting reduces the amount of time-correlated noise in the residuals. We determine the optimal flux-weighted centroiding aperture, photometric aperture, trim duration, and bin size for each visit by first fitting a combined instrumental and astrophysical model to each version of the photometry and then calculating the standard deviation of the residuals as a function of bin size stepping in powers of two as described in Kammer et al. (2015). We then calculate the least-squares difference between the measured standard deviation of the residuals and the predicted photon noise limit in each bin, which decreases as the square root of the number of points. We then select the photometric and centroiding apertures, trim duration, and bin size that minimizes this least-squares difference (i.e., the one that is closest to the photon noise at all measured timescales) for use in our subsequent analysis. Because we typically do not detect the eclipse in each individual visit, we fix the time of secondary eclipse to the predicted value (phase=0.5 for HAT-P-18b, HAT-P-26b, and WASP-69b, and using the best-fit radial velocity (RV) solution for HAT-P-15b and HAT-P-17b) during our initial optimization (see Section 2.2 for additional details). Our observations of WASP-69b also showed a steep downward trend after the end of the eclipse, which was not well matched with our standard linear function of time. In order to avoid fitting a quadratic function of time, which has the potential to bias our measured eclipse depth, we also trimmed up to 2 hours from the end of the time series for all of the WASP-69b observations. We optimized this trim duration in the same manner as for the initial trim duration.

Our model for each visit consists of an eclipse model and an instrumental noise model, which we fit simultaneously. We calculate our eclipse model using the `batman` package (Mandel and Agol, 2002; Kreidberg, 2015), where we fix the planet-star radius ratio, orbital inclination, and the ratio of the orbital semi-major axis to the stellar radius (a/R_*) to the published values for each planet (see Table 2.1 for references) and allow the eclipse depth and time to vary as free parameters.

The flux we measure also depends on the position of the star on the array in each image. This is due to *Spitzer*'s well-documented intrapixel sensitivity variations (e.g., Charbonneau et al., 2005; Reach et al., 2005; Morales-Calderon et al., 2006) combined with an undersampled stellar point spread function (the FWHM in the 3.6 and 4.5 μm arrays is approximately two pixels for data taken during the post-cryogenic mission). We correct for this effect using the pixel-level decorrelation (PLD) method (Deming et al., 2015). This method uses a linear combination of individual pixel-level light curves as the instrumental noise model, and is therefore able to capture trends due to variations in both the star's position and the width of the stellar point spread function. As in Deming et al. (2015), we utilize a 3 x 3 grid of pixels centered on the location of the star in our model. We remove astrophysical flux variations in each 3 x 3 postage stamp by dividing by the summed flux across all nine pixels. Our final instrumental noise model therefore consists of nine linear coefficients corresponding to the nine individual pixel-level light curves, as well as a linear function of time to capture any long-term trends (i.e., 11 free parameters in total). For all fits we divide out our initial astrophysical model and use linear regression on the residuals to obtain an initial guess for the nine linear PLD coefficients in order to speed up convergence for these highly correlated parameters.

Simultaneous Fits and Choice of Prior on Eclipse Phase

Because a majority of the planets in our study have relatively shallow eclipse depths, we do not expect to detect the eclipse signal in fits to individual visits. We therefore carry out our initial fits to individual visits using a fixed eclipse time. For HAT-P-18b, HAT-P-26b, and WASP-69b the published RVs are consistent with a circular orbit (Knutson, Fulton, et al., 2014; Bonomo et al., 2017) and we therefore fix the eclipse

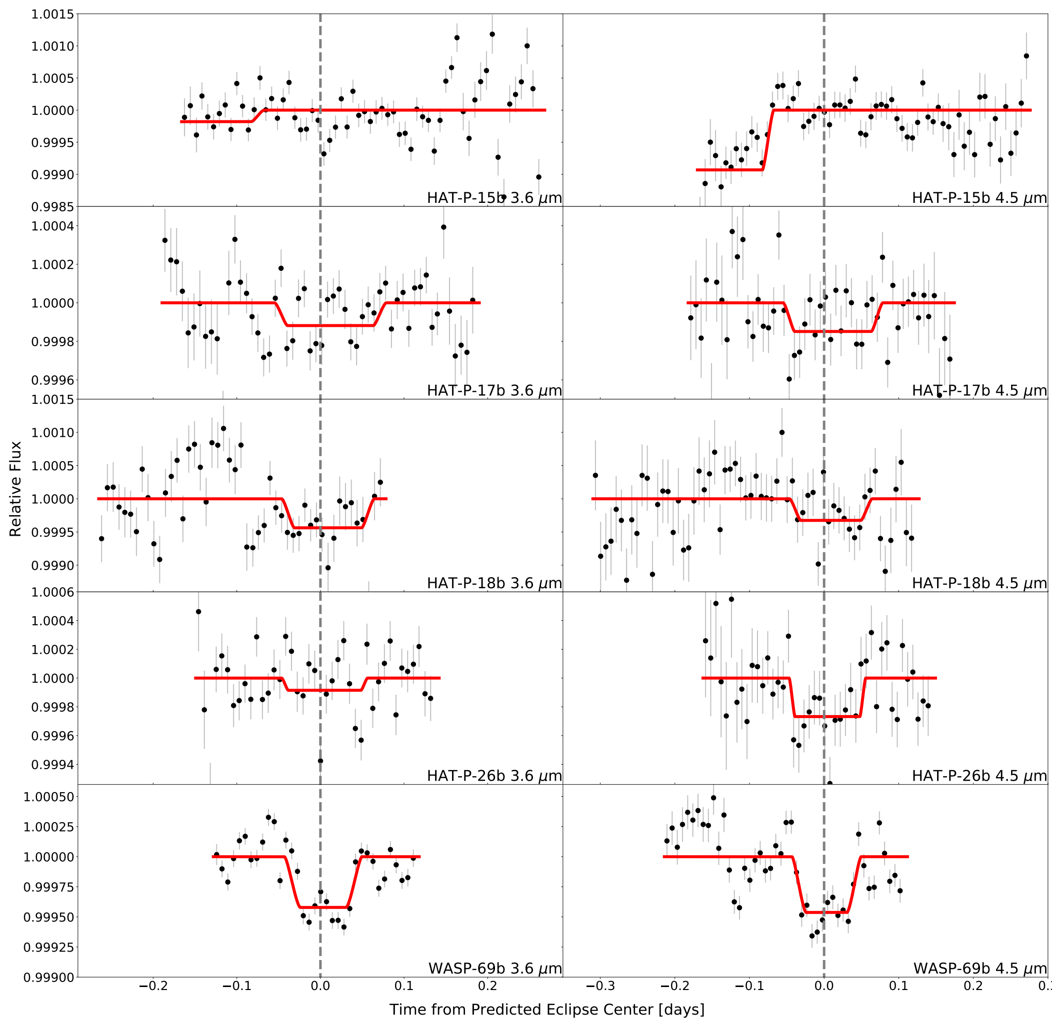

Figure 2.1: Phased light curves for each planet from the simultaneous fits with instrumental effects removed. We show data binned in ten-minute intervals (black filled circles) with error bars corresponding to the scatter in each bin, and overplot the best-fit eclipse model in each bandpass for comparison (red lines). The 2σ upper limits for the best-fit eclipse depths of the 3.6 μm and 4.5 μm bandpasses for HAT-P-15b (see Section 2.2 for more details), the 4.5 μm bandpass for HAT-P-17b, and the 3.6 μm bandpass for HAT-P-26b are shown.

phase to 0.5. HAT-P-15b and HAT-P-17b have non-zero orbital eccentricities and we therefore fix the eclipse time to the predicted value from the literature (Bonomo et al., 2017). After optimizing our choice of aperture, bin size, and trim duration for each individual visit, we next carry out a joint fit to all of the visits for a given planet. In these fits we assume a common eclipse depth for each bandpass and a common eclipse phase for all visits regardless of bandpass, and allow these three parameters to vary in our fits. In this case, we place a uniform prior on the eclipse time spanning the range of times where the full eclipse would be visible in the data (i.e., we disallow eclipse times that are either partially or fully outside our observational window). We then fix the eclipse time to the best-fit value from the simultaneous fit and revisit our choice of optimal aperture, bin size, and trim duration for each individual visit. Lastly, we rerun the simultaneous fit using these newly optimized light curves.

We estimate the uncertainties on the best-fit eclipse parameters in these simultaneous fits using the affine-invariant Markov chain Monte Carlo (MCMC) ensemble sampler `emcee` (Foreman-Mackey et al., 2013). Our combined astrophysical and instrumental noise model has 14 free parameters, and we therefore use 60 walkers in our fits in order to ensure sufficient sampling of the model parameter space. We place uniform priors on all of our model parameters except where noted below. We also allow the eclipse depths to take on negative values in our fits (i.e., an increase in flux during the eclipse) in order to avoid biasing our estimate of the eclipse depth by requiring only positive values. We initialize the walkers in a tight cluster centered on the best-fit solution from a Levenberg-Marquardt minimization and carry out an initial burn-in with a length of 10,000 steps. We then discard this initial burn-in and carry out a subsequent fit with 10^5 steps per chain. We report the median values from our MCMC chains and the corresponding 1σ uncertainties.

We show the raw photometry for each visit with best-fit instrumental noise models from the simultaneous fit overplotted in Figures 2.13— 2.15 in the appendix. Normalized light curves for these visits with best-fit eclipse light curves overplotted are shown in Figures 2.16— 2.18. The standard deviation of the residuals as a function of bin size for each visit is shown in Figures 2.19— 2.21, with the predicted photon noise limit for each bin size overplotted for comparison. We also combine all visits within the same bandpass and show these averaged light curves in Figure 2.1.

We modified our approach for HAT-P-26b, which is the only planet in our sample with four visits in each bandpass. In this case a simultaneous fit to all eight visits would require a prohibitively large model with a total of 91 free parameters. We instead elect to fit each bandpass separately, and find that the eclipse is detected at 4.5 μm but not at 3.6 μm. We therefore repeat our fits to the 3.6 μm data with a Gaussian prior on the eclipse time centered on the best-fit eclipse phase from the 4.5 μm fits and with a width equal to the $\pm 1\sigma$ uncertainty on this parameter.

HAT-P-15b was the only planet in our sample with no eclipse detection in either band. Previous RV observations of this planet indicate that it has an orbital eccentricity of 0.190 ± 0.019 (Kovács et al., 2010), and we therefore centered our window on the predicted secondary eclipse phase rather than a phase of 0.5. Bonomo et al. (2017) subsequently reported an updated eccentricity constraint of $0.200^{+0.026}_{-0.028}$ with a corresponding uncertainty in the predicted eclipse phase of ±0.058 days. This means that our shortest observational window for this planet (7.8 hours) encompassing the entirety of the eclipse only spanned -1.5σ to +1.3σ, while the longest observation (11 hours) spanned -2.0σ to +3.4σ. Because we do not expect to detect the eclipse at a statistically significant level in a single visit, the shortest observation window becomes the limiting factor on the effective phase range of our search.

Within this range, we place an upper limit on the eclipse depth in each bandpass by carrying out fits with a Gaussian prior on the eclipse phase based on the RV fit from Bonomo et al. (2017). This results in a multimodal posterior for the best-fit eclipse center time, with one peak corresponding to a fit in which the center of the secondary eclipse occurred at the very beginning of the observations (i.e., the entirety of the eclipse is not within the data) and the other peak centered at the expected time of secondary eclipse (see Figure 2.2). The fitted 3.6 μm secondary eclipse depth was consistent with zero in both peaks, but the 4.5 μm secondary eclipse depth was bimodal. In order to be more conservative, we report the 2σ upper limits on the eclipse depth corresponding to the peak that is centered at the earlier time of secondary eclipse (i.e. the time that gives a positive upper limit on the 4.5 μm eclipse depth).

We also test how the use of a Gaussian prior on the time of secondary eclipse as determined by RV measurements effects the measured eclipse depths for HAT-P-17b. We find that using either a flat prior (the time of secondary eclipse must be centered between -0.1 days and 0.1 days where zero is the time of secondary eclipse predicted using the Bonomo et al. (2017) eccentricity constraints) or a Gaussian prior (with the mean of the distribution occurring at the time of the secondary eclipse corresponding to zero days and a standard deviation of 1σ as determined from the Bonomo et al., 2017 eccentricity constraints) results in the same measured eclipse depths to within 1σ. Therefore, we report the best-fit values using the less restrictive prior.

Our observations of HAT-P-18b also proved to be particularly challenging. While Hartman, Bakos, Sato, et al. (2011) reported a non-zero eccentricity for HAT-P-18b with $\sim 2\sigma$ significance, we subsequently acquired additional RV measurements and refit these data in Knutson, Fulton, et al. (2014), where we found that the orbit was consistent with zero eccentricity (e= $0.11^{+0.15}_{-0.08}$). As a result, we centered the 2011

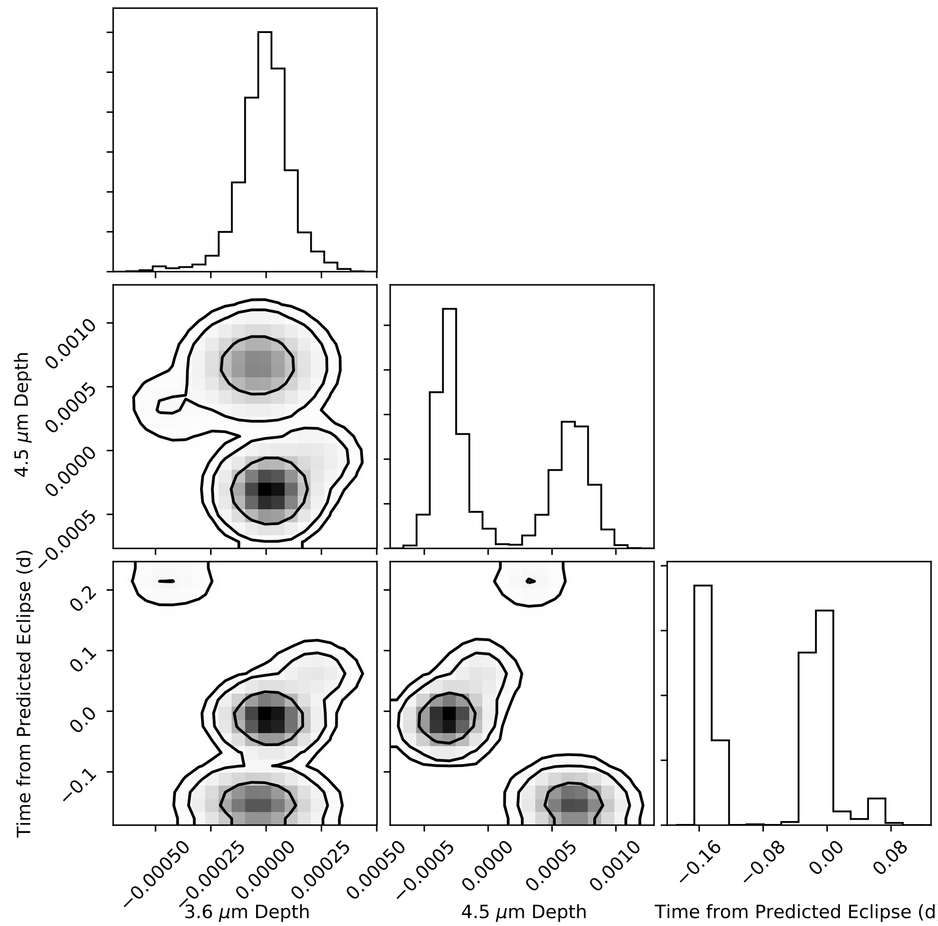

Figure 2.2: Posterior probability distribution for the secondary eclipse center time and depth in both bands from a joint fit with a Gaussian prior derived from the RV constraints on the eclipse center time for HAT-P-15b. Contours indicate the 1σ, 2σ, and 3σ bounds on these parameters.

4.5 μm and 2012 3.6 μm observations on the predicted eclipse time for the eccentric orbit from Hartman, Bakos, Sato, et al. (2011), and then centered the subsequent 2014 3.6 and 4.5 μm observations on an orbital phase of 0.5 (i.e., a circular orbit). Although the 2011 4.5 μm observation is not centered on a phase of 0.5, it does contain the entirety of the eclipse detected in our simultaneous fits (see Figure 2.17). However, the 2012 3.6 μm observation only spans the first half of the eclipse.

When we tried to fit the two channels of HAT-P-18b separately as we did for HAT-P-26b, we found marginal 2.7 and 1.2σ detections in the 3.6 μm and 4.5 μm bandpasses, respectively, when tight flat priors were used. However, switching to a joint fit of both bands with a flat prior allowing for the secondary eclipse to occur

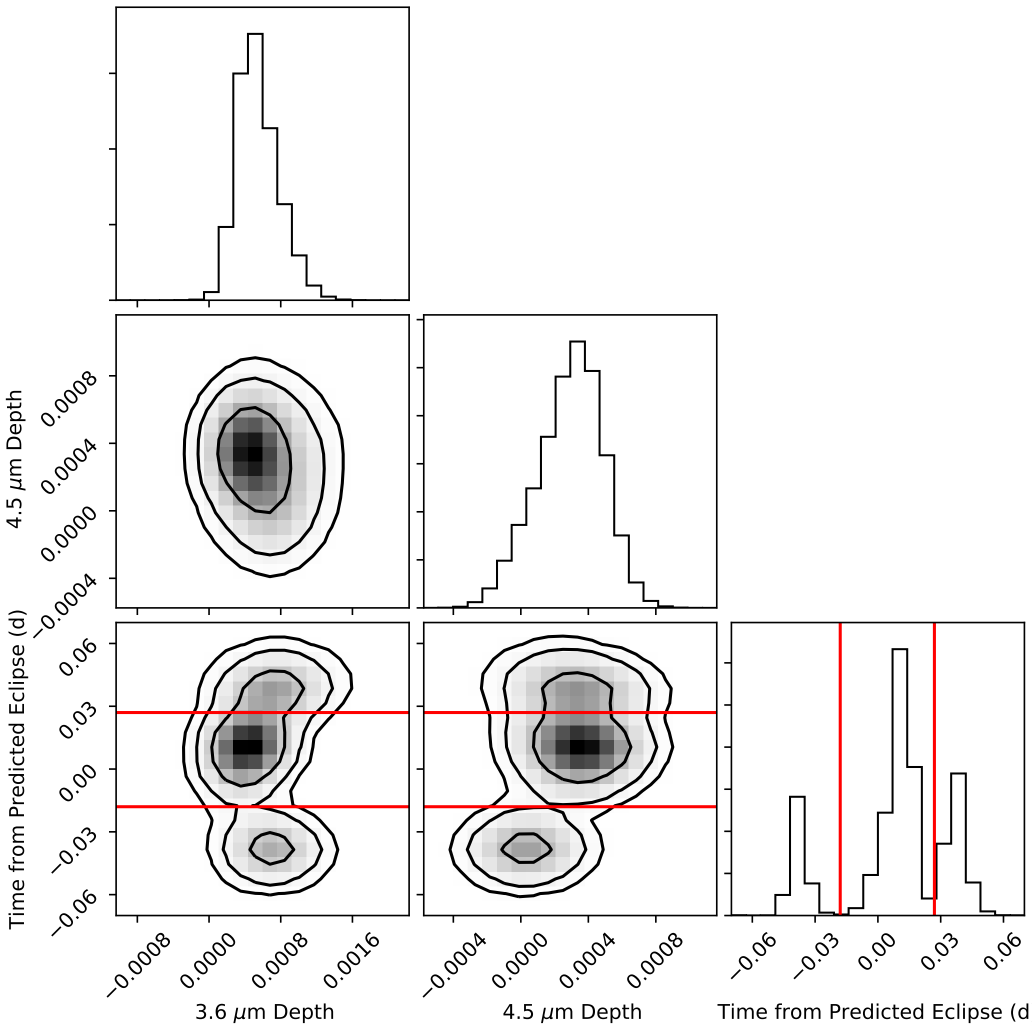

Figure 2.3: Posterior probability distribution for the secondary eclipse center time and depth in both bands from a joint fit with a relatively broad uniform prior of -0.07 to 0.07 days on the eclipse center time for HAT-P-18b. Contours indicate the 1σ, 2σ, and 3σ bounds on these parameters, while the red lines show the prior constraints used in our final version of the fits for this planet.

any time during the full range of orbital phases spanned by our observations resulted in a multimodal posterior on the best-fit eclipse center time (see Figure 2.3) with marginal eclipse depths for both channels ($<1\sigma$).

The highest peak in this distribution is centered near zero, corresponding to an eclipse center time consistent with an orbital phase of 0.5. If we instead repeat our fits using a tighter uniform prior of -0.018 days to 0.027 days, therefore excluding the other two weaker peaks, it increases the significance of the detection in both bands to 3.0 and 2.2σ, respectively. We adopt this version of the fits as our final solution, as there is currently no evidence for a non-zero orbital eccentricity in the RV data for this planet and this peak had the highest posterior probability in our original fit.

2.3 Results

We report the best-fit eclipse depths and times and their corresponding uncertainties in Table 2.3. We detect the eclipse in both channels with high significance for WASP-69b and with somewhat lower significance for HAT-P-18b. We detect the eclipse at 4.5 μm but not at 3.6 μm for HAT-P-26b, detect the eclipse at 3.6 μm but not at 4.5 μm for HAT-P-17b, and do not detect the eclipse in either channel for HAT-P-15b.

Target	Band (μm)	Depth (ppm)	Brightness Temperature (K)	Time Offset (days)[a]	Center of Eclipse (Phase)	$e\cos(\omega)$[b]
HAT-P-15b	3.6	< 180[c]	< 971	0 ±0.0585[f]	0.4829±0.0054	$-0.0262^{+0.0082}_{-0.0084}$[g]
	4.5	<931[c,d]	<1355			
HAT-P-17b	3.6	118 ± 39	813^{+49}_{-61}	$0.0120^{+0.0120}_{-0.0130}$	0.2997±0.0012	-0.3146±0.0018
	4.5	< 149[c]	< 708			
HAT-P-18b	3.6	437^{+146}_{-144}[e]	1004^{+78}_{-94}	$0.0091^{+0.0054}_{-0.0073}$	$0.5016^{+0.0010}_{-0.0013}$	$0.0026^{+0.0015}_{-0.0021}$
	4.5	326^{+144}_{-147}[e]	783^{+77}_{-100}			
HAT-P-26b	3.6	< 85[c]	<949	0.0050±0.0037	0.5012 ± 0.0009	0.0019±0.0014
	4.5	265^{+68}_{-72}	1087^{+91}_{-102}	$0.0045^{+0.0031}_{-0.0038}$	$0.5011^{+0.0007}_{-0.0009}$	0.0017±0.0011
WASP-69b	3.6	421±29	1011±17	0.0033 ± 0.001	0.5009±0.0003	0.001± 0.0004
	4.5	463±39	863^{+19}_{-20}			

Table 2.3: Best-fit Eclipse Parameters

[a]Time offset from the predicted center of the eclipse. Unless otherwise noted, we fit both channels with a common time of secondary eclipse.
[b]Computed using the approximation for a low eccentricity orbit. Therefore, this only serves as a first-order approximation for the more highly eccentric orbit of HAT-P-17b. See Pál et al. (2010) for a detailed discussion of the correct treatment for higher eccentricity orbits.
[c]We report the 2σ upper limit for the eclipse depth.
[d]The solution for the eclipse depth at 4.5μm was multimodal, so we report the 2σ upper limit corresponding to the deepest of the eclipse solutions to be conservative. See Section 2.2 for more details.
[e]We report the secondary eclipse depths using a tight uniform prior (see Section 2.2 for more details).
[f]Due to the nondetections in both bandpasses, we simply report the time offset and corresponding phase of the Gaussian prior derived from the RV constraints from Bonomo et al. (2017; see Section 2.2 for more details).
[g]We report the ecos(ω) from Bonomo et al. (2017).

In order to interpret our results, we first convert the measured eclipse depth in each bandpass to a brightness temperature (e.g. Schwartz and Cowan, 2015). We then check for differences in brightness temperature between bands, which are indicative of changes in the shape of the planet's emission spectrum due to molecular features (see Section 2.4). We find that WASP-69b has molecular features (i.e., nonblackbody emission spectra) detected with a significance greater than 3σ, while HAT-P-17b, HAT-P-18b, and HAT-P-26b differ from the blackbody model by less than 3σ.

These same brightness temperatures can also be used to estimate the efficiency of heat recirculation between the planet's day- and nightsides. We find that the band-averaged brightness temperatures for all four planets with detected eclipses are consistent with their respective equilibrium temperatures (calculated assuming efficient day-night circulation and zero albedos), suggesting that they have either efficient day-night circulation, non-zero albedos, or a combination of the two (Kammer et al., 2015; Schwartz and Cowan, 2015, 2017).

We next use our best-fit eclipse phases to place tighter constraints on the values of $e\cos(\omega)$ for each planet. HAT-P-18b, HAT-P-26b, and WASP-69b all have time offsets that are consistent with a circular orbit (within $\sim 3\sigma$ of the time predicted from a circular orbit). HAT-P-17b was previously known to be eccentric, and our new observations confirm and refine the published eccentricity and longitude of periastron from Bonomo et al. (2017).

2.4 Discussion

Comparison to 1D Atmosphere Models

We compare our best-fit eclipse depths to predictions from 1D atmosphere models. Briefly, these models calculate the temperature structure of the atmosphere assuming both chemical and radiative-convective equilibrium. These models are described in more detail in Fortney (2005), Fortney et al. (2008), and Morley et al. (2013, 2017). Cross sections for molecular and atomic species are described in detail in Freedman et al. (2008, 2014), with updates to several species that are described in Marley et al.(2019, in preparation). Moderate resolution spectra are calculated using the thermal emission code described in the appendix of Morley et al. (2015). Stellar spectra are calculated using PHOENIX model atmospheres for the stellar properties given in Table 2.1. Surface gravities are calculated using the planet masses and radii in Table 2.1. To calculate the incident flux on the planet, we assume that the planet-star distance is the semimajor axis for both circular and eccentric planetary orbits.

We assume that heat is either efficiently redistributed or inefficiently redistributed to the nightside. We calculate model spectra for a range of metallicities from solar to 100× solar metallicity and a range of C/O ratios from C/O=0.15 to 1.5.

We also develop 1D thermo/photochemical kinetics and transport models for these planets to investigate the possible effects of disequilibrium chemistry (i.e., transport-induced quenching and photochemistry) on the atmospheric composition. These models use the Caltech/JPL KINETICS code (Allen et al., 1981) to solve the continuity equations for 92 neutral H-, C-, O-, and N-bearing species that interact via ~1600 forward-reverse chemical reaction pairs. The reaction list is derived from Moses, Line, et al. (2013), and further details of the exoplanet disequilibrium-chemistry modeling can be found in Moses et al. (2011), Moses, Line, et al. (2013), and Moses et al. (2016). Vertical transport in the models occurs through molecular and eddy diffusion, with the vertical profile of the eddy diffusion coefficient (K_{zz}) assumed to be similar to that derived for HD 189733b from general circulation models (Agúndez et al., 2014). Specifically, K_{zz} = $1{\times}10^7/(P(\mathrm{bar}))^{0.65}$ cm^2 s^{-1} in the radiative region in the upper troposphere and middle atmosphere (restricted to never exceeding 10^{10} cm^2 s^{-1} in the upper atmosphere), and a constant-with-altitude value of 10^{10} cm^2 s^{-1} in the convective region at pressures P greater than 100 bar.

The vertical grid in the disequilibrium model consists of 198 levels separated uniformly in log pressure. The thermal structure is taken from the radiative-convective equilibrium models described above. Zero flux boundary conditions are assumed at the top and bottom boundaries, and chemical-equilibrium abundances are assumed for the initial conditions. The protosolar abundances from Table 10 of Lodders et al. (2009) are assumed to be representative of solar composition, but the models assume that 20.7% of the oxygen is removed at depth as a result of the formation of silicates and other refractory condensates (see Visscher et al., 2010). The solar spectrum at solar minimum is adopted for the stellar ultraviolet spectrum for planets with G- and K-type host stars and the composite M-type stellar spectrum described in Moses, Line, et al. (2013) is adopted for planets with M-type host stars. All fluxes are scaled to the appropriate planet-star distance.

Chemistry of Cool Hydrogen-rich Atmospheres

We first use these models to examine the effect that varying atmospheric metallicity and the carbon-to-oxygen ratio has on the measured 3.6 and 4.5 μm broadband fluxes from these planets, in order to determine the degree of degeneracy between

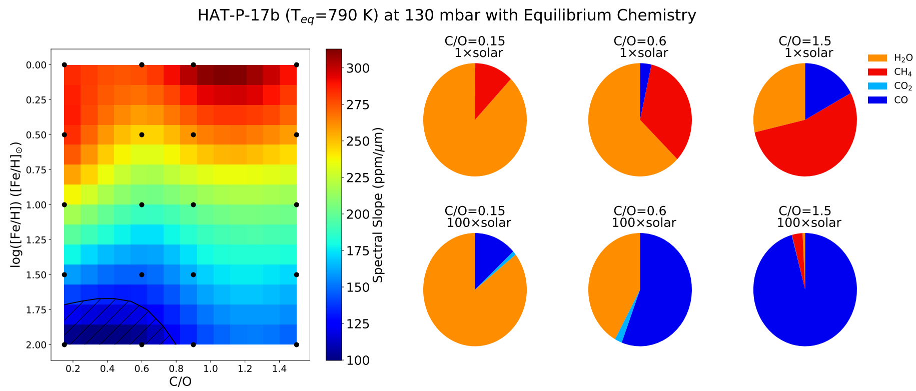

Figure 2.4: Heat map (left) showing the spectral slope expected for equilibrium chemical models with varying C/O ratios and metallicities for HAT-P-17b. Each black point represents a forward model, where we interpolate between models to generate the heat map. We indicate the region of parameter space consistent with this planet's measured spectral slope at the 2σ level or better with black diagonal lines. The pie charts (right) show the abundances of H_2O, CH_4, CO_2, and CO at a pressure representative of those probed in our observations for select models.

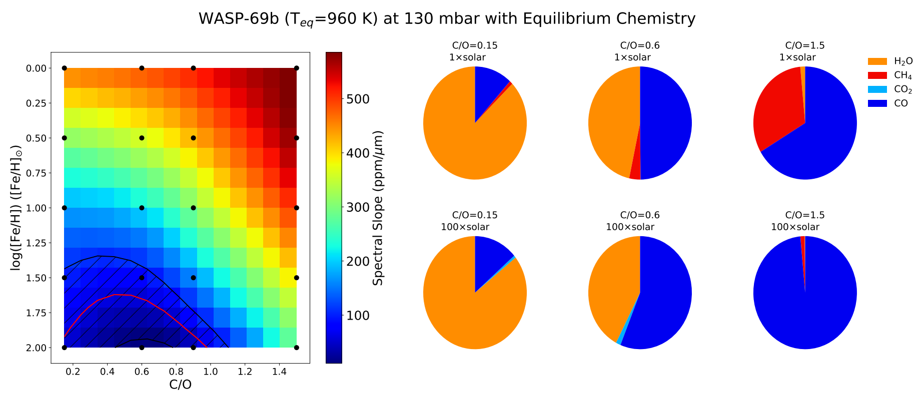

Figure 2.5: Heat map (left) showing the spectral slope expected for equilibrium chemical models with varying C/O ratios and metallicities for WASP-69b. Each black point represents a forward model, where we interpolate between models to generate the heat map. We show the best-fit value of this planet's measured spectral slope in red and show the region of parameter space consistent at the 1σ level or better with black diagonal lines. The pie charts (right) show the abundances of H_2O, CH_4, CO_2, and CO at a pressure representative of those probed in our observations for select models.

these two parameters. This topic has been previously explored with an extensive grid of generic equilibrium chemistry models in Molaverdikhani et al. (2018), and also with both forward modeling and atmospheric retrievals for the specific case of

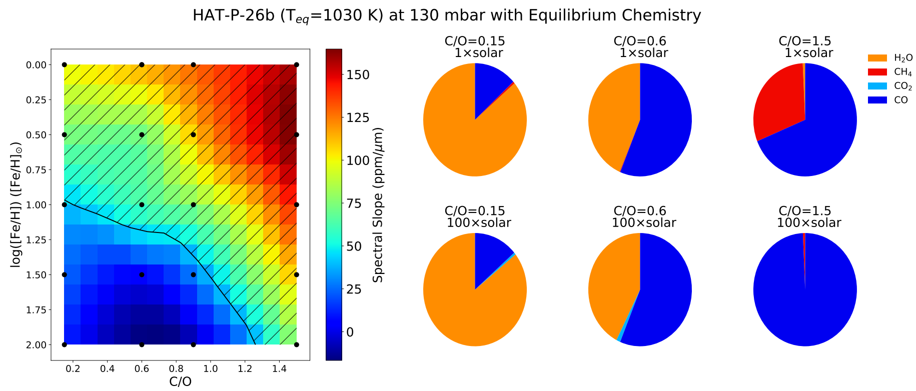

Figure 2.6: Heat map (left) showing the spectral slope expected for equilibrium chemical models with varying C/O ratios and metallicities for HAT-P-26b. Each black point represents a forward model, where we interpolate between models to generate the heat map. We indicate the region of parameter space consistent with this planet's measured spectral slope at the 2σ level or better with black diagonal lines. The pie charts (right) indicate the relative abundances of H_2O, CH_4, CO_2, and CO at a pressure representative of those probed in our observations for select models.

GJ 436b (Morley et al., 2017; Moses, Line, et al., 2013). These studies indicate that GJ 436b's very low ratio of CH_4 to CO and CO_2 can only be reproduced by relatively high (>200× solar) metallicity atmospheres even when the C/O ratio is allowed to vary as a free parameter. In this study we focus on results using forward models, as our two broadband data points are not sufficient for a full retrieval.

We run a grid of equilibrium models with C/O ratios of [0.15, 0.6, 0.9, 1.5] and metallicities of [1, 3, 10, 30, 100] for the hottest (HAT-P-26b; T_{eq} = 1030 ± 20 K), the coolest (HAT-P-17b; T_{eq} = 790 ± 20 K, comparable to GJ 436b), and intermediate temperature (WASP-69b; T_{eq} = 960 ± 20 K) planets in our sample and determine the expected 3.6 to 4.5 μm spectral slopes from each of these models. As shown in Figures 2.4—2.6, these models indicate that the smallest 3.6 to 4.5 μm spectral slopes (corresponding to planets that are relatively bright at 3.6 μm and dim at 4.5 μm) can only be achieved by models with both relatively high (> 50× solar) metallicities and C/O ratios less than ~ 1.5. This is because at solar C/O, the mixing ratios of H_2O, CH_4, CO, and CO_2 all increase as the atmospheric metallicity increases from 1× to 100× solar, leading to greater atmospheric opacity, higher temperatures, and a higher overall emission flux in the continuum regions. However, the CO and CO_2 mixing ratios increase much more rapidly with increasing metallicity than the CH_4 mixing ratio, leading to a significantly lower CH_4/(CO +

CO_2) ratio and greater absorption in the 4.5 μm band (where CO and CO_2 absorb) than in the 3.6 μm band (where CH_4 absorbs).

This overall picture remains true for all but the most extreme C/O ratios. Decreasing the atmospheric C/O ratio at 1× solar metallicity from 0.9 to 0.15 on a relatively warm planet like HAT-P-26b has only a small effect on the dominant oxygen and carbon species H_2O and CO, but has a much greater effect on minor constituents CH_4 and CO_2, with CH_4 being present at high C/O ratios and CO_2 at low C/O ratios. The higher C/O ratio model therefore exhibits more absorption in the 3.6 micron bandpass due to the increased presence of CH_4, but the relative insignificance of both CH_4 and CO_2 under these conditions means that varying the C/O ratio over this range has much less of an effect on the spectral slope than changing the atmospheric metallicity.

For cooler planets where CH_4 is expected to be the dominant carbon-bearing constituent at solar C/O ratios, extreme changes in C/O ratio can lead to significant changes in atmospheric chemistry. As the C/O ratio is reduced, these cooler planets will eventually experience a transition where the carbon shifts from CH_4 to CO_2 dominated carbon chemistries, with a corresponding major shift in spectral slope. Warmer CO-dominated planets can also transition to a different chemical regime when the C/O ratio becomes large enough that CH_4 becomes a major reservoir of carbon (see Figure 2.7 and Figure 2.8). The degree of the degeneracy between the atmospheric metallicity and the C/O ratio will be, at least in part, governed by the equilibrium temperature of the planet. In planets that are cool enough to have methane, metallicity will be the primary driver for the spectral slope (as shown by the fact that the C/O ratio does not greatly impact the spectral slope of HAT-P-17b in Figure 2.4). For warmer planets without significant methane, the spectral slope will be more strongly influenced by variations in the C/O ratio as shown in Figure 2.6 and to a lesser degree Figure 2.5.

As shown in Figures 2.7 and 2.8, as well as Figures 2.22— 2.25, the inclusion of disequilibrium chemical processes does not appreciably change this picture (e.g., Moses, Line, et al., 2013). The disequilibrium models have slightly less CH_4 and more CO and CO_2 in their upper atmospheres as compared to the equilibrium models, but this is a relatively minor shift compared to the change in chemistry as we vary the atmospheric metallicity and C/O ratio. We therefore conclude that under the thermal conditions relevant to the planets in our sample, variations in atmospheric metallicity are the dominant factor shaping the 3.6-4.5 μm spectral slopes, unless the atmosphere is highly enriched (C/O$> 1 - 1.5$) or depleted (C/O< 0.1) in carbon compared to oxygen. Although a more careful consideration of the 3D coupled chemistry and dynamics may alter this picture (e.g., Cooper and Showman, 2005; Bordwell et al., 2018; Drummond et al., 2018; Mendonça et al., 2018; Steinrueck et al., 2019), these effects are expected to be relatively minor, as the composition in the infrared photosphere tends to be homogenized to those of the warmest dayside regions.

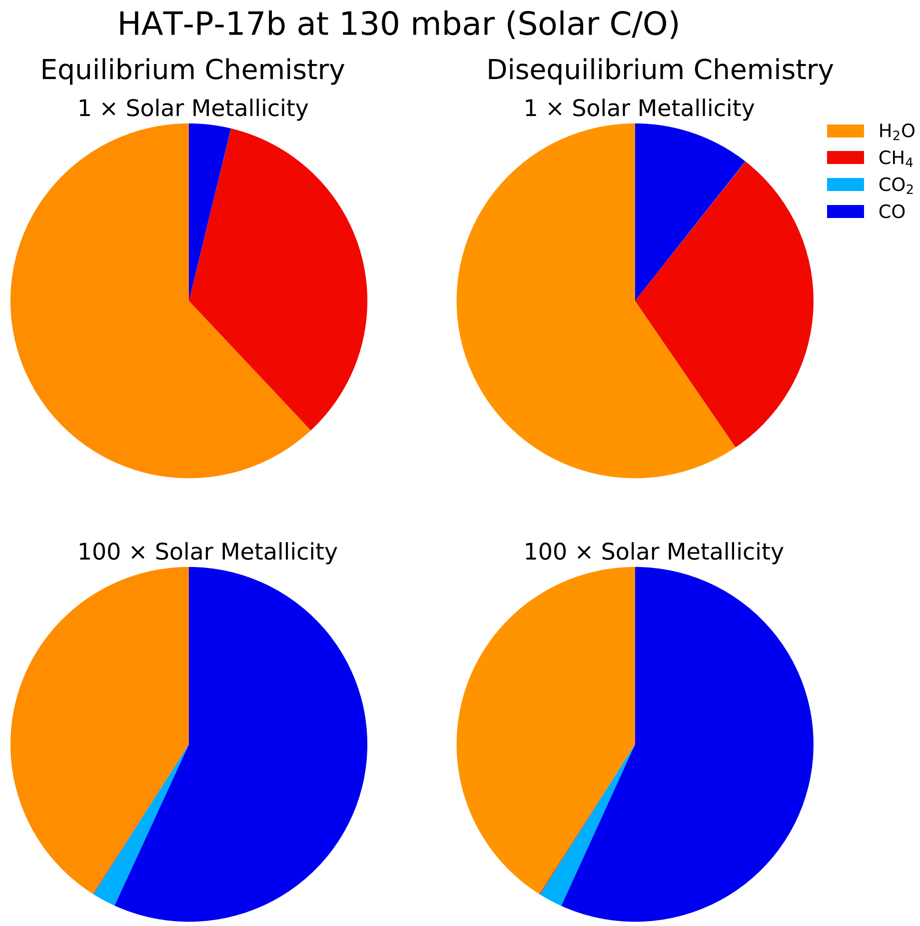

Figure 2.7: Comparison of chemical abundances of H_2O, CH_4, CO_2, and CO from the equilibrium chemical models (left) and disequilibrium chemical models (right) for 1× solar metallicity models (top) and 100× solar metallicity models (bottom) all with solar C/O ratios (C/O=0.6) at 130 mbar for our coolest planet, HAT-P-17b.

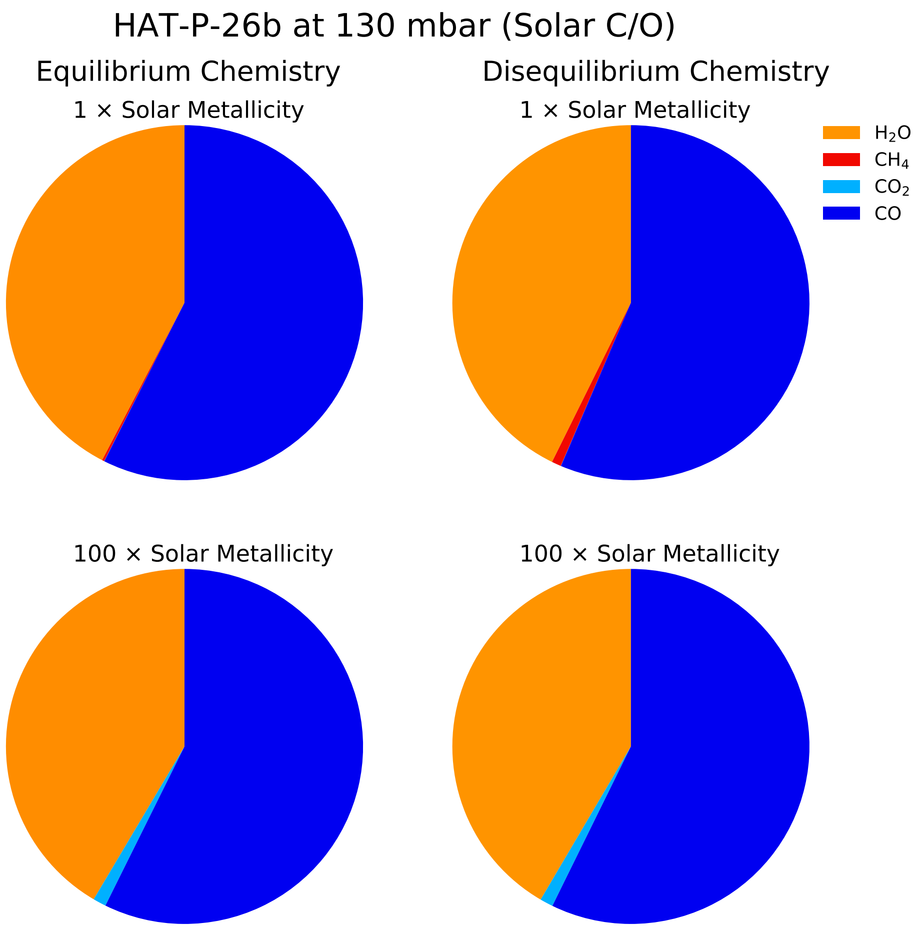

Figure 2.8: Comparison of the relative abundances of H_2O, CH_4, CO_2, and CO from the equilibrium chemical models (left) and disequilibrium chemical models (right) for 1× solar metallicity models (top) and 100× solar metallicity models (bottom) all with solar C/O ratios (C/O=0.6) at 130 mbar for our hottest planet, HAT-P-26b.

Model Comparison for Individual Planets

We next compare our measured secondary eclipse depths for each individual planet to a grid of four models, including atmospheric metallicities of either 1× or 100× solar and either full recirculation (i.e., complete redistribution of heat to the planet's nightside) or dayside-only recirculation (i.e., redistribution of heat limited to the dayside hemisphere alone). This set of four models represents a reasonably compact sampling of the possible parameter space, with redistribution efficiency allowing us to make each model globally hotter or cooler while varying atmospheric metallicity serves as a simplified proxy for changes in atmospheric chemistry that can affect the spectral slope. The resulting models are shown in Figure 2.9. Although we include the 3.6 μm depth for HAT-P-15b for completeness, we do not detect an eclipse in either bandpass, and therefore refrain from any further discussion of the implications of the eclipse depths for our understanding of this planet's atmosphere.

As in Kammer et al. (2015), model-data comparisons for all four planets with detected eclipses strongly prefer models with efficient circulation between the day- and nightside hemispheres. We find that the HAT-P-26b eclipses are best matched by the 1$\times$ solar metallicity model, in good agreement with the constraints from transmission spectroscopy presented in Wakeford et al. (2017). The WASP-69b eclipses are well matched by the 100$\times$ solar metallicity model. Our constraints for HAT-P-17b and HAT-P-18b are somewhat weaker, but still appear to modestly favor the 100$\times$ solar metallicity model over the 1$\times$ solar model.

Model-independent Trends in Atmospheric Composition

We next consider the same model-independent metric used in Kammer et al. (2015) to search for trends in atmospheric composition. This metric is defined as the ratio of the measured brightness temperatures in the 4.5-3.6 μm bandpasses, and should be effectively independent of the planet-star radius ratio and equilibrium planet temperature. We expect variations in this ratio to instead reflect the relative strength of CH_4 (3.6 μm) versus CO and CO_2 (4.5 μm) absorption features in the atmospheres of these planets. We use this ratio to search for empirical correlations with other parameters of interest including the planet's mass, bulk metallicity, and host star metallicity.

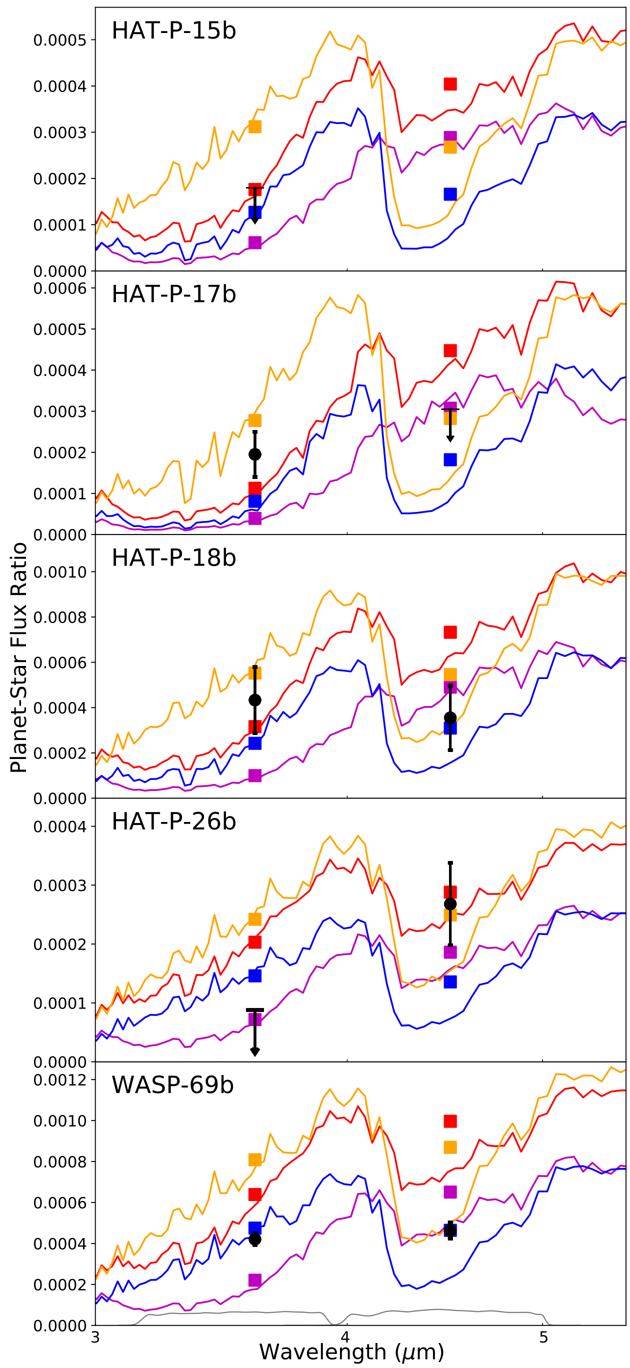

Figure 2.9: Planet-star flux ratios as a function of wavelength from 1D atmosphere models for all five planets. We show 1× solar and 100× solar metallicity models with either efficient (purple and blue, respectively) or inefficient (red and orange, respectively) redistribution of energy to the planet's nightside. Our measured eclipse depths for each planet are shown as black circles, and we plot the corresponding band-integrated flux values from the models as filled squares. For HAT-P-15b (3.6 μm only; see Section 2.2 for more details), HAT-P-17b (4.5 μm only), and HAT-P-26b (3.6 μm only) we show the 2σ upper limit on the eclipse depth. We also overplot the IRAC 3.6 and 4.5 μm response functions in gray in the bottom panel for comparison.

Planet	Mass (M_{Jup})	Radius (R_{Jup})	T_{eq} (K)	T_{Bright} Ratio	Bulk Z_{planet}	[Fe/H]$_*$	Ref
GJ 436b	0.07 ± 0.01	0.37 ± 0.02	669 ± 22	< 0.72	0.83 ± 0.02	0.05 ± 0.141	1,2,3,4
GJ 3470b	0.0432 ± 0.0051	0.346 ± 0.029	604 ± 98	< 1.00	0.74 ± 0.37	0.27 ± 0.11	5,6,7
HAT-P-12b	0.21 ± 0.01	$0.96^{+0.03}_{-0.02}$	963 ± 16	$1.06^{+0.08}_{-0.10}$	0.32 ± 0.03	-0.26 ± 0.06	1,8,9,10
HAT-P-17b	0.537 ± 0.017	1.010 ± 0.029	791±17	<0.87	0.13 ± 0.04	0.05 ± 0.03	1,10,11
HAT-P-18b	0.200 ± 0.019	0.995 ± 0.052	822 ± 22	$0.78^{+0.08}_{-0.09}$	0.24 ± 0.05	0.10 ± 0.08	1,10,11
HAT-P-19b	0.292 ± 0.018	1.132 ± 0.072	1010 ± 42	0.84 ±0.06	0.22 ± 0.05	0.29 ± 0.06	1,10,12,13
HAT-P-20b	7.25 ± 0.19	0.87 ± 0.03	970 ± 23	$1.00^{+0.03}_{-0.04}$	0.28 ± 0.05	0.12 ± 0.15	1,10,14,15
HAT-P-26b	0.059 ± 0.007	$0.565^{+0.072}_{-0.032}$	1028 ± 21	> 1.15	0.66 ± 0.03	0.01 ± 0.04	1,10,11
WASP-8b	$2.24^{+0.08}_{-0.09}$	$1.04^{+0.01}_{-0.05}$	948 ± 22	0.73 ±0.06	0.11 ± 0.04	0.29 ± 0.03	1,10,16
WASP-10b	3.14 ± 0.27	$1.039\,^{+0.043}_{-0.049}$	972 ± 31	0.94± 0.03	0.12 ± 0.02	0.04 ± 0.05	1,2,10,13
WASP-67b	0.406 ± 0.035	1.091 ± 0.046	1003 ± 20	>0.97	0.2 ± 0.06	0.18 ± 0.06	1,10,13,17
WASP-69b	0.250 ± 0.023	1.057 ± 0.047	961 ± 20	0.85 ± 0.02	0.21 ± 0.04	0.30 ± 0.06	1,10,11
WASP-80b	0.54 ± 0.04	1.00 ± 0.03	825 ± 19	0.99 ± 0.10	0.17 ± 0.04	0.13 ± 0.11	1,7,9,18

Table 2.4: Brightness Temperature Ratios

References. (1) Thorngren et al. (2016), Thorngren and Fortney (2019), (2) Southworth (2011), (3) Morley et al. (2017), (4) [Fe/H] from Rojas-Ayala et al. (2012), (5) Biddle et al. (2014), (6) Benneke et al. (2019), (7) [Fe/H] from Terrien et al. (2015), (8) Hartman et al. (2009), (9) Wong et al. (2019, in preperation), (10) [Fe/H] from Santos et al. (2013), Sousa et al. (2018), (11) This work, (12) Hartman, Bakos, Sato, et al. (2011), (13) Kammer et al. (2015), (14) Bakos et al. (2011), (15) Deming et al. (2015), (16) Cubillos et al. (2013), (17) Mancini et al. (2014), (18) Triaud et al. (2015)

We note that the presence or absence of a temperature inversion might also alter a planet's relative brightness in these two bands in a way that mimics the shift from a CH_4-dominated to CO- and CO_2-dominated carbon chemistry. Observations of the broader sample of hot Jupiters suggests that temperature inversions are only found in the atmospheres of the most highly irradiated planets and are most likely caused by the presence of gas phase TiO (e.g., Evans et al., 2017; Nugroho et al., 2017; Sedaghati et al., 2017; Sheppard et al., 2017). The planets in this study are too cool for TiO and VO to remain in the gas phase, and there is currently no evidence for temperature inversions in the atmospheres of planets at these temperatures.

Two of the Neptune-mass planets in our sample, GJ 436b and HAT-P-26b, have previously published constraints on their atmospheric metallicities and C/O ratios. Morley et al. (2017) re-examined all of the available secondary eclipse data for GJ 436b, which has a low 4.5-3.6 μm brightness temperature ratio. They concluded that these observations were consistent with absorption features from water, carbon monoxide, and carbon dioxide corresponding to an atmospheric metallicity greater than 200× solar and a C/O ratio consistent with solar. Similarly, transmission spectroscopy for HAT-P-26b from Wakeford et al. (2017) constrains its atmospheric metallicity to $0.8 - 26\times$ solar (1σ); this is consistent with our measurement of a relatively high 4.5-3.6 μm brightness temperature ratio. We therefore conclude that for these two planets, differences in atmospheric metallicity are likely the primary factor driving the observed difference in $3.6 - 4.5$ μm spectral slope, in good agreement with our predictions based on the model grids in Section 2.4.

We use the measured spectral slopes for our sample of planets to search for trends in spectral shape across our sample of short-period gas giant planets. If these planets have broadly solar C/O ratios and follow the same trend of increasing atmospheric metallicity with decreasing planet mass that we see for the solar system gas giants, we would expect to see a rising trend in the measured brightness temperature ratios with increasing planet mass. In Figure 2.10c, we plot this brightness temperature ratio as a function of planet mass for the four planets with measured eclipses described herein as well as other planets with temperatures less than 1100 K and published secondary eclipse detections (see Table 2.4). As before, we see that planets with eccentric orbits (GJ 436b, HAT-P-17b, and WASP-8b) appear to have brightness temperature ratios that are systematically lower than those of planets on circular orbits with the same mass. Other than this apparent clustering of eccentric planets, there appears to be no obvious correlation between atmospheric composition and

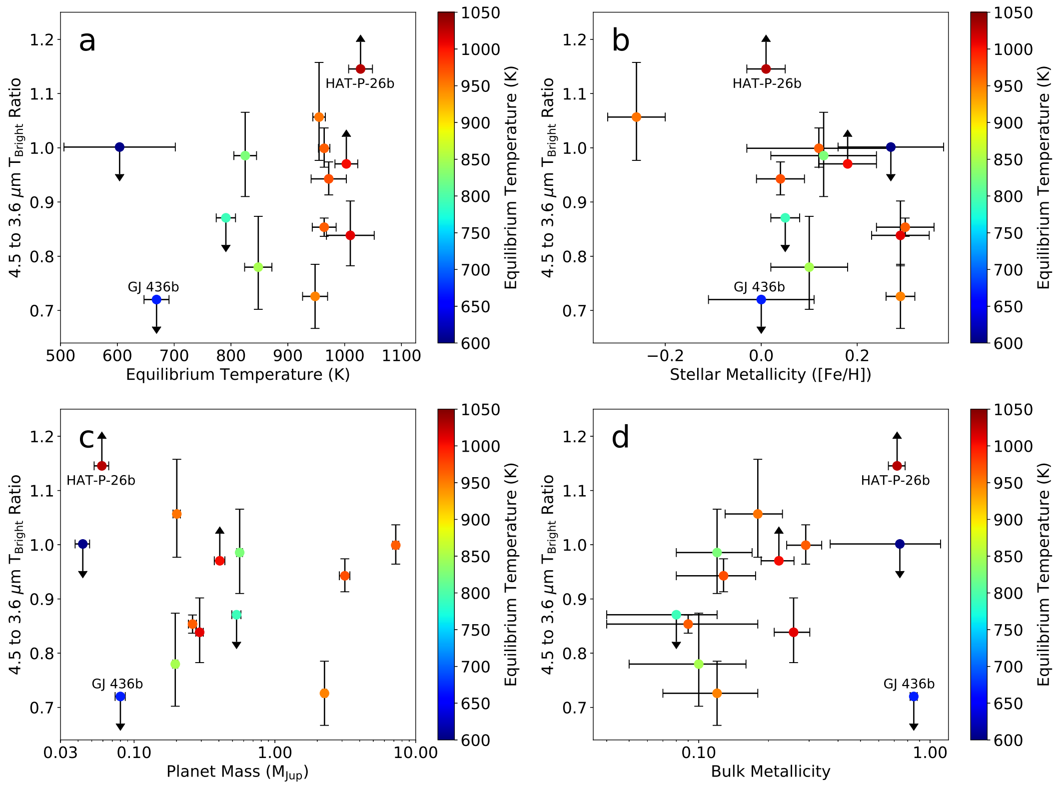

Figure 2.10: Measured 4.5-3.6 μm brightness temperature ratio as a function of (a) equilibrium temperature, (b) stellar metallicity, (c) planetary mass, and (d) bulk metallicity for all planets with published *Spitzer* eclipse depths and equilibrium temperatures less than 1100 K. We show four planets from this study (HAT-P-17b, HAT-P-18b, HAT-P-26b, and WASP-69b) as well as nine previously published planets (see Table 2.4 for the full list of planets and corresponding references). For planets with no eclipse detected in the 3.6 (4.5) μm bands we plot 2σ lower (upper) limits, respectively.

planetary mass for planets in this temperature regime.

We also check to see if the atmospheric compositions of these planets are correlated with their bulk metallicities. We take published bulk metallicity values from Thorngren and Fortney (2019), which used a 1D planetary model with an inert rock-ice core and a convective H/He-rock-ice envelope. We calculate new bulk metallicity values for GJ 3470b, which was not included in this study, using the same method (see Table 2.4). We find evidence for a correlation between atmospheric metallicity and bulk metallicity (Figure 2.10d, where planets with higher bulk metallicities have on average slightly higher 4.5-3.6 μm brightness temperature ratios. We evaluate the significance of the proposed trend in brightness temperature ratio versus bulk metallicity using a Monte Carlo simulation where we create a series of simulated data sets by sampling from the posterior probability distributions for each point. For the brightness temperature ratios, we assume that the reported uncertainties in the 3.6 and 4.5 μm brightness temperatures are reasonably well-approximated by Gaussian distributions. We then draw 10^6 samples from these two distributions for each planet.

For planets with a nondetection in one band, we assume that the brightness temperature in the band with the non-detection follows a Gaussian distribution with a standard deviation of 100 K centered at the assumed median of the distribution as determined from the brightness temperature corresponding to the eclipse depth of the reported 2σ upper limit (i.e., the center of the distribution is the brightness temperature corresponding to the 2σ upper limit - 200 K); this effectively excludes solutions in which the brightness temperature for the nondetection is unphysically low (i.e., 98% of all samples are limited to temperatures within 400 K of the 2σ upper limit). Lastly, we assume that the bulk metallicities are also well approximated by Gaussian distributions and sample from those as well.

If we exclude the three Neptune-mass planets (GJ 436b, GJ 3470b, and HAT-P-26b), we do find relatively weak (with positively sloped lines preferred over flat or negatively sloped lines at the 1.4σ level) evidence for a linear trend with bulk metallicity. If it can be substantiated with additional measurements, this correlation would be somewhat surprising as it would suggest that gas giant planets with high bulk metallicities may have lower atmospheric metallicities. This would be the opposite of the observed trend for the solar system gas giants, in which planets with higher bulk metallicities also have higher atmospheric metallicities.

Intriguingly, we do see tentative evidence for a trend in atmospheric composition with stellar metallicity (Figure 2.10b). This trend is not entirely surprising given that we would expect metal-rich stars to have correspondingly metal-rich disks. However, the metallicities of the host stars in our sample only vary between -0.26 and $+0.30$, corresponding to a relatively small $3.5\times$ change in bulk disk metallicity. In contrast, we would need to vary the atmospheric metallicities of these planets by more than two orders of magnitude to reproduce the observed change in 4.5-3.6 μm brightness temperature ratios. If real, this trend suggests that gas giant planets in metal-rich disks incorporate disproportionately more solids into their atmospheres than planets in metal-poor disks. If we assume that these planets formed in the inner disk, this might be explained by scenarios in which gas drag causes approximately centimeter-sized particles to migrate inward, increasing the concentration of solids in this region (e.g., Johansen et al., 2014).

We evaluate the significance of this proposed trend in the same manner as before (i.e., by drawing 10^6 samples from the distributions for the brightness temperatures as described above) and assuming that the reported stellar metallicities are well approximated by Gaussian distributions. We then fit the resulting 10^6 simulated data sets with a linear function and plot the corresponding posterior probability distributions for the slope and y intercept of this line (Figure 2.11). We find conflicting literature values for the metallicity of the M-dwarf stars in our sample (GJ 436, GJ 3470, and WASP-80), many of which also have relatively large uncertainties. We therefore opted to exclude these M-dwarf hosts when evaluating the significance of the proposed trend (Rojas-Ayala et al., 2012; Terrien et al., 2012; Lindgren and Heiter, 2017). We find that negative slopes are preferred, but our data are still consistent with a positive sloped or flat line at the 1.9σ level.

We also consider a scenario in which the points shown in Figure 2.11 do not follow a smooth trend, but rather comprise two distinct groups of planets– those with high atmospheric metallicities and those with low atmospheric metallicities. We follow the same approach as Schlaufman (2018) and try a hierarchical clustering algorithm, a k-means clustering algorithm, and a Gaussian-model clustering algorithm. All three algorithms are available as part of the `scikit-learn` package (Pedregosa et al., 2011). We find that these three methods were inconclusive as to the membership of the planets within the two groups, indicating that these measurements are consistent with a single population.

2.5 Conclusions

We present new secondary eclipse depth measurements in the 3.6 and 4.5 μm *Spitzer* bands for HAT-P-17b, HAT-P-18b, HAT-P-26b, and WASP-69b and place upper limits on the eclipse depths of HAT-P-15b. Our measured times of secondary eclipse for HAT-P-18b, HAT-P-26b, and WASP-69b are consistent with circular orbits, and we confirm the non-zero eccentricity of HAT-P-17b. We compare our measured eclipse depths with 1D radiative-convective models for each planet. For HAT-P-26b, which was the only planet with a well-constrained atmospheric metallicity from transmission spectroscopy, our data are in good agreement with the low atmospheric metallicity reported in Wakeford et al. (2017). We find no evidence for a correlation between atmospheric composition and planetary mass. However, we do find a suggestive 1.9σ trend in atmospheric composition as a

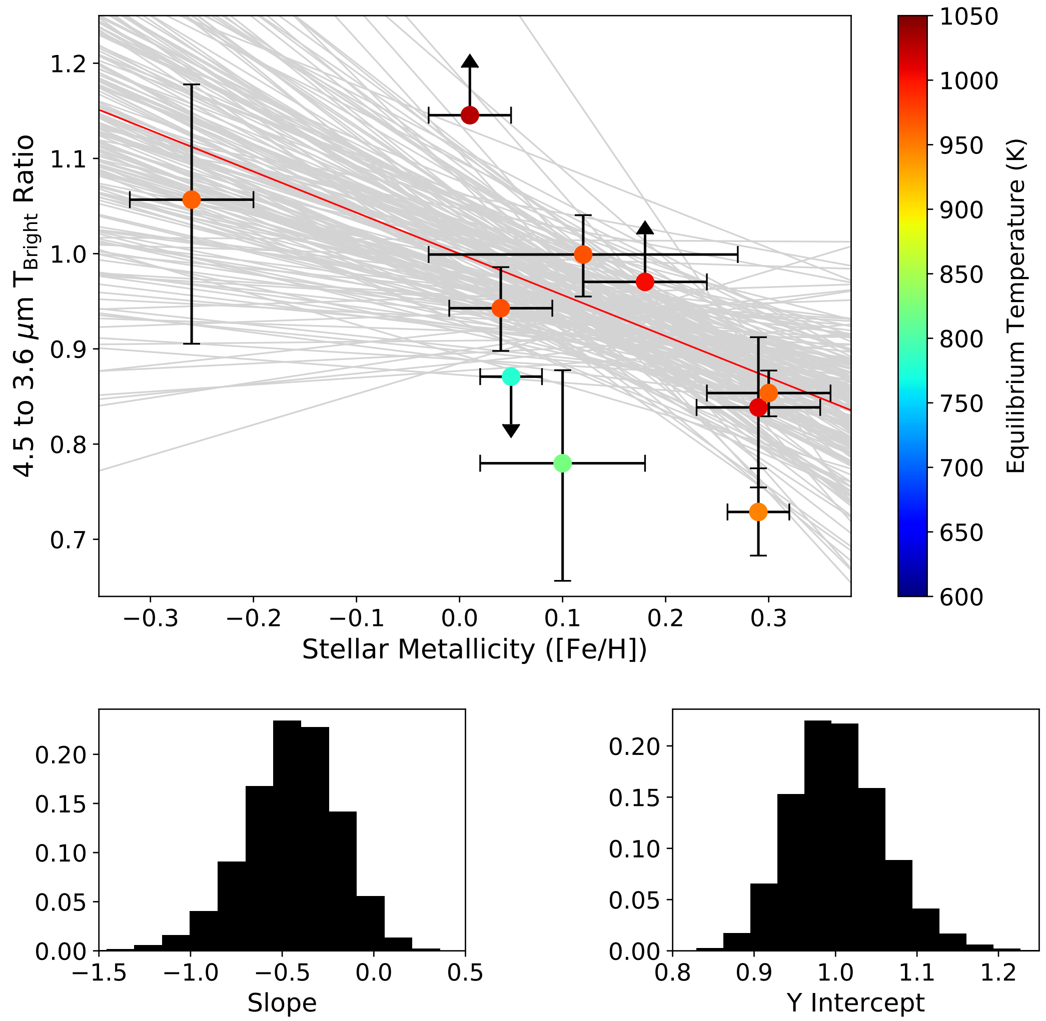

Figure 2.11: Measured 4.5 μm to 3.6 μm brightness temperature ratio as a function of stellar metallicity. We create 10^6 simulated data sets by sampling from posterior probability distributions for the reported brightness temperatures and stellar metallicities, and show a random subset of the resulting distribution of linear fits as gray lines. We indicate the median linear solution in red, and plot the corresponding distributions in y intercept and slope below.

function of stellar metallicity. While the existence of a correlation between planetary atmospheric composition and stellar metallicity would not be surprising, the strength of the observed trend implies that short-period gas giant planets orbiting metal-rich stars may have atmospheric metallicities that are significantly higher than the bulk metallicity of the disk. However, our ability to fully understand this possible trend is limited by the availability of precise stellar metallicity measurements.

Beginning in 2021, the broad infrared wavelength coverage and higher spectral resolution of the *James Webb Space Telescope* (*JWST*) will provide invaluable new insights into the atmospheric compositions of this population of planets (see Figure 2.12 for the expected JWST precision and coverage). In this study, we relied on broad photometric bandpasses that span multiple absorption features including water, methane, carbon monoxide, and carbon dioxide. This necessarily results in degeneracies in the interpretation of these data, including correlations between the abundances of the various molecular species and also with the planet's dayside pressure-temperature profile. *JWST* will be able to resolve individual molecular bands, therefore avoiding these degeneracies and allowing for robust abundance constraints for these atmospheres. It is worth noting that these cooler planets are also ideal targets for studies examining trends in bulk metallicity as a function of planet mass (e.g., Miller and Fortney, 2011; Thorngren et al., 2016), as hotter planets have inflated radii that make it difficult to accurately determine their bulk metallicities (e.g., Laughlin et al., 2011; Thorngren and Fortney, 2018). We therefore expect that future studies of this cool gas giant population with *JWST* will be able to determine for the first time whether or not the postulated correlation between planet mass, core mass fraction, and atmospheric metallicity is in fact a universal property of all gas giant planets. This in turn will tell us whether or not the interior and atmospheric compositions of gas giant planets are the inevitable outcome of the core accretion process or instead primarily reflect the diverse formation locations and disk properties of these planets.

2.6 Appendix

We show the individual normalized raw light curves for each visit of HAT-P-15b, HAT-P-17b, HAT-P-18b, HAT-P-26b, and WASP-69b in Figures 2.13— 2.15. For each of the visits, we overplot the best-fit instrumental noise model derived from the joint fits. We then show these same individual light curves with the instrumental noise models removed in Figures 2.16— 2.18 and overplot the best-fit eclipse model derived from the joint fits. We show the standard deviation of the residuals after removing both the eclipse and noise models from each visit for each planet in Figures 2.19— 2.21. The predicted photon noise for each visit is overplotted for reference.

We show the mixing-ratio profiles for relevant species of interest for a 1× and 100× solar metallicity model for HAT-P-17b (Figures 2.22 and 2.23, respectively) and a 1× and 100× solar metallicity model for HAT-P-26b (Figures 2.24 and 2.25, respectively). We show both equilibrium and disequilibrium chemical models derived using the same framework as presented in Moses et al. (2011), Moses, Line, et al.

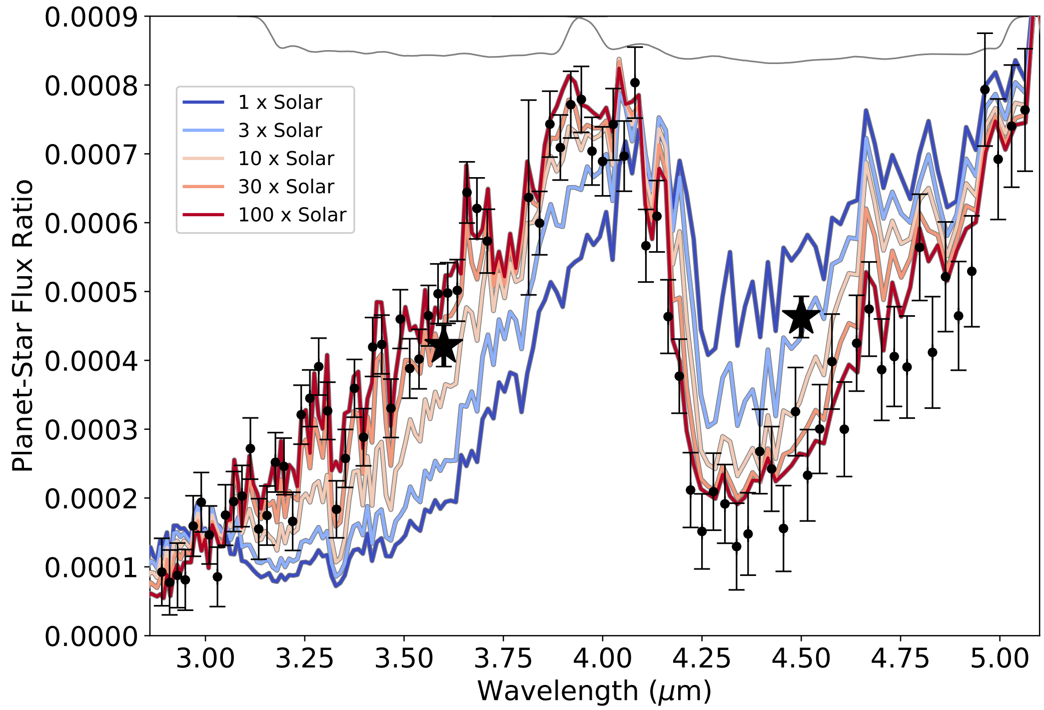

Figure 2.12: Simulated JWST observations of a single secondary eclipse observation of WASP-69b using the NIRSpec G395 grism (black points). We use our best-fit 100× solar metallicity model for this simulation and overplot models with 1×, 3×, 10× and 30× solar metallicities for comparison (all with solar C/O ratios). The IRAC 3.6 and 4.5 μm response functions are shown in gray and our measured eclipse depths in the two *Spitzer* bands are shown as filled black stars.

(2013), and Moses et al. (2016).

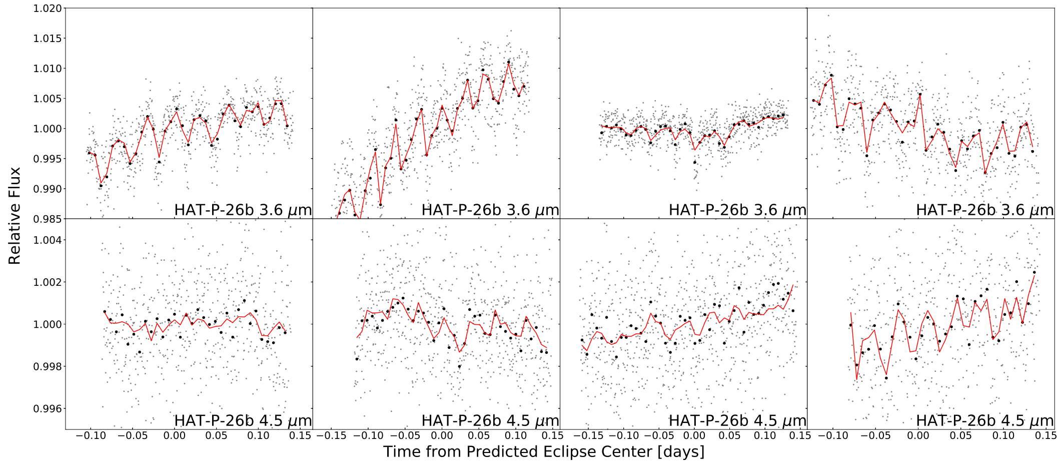

Figure 2.13: Raw *Spitzer* photometry for each visit of HAT-P-26b. The normalized flux binned in ten-minute intervals is shown in black and the thirty-second binned flux is shown in gray. Overplotted is the best-fit instrumental model in red. Observations are shown in chronological order across each row.

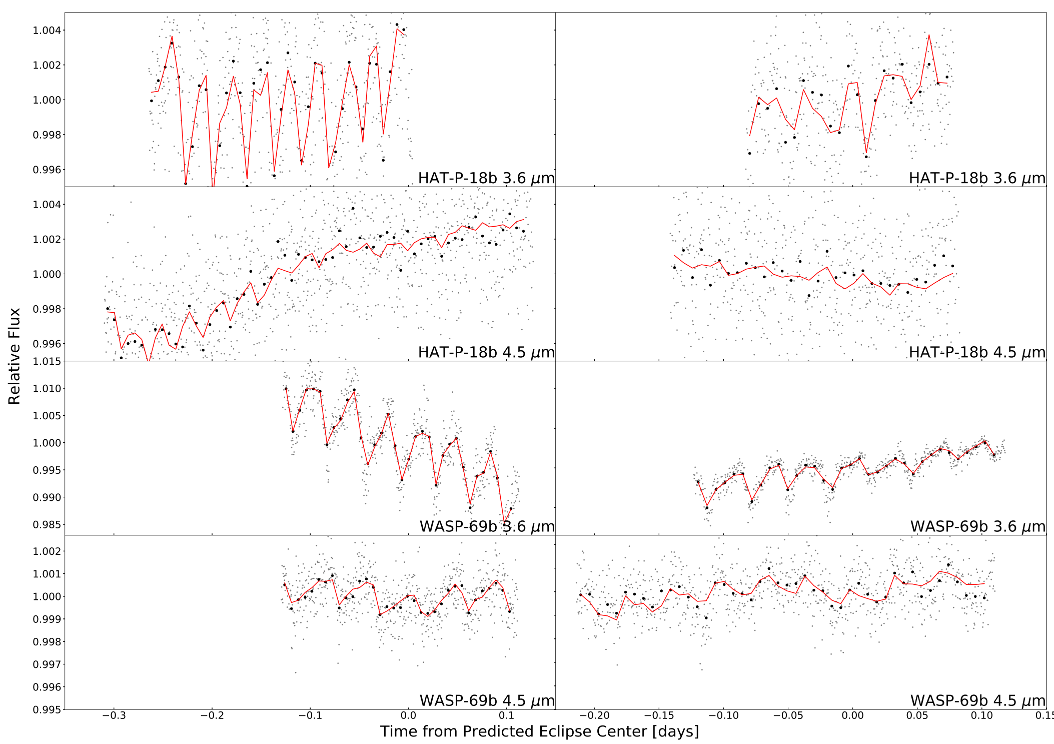

Figure 2.14: Raw *Spitzer* photometry for each visit of HAT-P-18b and WASP-69b. The normalized flux binned in ten-minute intervals is shown in black and the thirty-second binned flux is shown in gray. Overplotted is the best-fit instrumental model in red. Observations are shown in chronological order across each row.

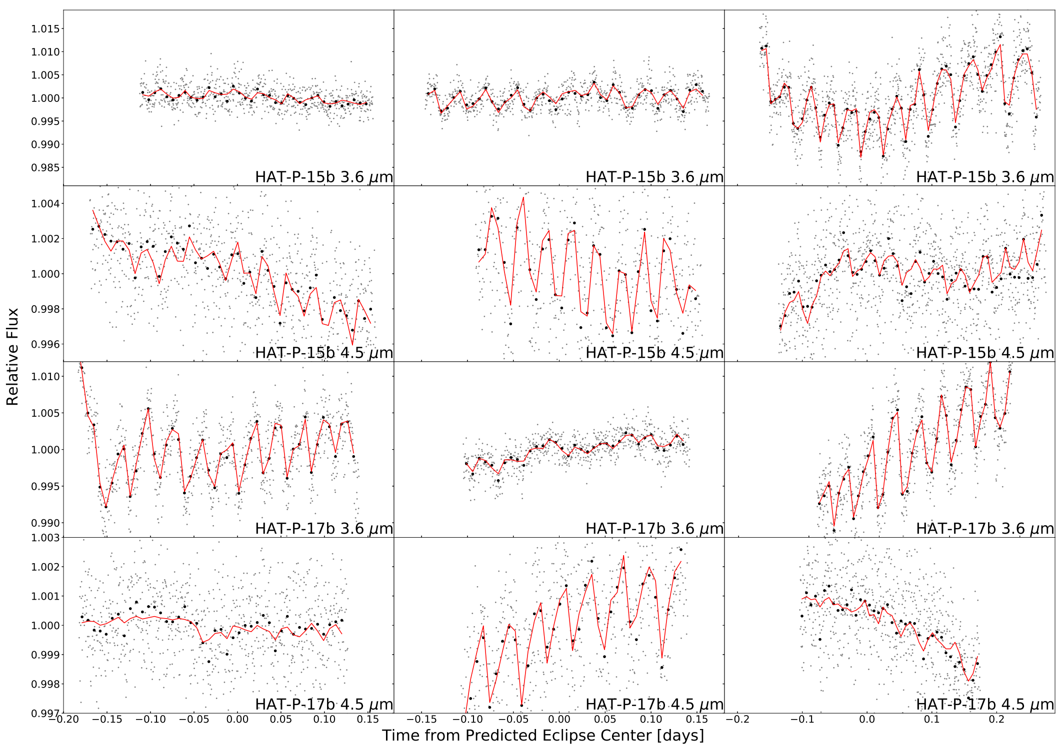

Figure 2.15: Raw *Spitzer* photometry for each visit of HAT-P-15b and HAT-P-17b. The normalized flux binned in ten-minute intervals is shown in black and the thirty-second binned flux is shown in gray. Overplotted is the best-fit instrumental model in red. Observations are shown in chronological order across each row.

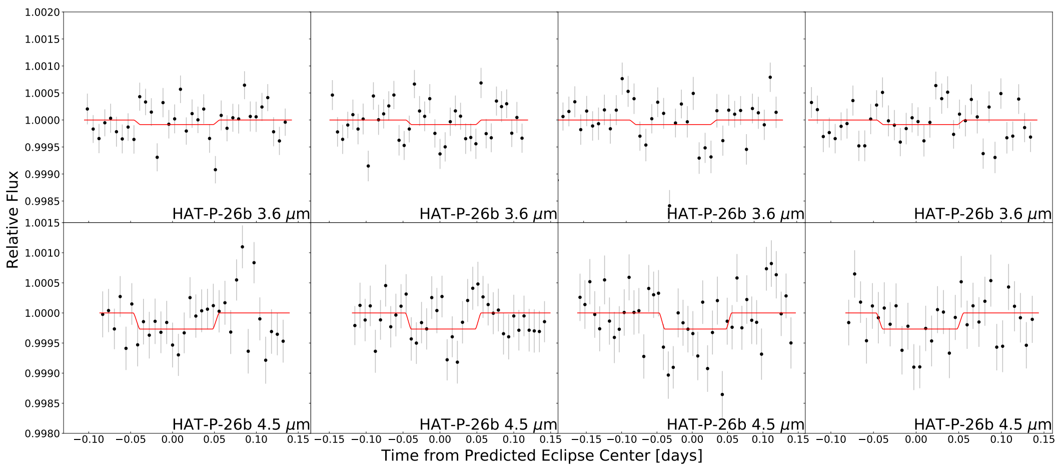

Figure 2.16: Individual light curves for each visit of HAT-P-26b. The ten-minute binned normalized flux in shown in black with error bars showing the standard error of the flux in each bin. The instrumental best-fit parameters are unique to each visit and have been divided out. The red lines are the light curves with the best-fit parameters from the joint fits. Observations are shown in chronological order across each row. The 2σ upper limits for the best-fit eclipse depths of the 3.6 μm visits are shown.

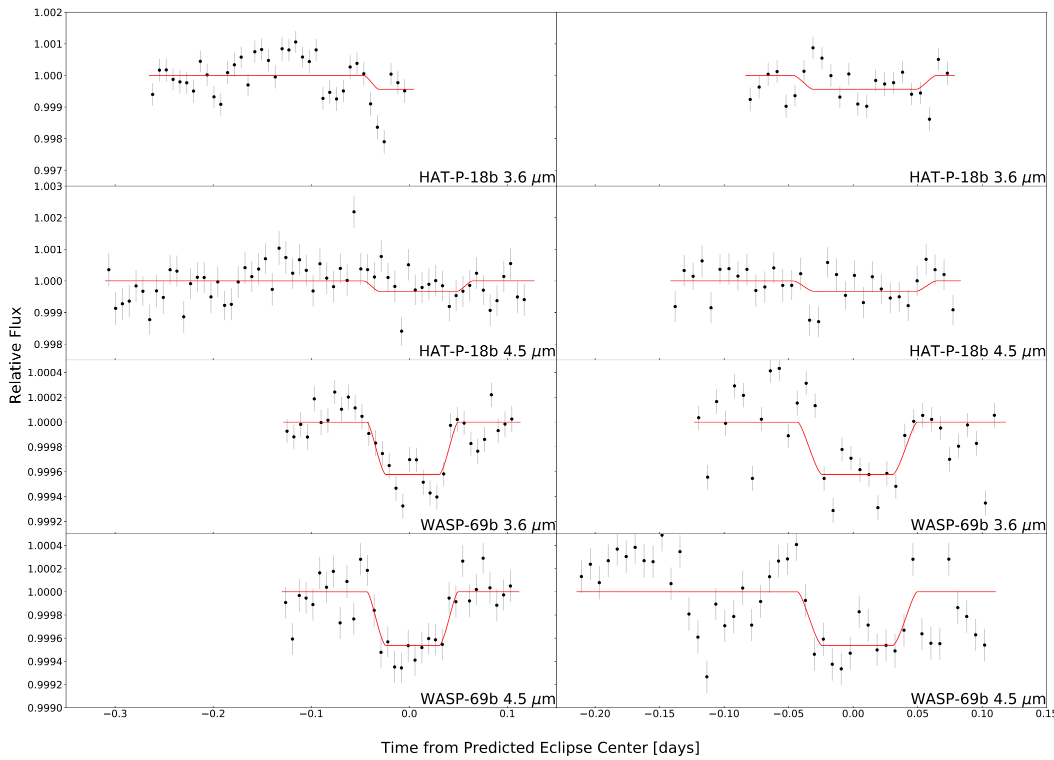

Figure 2.17: Individual light curves for each visit of HAT-P-18b and WASP-69b. The ten-minute binned normalized flux in shown in black with error bars showing the standard error of the flux in each bin. The instrumental best-fit parameters are unique to each visit and have been divided out. The red lines are the light curves with the best-fit parameters from the joint fits. Observations are shown in chronological order across each row.

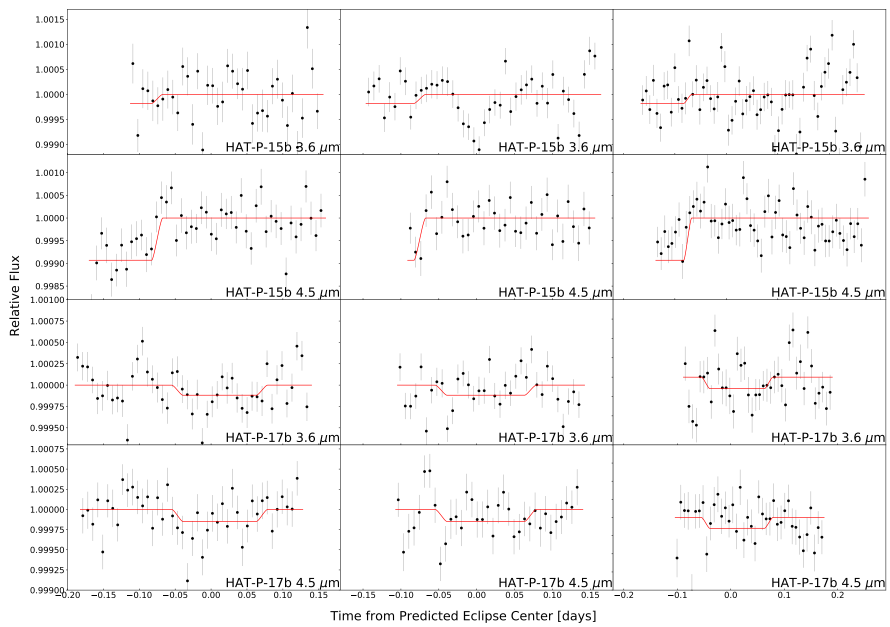

Figure 2.18: Individual light curves for each visit of HAT-P-15b and HAT-P-17b. The ten-minute binned normalized flux in shown in black with error bars showing the standard error of the flux in each bin. The instrumental best-fit parameters are unique to each visit and have been divided out. The red lines are the light curves with the best-fit parameters from the joint fits. Observations are shown in chronological order across each row. The 2σ upper limits for the best-fit eclipse depths of all visits of HAT-P-15b (see Section 2.2 for more details), and the 4.5 μm visits of HAT-P-17b are shown.

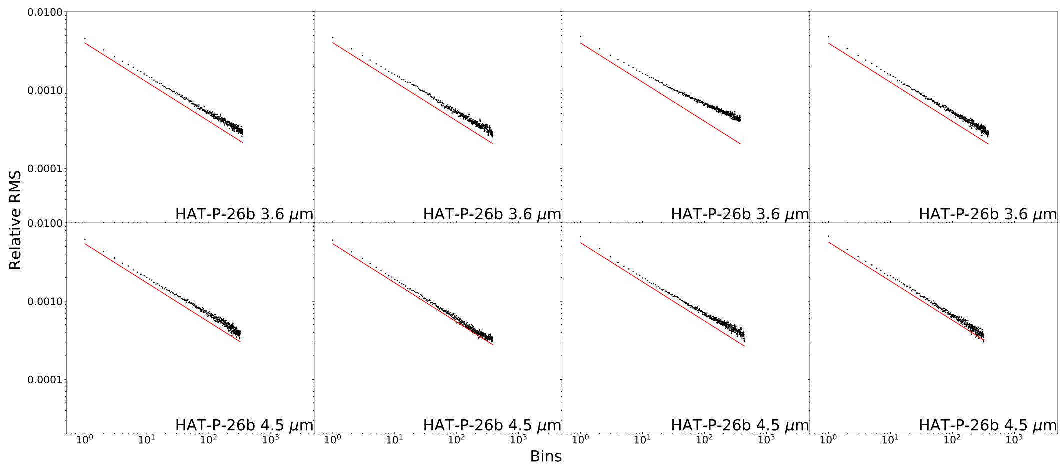

Figure 2.19: Standard deviation of the residuals of each visit of HAT-P-26b after removing the best-fit instrumental and astrophysical models as a function of bin size. The solid lines show the photon noise limits as a function of bin size scaled by $1/\sqrt{N}$. Observations are shown in chronological order across each row.

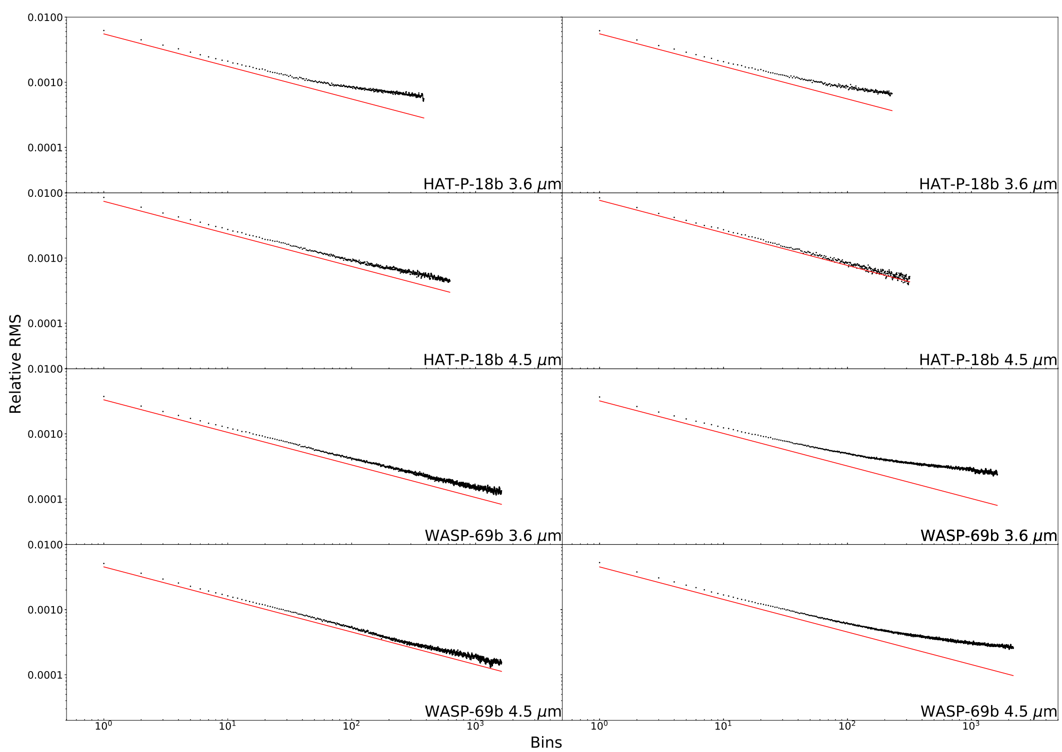

Figure 2.20: Standard deviation of the residuals of each visit of HAT-P-18b and WASP-69b after removing the best-fit instrumental and astrophysical models as a function of bin size. The solid lines show the photon noise limits as a function of bin size scaled by $1/\sqrt{N}$. Observations are shown in chronological order across each row.

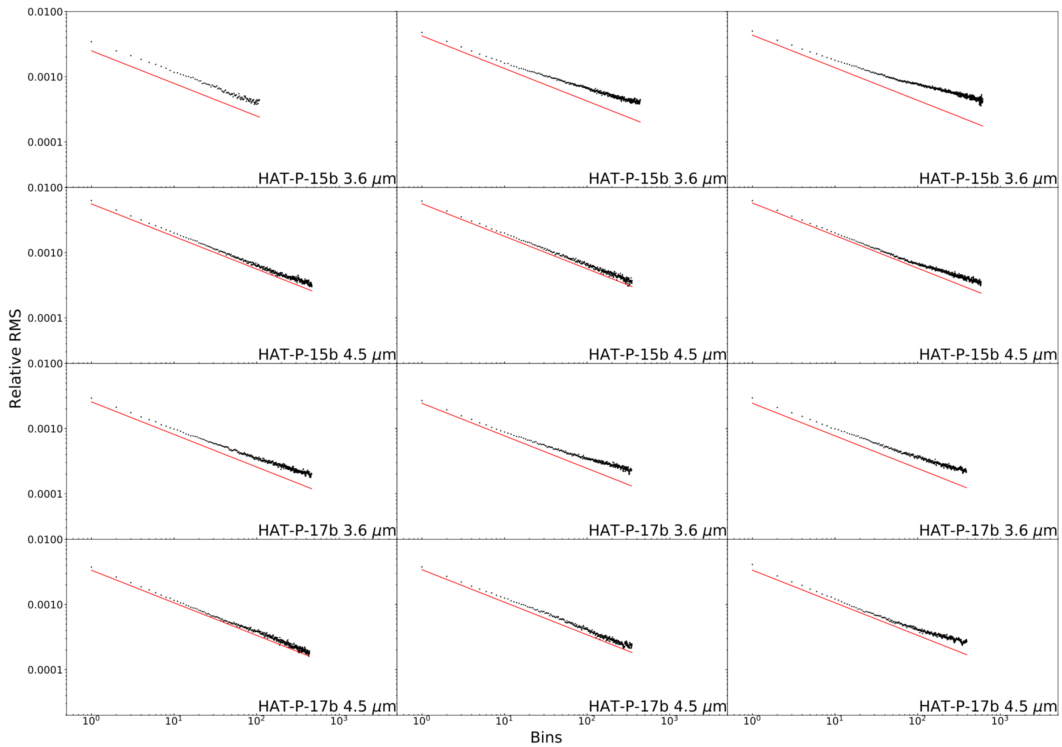

Figure 2.21: Standard deviation of the residuals of each visit of HAT-P-15b and HAT-P-17b after removing the best-fit instrumental and astrophysical models as a function of bin size. The solid lines show the photon noise limits as a function of bin size scaled by $1/\sqrt{N}$. Observations are shown in chronological order across each row.

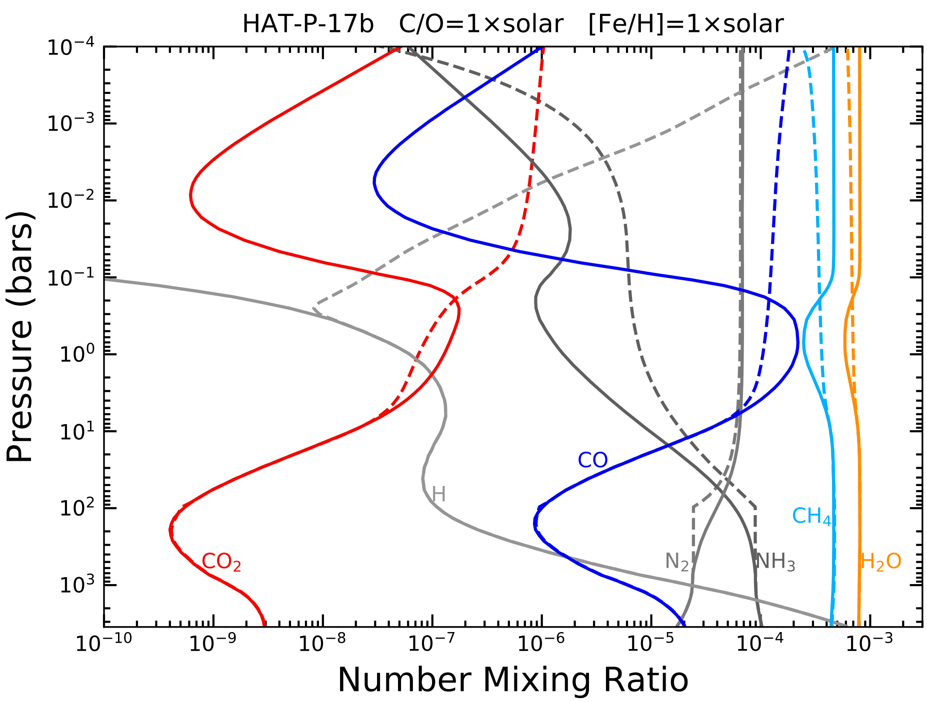

Figure 2.22: Mixing ratio profiles derived using the same framework as presented in Moses et al. (2011), Moses, Line, et al. (2013), and Moses et al. (2016) for relevant species of interest for a 1× solar metallicity equilibrium (solid lines) and disequilibrium (dashed lines) model with solar C/O ratios for HAT-P-17b.

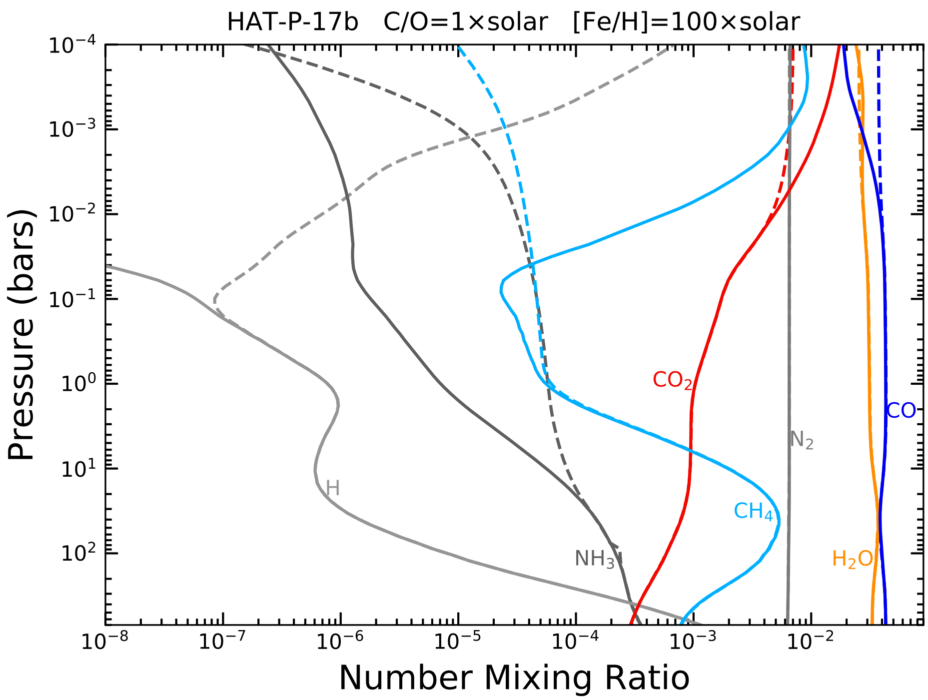

Figure 2.23: Mixing ratio profiles derived using the same framework as presented in Moses et al. (2011), Moses, Line, et al. (2013), and Moses et al. (2016) for relevant species of interest for a 100× solar metallicity equilibrium (solid lines) and disequilibrium (dashed lines) model with solar C/O ratios for HAT-P-17b.

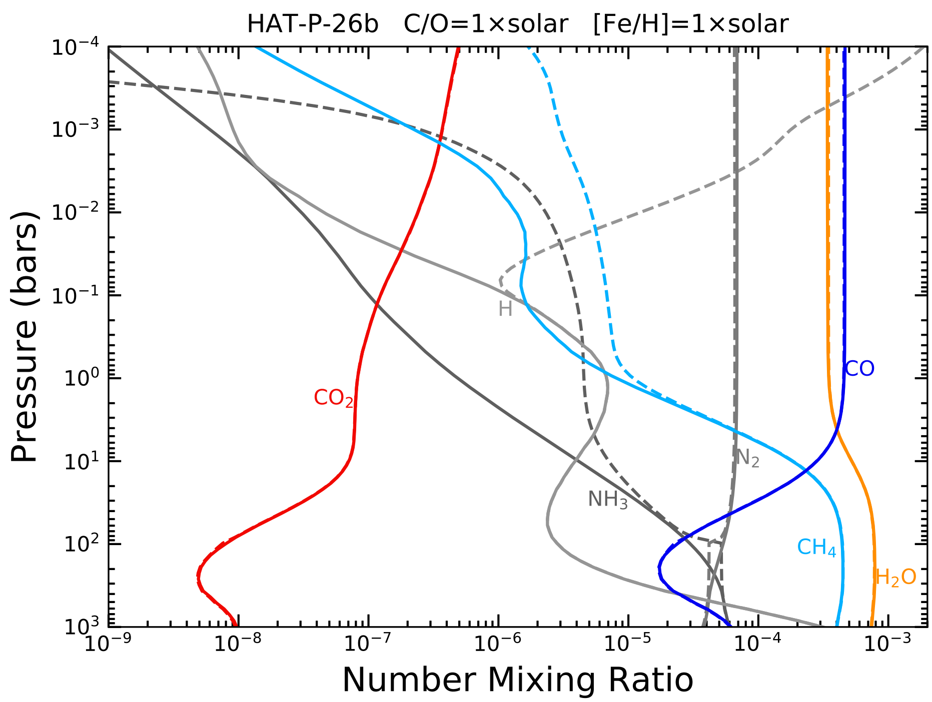

Figure 2.24: Mixing ratio profiles derived using the same framework as presented in Moses et al. (2011), Moses, Line, et al. (2013), and Moses et al. (2016) for relevant species of interest for a 1× solar metallicity equilibrium (solid lines) and disequilibrium (dashed lines) model with solar C/O ratios for HAT-P-26b.

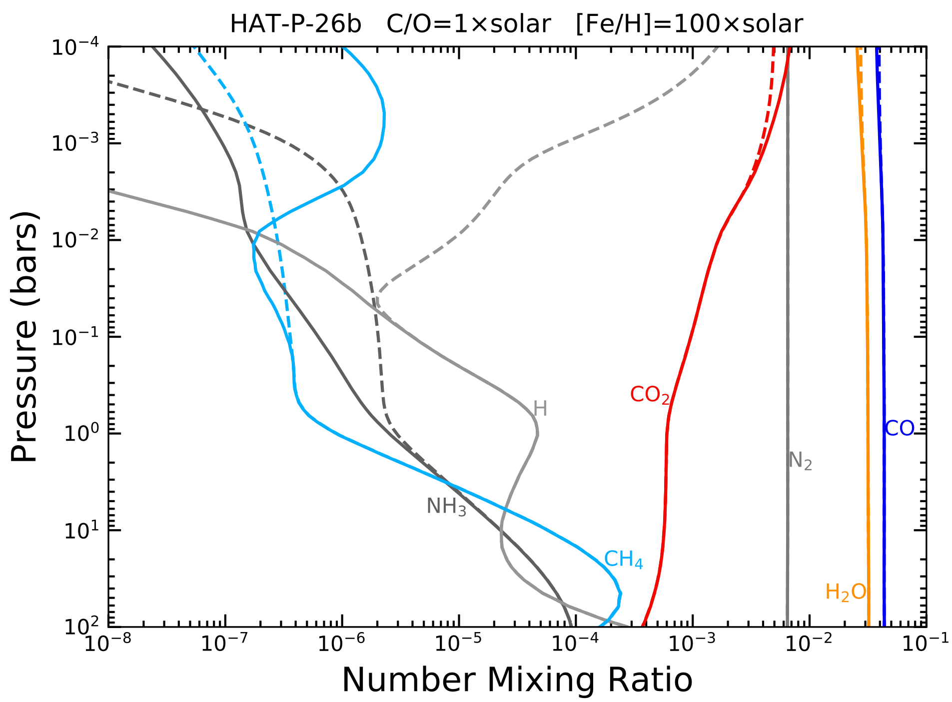

Figure 2.25: Mixing ratio profiles derived using the same framework as presented in Moses et al. (2011), Moses, Line, et al. (2013), and Moses et al. (2016) for relevant species of interest for a 100× solar metallicity equilibrium (solid lines) and disequilibrium (dashed lines) model with solar C/O ratios for HAT-P-26b.

Chapter 3

TRENDS IN *SPITZER* SECONDARY ECLIPSES

Wallack, N. L., Knutson, H. A., & Deming, D. (2021). Trends in Spitzer Secondary Eclipses. *The Astronomical Journal*, *162*(1), 36. https://doi.org/10.3847/1538-3881/abdbb2.

3.1 Introduction

For short-period gas giant planets with hydrogen-rich envelopes, the amount of incident flux received from the star is predicted to be the primary factor that determines the shape of their observed dayside emission spectra (e.g., Fortney et al., 2008; Burrows et al., 2008). We expect these short-period planets to be tidally locked, where the efficiency of day-night circulation varies as a function of the incident flux (e.g., Komacek and Showman, 2016). This atmospheric circulation in turn determines the temperature of the upper region of the dayside atmosphere, which sets the equilibrium chemistry and corresponding atmospheric composition (e.g., Heng and Marley, 2018). Although photochemistry and mixing from the nightside and deep interior can alter this default chemistry, these effects are predicted to be below the sensitivity of current observations for the majority of planets observed to date (e.g., Moses, 2014). Condensate clouds can also alter the observed atmospheric properties of these planets, but the effects of these clouds are expected to be less pronounced for dayside thermal emission spectra than for transmission spectroscopy (e.g., Fortney, 2005).

Observations of the secondary eclipse, when the planet passes behind its host star, allow us to probe the thermal emission spectra of transiting gas giant planets. This has enabled detailed studies of a handful of planets (e.g., Brogi et al., 2017; Morley et al., 2017; Kreidberg et al., 2018), but there are relatively few planets with such extensive secondary eclipse data sets. If we broaden our focus to planets with just a few broadband photometric measurements from *Spitzer*, we can search for broader population-level trends. Previous studies of dayside emission spectra confirm that hotter planets do indeed have less efficient heat redistribution (Schwartz and Cowan, 2015; Garhart et al., 2020), in good agreement with predictions from atmospheric circulation models (Perez-Becker and Showman, 2013; Komacek and Showman, 2016). Garhart et al. (2020) additionally found evidence for a systematic shift in the 3.6 − 4.5 μm spectral slopes of these planets as a function of incident flux, which suggests that the atmospheric chemistries and pressure-temperature profiles of these planets also vary as a function of the irradiation. However, this study found that neither of the two most commonly utilized model atmosphere grids was able to accurately predict the increase in the observed ratio of 3.6 μm and 4.5 μm brightness temperatures with increasing equilibrium temperature, suggesting that these models can be further improved.

To date, most published population-level studies of transiting gas giant planet emission spectra have focused on searching for correlations with the incident flux (e.g., Cowan and Agol, 2011; Schwartz and Cowan, 2015; Schwartz et al., 2017; Garhart et al., 2020; Baxter et al., 2020). However, we expect that planets with the same incident flux levels might nonetheless possess distinct thermal spectra if they have different atmospheric metallicities and/or surface gravities, both of which can alter their atmospheric chemistries, circulation patterns, and cloud properties. In a previous study (Wallack et al., 2019), we focused on the sub-population of planets cooler than $\sim$ 1000 K, which are expected to undergo a particularly distinct shift in atmospheric chemistry as a function of atmospheric metallicity and C/O ratio (e.g., Moses, Madhusudhan, et al., 2013; Drummond et al., 2018). In this study, we broaden our focus to the full sample of transiting gas giant planets with *Spitzer* secondary eclipse detections in order to determine whether or not there are additional parameters beyond incident flux that might help to explain the observed diversity of dayside emission spectra. These same factors might also provide new insights into how to modify standard atmosphere model grids in order to better match the observed trends in spectral shape as a function of incident flux.

	HAT-P-5b	HAT-P-38b	WASP-7b	WASP-72b	WASP-127b
T_* (K)	5960±100	5330±100	6520±70	6250±100	5750±100
$[Fe/H]_*$	0.24±0.15	0.06±0.1	0.00±0.10	-0.06±0.09	-0.18±0.06
Mass (M_{Jup})	1.06 ±0.11	0.267±0.020	0.98±0.13	$1.461^{+0.059}_{-0.056}$	$0.165^{+0.021}_{-0.017}$
Radius (R_{Jup})	1.252±0.043	$0.825^{+0.092}_{-0.063}$	1.374±0.094	1.27±0.20	$1.311^{+0.025}_{-0.029}$
T_{equ} (K)^a	1517±37	1080^{+60}_{-45}	1530±50	2204^{+139}_{-115}	1404±29
e^b	<0.072 (<0.18)	<0.055 (<0.17)	<0.049 (<0.11)	<0.017 (<0.038)	0
ω (deg)^b	...	...	...	...	...
Period (days)^c	2.78847360 (52)	4.640382 (32)	4.9546416 (35)	2.2167421 (81)	4.17807015 (57)
T_c	5432.45510 (10)	5863.12034 (35)	5446.63493 (30)	5583.6528 (21)	7248.741276 (68)
References	1,2,3,4,5	1,5,6	1,5,7,8	1,5,9	5,10,11

Table 3.1: System Properties for New Planets in this Study

[a] Calculated assuming planet-wide heat circulation and zero albedo.

[b] The orbital eccentricity e and longitude of periapse ω are derived from fits to radial velocity data.

[c] (BJD-2,450,000) Uncertainties on the last two digits are parenthesized.

(1) Bonomo et al. (2017), (2) Southworth et al. (2012), (3) Bakos et al. (2007), (4) Torres et al. (2008), (5) Southworth (2011), (6) Sato et al. (2012), (7) Albrecht et al. (2012), (8) Hellier et al. (2009), (9) Gillon et al. (2013), (10) Lam et al. (2017), (11) Chen et al. (2018)

Garhart et al. (2020) presented a uniform analysis of 3.6 and 4.5 μm *Spitzer* observations of 36 transiting hot Jupiters. We use 31 of these observations (those with detections above 2.5σ) and expand on this sample by leveraging an additional 42 planets with *Spitzer* 3.6 and 4.5 μm secondary eclipse detections (above 2.5σ) from the literature as well as adding secondary eclipse measurements for three of our five new planets: HAT-P-5b (Bakos et al., 2007), WASP-7b (Hellier et al., 2009), and WASP-127b (Lam et al., 2017). HAT-P-38b (Sato et al., 2012) and WASP-72b (Gillon et al., 2013) do not have detections in both bandpasses. With this newly expanded sample we proceed to revisit previously established correlations between spectral shape and incident flux, and search for additional correlations with stellar metallicity and surface gravity. In Section 3.2, we describe our photometric extraction and model fits. In Section 3.3, we present new *Spitzer* secondary eclipse measurements of five new planets, and in Section 3.4, we add these new planets to the published *Spitzer* secondary eclipse measurements and investigate trends in the thermal emission spectra of the population of short-period gas giant planets.

3.2 Observations and Data Analysis

We obtained one secondary eclipse each in the IRAC 3.6 μm and 4.5 μm bands (Fazio et al., 2004) for HAT-P-5b (PID: 60021), WASP-7b (PID: 60021), WASP-72b (PID: 10102), and WASP-127b (PID: 13044) and two visits in each band for HAT-P-38b (PID: 12085). Aside from HAT-P-5b, all of these data were taken in the 32×32 pixel subarray mode with an initial 30 minute observation to allow for settling of the telescope followed by a peak-up pointing adjustment prior to the start of the science observation (Ingalls et al., 2012). HAT-P-5b and WASP-7b are the oldest data sets in this study and were observed before the peak-up pointing mode was fully implemented. Additionally, HAT-P-38b was observed in full array mode. See Table 3.1 and Table 3.2 for additional details.

Target	λ (μm)	UT Start Date	AOR	Length (h)	t_{int} (s)[a]	t_{trim} (h)[b]	r_{pos}[c]	r_{phot}[d]	n_{bin}[e]	RMS[f]
HAT-P-5b	3.6	2009 Oct 16	31757056	7.64	6.0	0.5	3.0	2.0	2	1.25
	4.5	2009 Oct 19	31751424	7.64	6.0	2.0	3.0	2.0	4	1.26
HAT-P-38b	3.6	2016 Apr 10	58238976	8.91	2.0	1.0	4.0	2.0	4	1.15
	3.6	2016 May 08	58241024	8.95	2.0	1.5	4.0	2.0	2	1.14
	4.5	2016 Apr 20	58238464	8.95	2.0	2.0	3.5	2.0	2	1.17
	4.5	2016 May 04	58241280	8.95	2.0	2.0	3.5	2.0	32	1.20
WASP-7b	3.6	2010 Jun 12	31770880	7.73	2.0	0.5[g]	3.0	5.0	2	1.39
	4.5	2010 Jun 27	31765248	7.73	2.0	0.5[g]	3.0	2.9	16	1.22
WASP-72b	3.6	2014 Nov 17	51816192	10.11	0.4	1.0	4.0	2.0	512	1.31
	4.5	2014 Nov 19	51842304	10.11	0.4	1.0	3.5	2.0	64	1.53
WASP-127b	3.6	2017 Aug 20	62161664	12.55	2.0	2.0	4.0	2.0	2	1.27
	4.5	2017 Sep 01	62162176	12.55	2.0	2.0	2.5	2.7	16	1.20

Table 3.2: *Spitzer* Observation Details

[a]Integration time

[b]Initial trim duration

[c]Radius of the aperture (in pixels) used to determine the location of the star on the array

[d]Radius of the aperture (in pixels) used for the photometry

[e]Bin size used for fits

[f]Ratio of measured RMS to photon noise limit

[g]WASP-7b has a time of secondary eclipse that is not well centered in the observation window, therefore in order to preserve as much of ingress as possible, we fix the trim duration to 30 minutes (see §3.2 for more details).

We utilize the standard Basic Calibrated Data (BCD) images for our analysis and extract photometric fluxes as described in our previous studies (i.e., Wallack et al., 2019). In brief, we first calculate the BJD_{UTC} mid-exposure times for each image, then estimate the sky background in each image by masking out a circular region with a radius of 15 pixels centered on the position of the star, iteratively trimming 3σ outliers, and fitting a Gaussian function to a histogram of the remainder of the pixels. We utilize flux-weighted centroiding (e.g., Knutson et al., 2008; Deming et al., 2015) with a circular aperture to determine the location of the star on the array, considering aperture radii ranging between 2.5 and 4.0 pixels in 0.5 pixel steps and optimize our choice of aperture as described below. We use the `aper` routine in the `DAOPhot` package (Stetson, 1987) to extract the total flux in a circular aperture centered on the position of the star, considering aperture sizes ranging from 2.0 to 3.0 pixels in steps of 0.1 pixels and from 3.0 to 5.0 pixels in steps of 0.5 pixels.

In order to mitigate the ramp-like behavior present at early times in some of the visits, we trim up to two hours of data from the beginning of each time series. We find that binning our data prior to fitting reduces the amount of time-correlated noise in the residuals (see Deming et al., 2015 and Kammer et al., 2015 for more details). In order to determine the optimal combination of flux-weighted centroiding aperture, photometric aperture, trim duration, and bin size for each visit, we fit a combined instrumental and astrophysical model to each version of the photometry and calculate the standard deviation of the residuals as a function of bin size stepping in powers of two (see Kammer et al., 2015 for further details). We then calculate the least-squares difference between the measured standard deviation of the residuals and the predicted photon noise limit in each bin, which decreases as the square root of the number of points. We then select the photometric and centroiding apertures, trim duration, and bin size that minimizes this least-squares difference (i.e., the one that is closest to the photon noise at all measured timescales) for use in our subsequent analysis.

Our model for each visit consists of a secondary eclipse light curve and an instrumental noise model, which we fit simultaneously. We calculate our eclipse model using the `batman` package (Mandel and Agol, 2002; Kreidberg, 2015), where we fix the planet-star radius ratio, orbital inclination, and the ratio of the orbital semi-major axis to the stellar radius (a/R_*) to the published values for each planet (see Table 3.1 for references) and allow the eclipse depth and time to vary as free parameters. Due to the fact that the orbital parameters are often more precisely measured from transit light curves than from secondary eclipse light curves, we are justified in fixing the orbital parameters to those measured from transit light curves instead of letting these parameters vary in our fits.

The dominant instrumental noise source for *Spitzer* timeseries photometry is intrapixel sensitivity variations (Reach et al., 2005; Charbonneau et al., 2005; Morales-Calderon et al., 2006), which cause the apparent flux from the star to vary as a function of its position on the pixel. We model this effect using the pixel-level decorrelation (PLD) method, which uses a linear combination of individual pixel-level light curves to account for trends due to variations in both the star's position on the array and the width of the stellar point spread function (Deming et al., 2015). As in Deming et al. (2015), we utilize a 3×3 grid of pixels centered on the location of the star and remove astrophysical flux variations in each 3×3 postage stamp by dividing by the summed flux across all nine pixels.

In the majority of our observations, we can fully account for additional time-dependent trends with the inclusion of a linear function of time once we have trimmed some data from the start of the observation. This is not true, however, for the 3.6 μm observation of WASP-72b or the 3.6 μm observation of WASP-7b. For the 3.6 μm observation of WASP-72b, we obtain the best fit using an exponential function of time. Using this exponential reduces the Bayesian Information Criterion (BIC) by 12. For the 3.6 μm observation of WASP-7b, we obtain the best fit using a quadratic function of time (ΔBIC of 66). For all fits we divide out our initial astrophysical model and use linear regression on the residuals to obtain an initial guess for the nine linear PLD coefficients in order to speed up convergence for these highly correlated parameters.

When optimizing our choice of photometry, we first fix the predicted time of eclipse to an orbital phase of 0.5 and run fits on each version of the photometry using a Levenberg-Marquardt minimization. We then select the optimal version of the photometry in each bandpass and carry out a simultaneous fit to all of the visits for a given planet, where we allow the orbital phase of the secondary eclipse to vary as a free parameter. We carry out these fits using the affine-invariant Markov chain Monte Carlo (MCMC) ensemble sampler `emcee` (Foreman-Mackey et al., 2013, 2019), where we allow the secondary eclipse depth to vary independently in each bandpass but assume a common eclipse phase. We place uniform priors on all free parameters and allow the eclipse depths to take on negative values so that we do not bias our eclipse depth estimates. We utilize 60 walkers for our fits, which is enough to ensure adequate sampling of the model parameter space. We initialize these walkers in a tight cluster centered on the best-fit solution from a joint Levenberg-Marquardt minimization and carry out an initial burn-in with a length of 10,000 steps. We then discard this initial burn-in and carry out a subsequent fit with 10^5 steps per chain. We then return to the original set of photometry options and repeat our optimization fixing the time of secondary eclipse to the median value from the MCMC chains. We adopt the resulting optimal photometry choices for each visit and rerun the MCMC for the joint fits.

We report the median values from our MCMC chains and the corresponding 1σ uncertainties in Table 3.3 and show the raw photometry for each visit with best-fit instrumental noise models from the joint fits overplotted in Figure 3.1. Normalized light curves for these visits with best-fit eclipse light curves overplotted are shown in Figure 3.2. In Figure 3.3 we combine all visits for HAT-P-38b and show the averaged light curves for each bandpass. The standard deviation of the residuals as a function of bin size for all visits are shown in Figure 3.4.

We alter our fitting procedure for WASP-7b, as there appears to be substantial correlated noise (i.e. the residuals do not scale with $\sqrt{n}$) in the residuals of the 3.6 μm data (see the WASP-7b 3.6 μm panel in Figure 3.4). To mitigate any biases in our best-fit parameters, we initially fit each of the channels for WASP-7b independently. We find that the best-fit secondary eclipse phases for each channel are consistent at the 1 sigma level, indicating that the correlated noise in the 3.6 μm data is likely not biasing our time of secondary eclipse in that channel.

We find that both the 3.6 and 4.5 μm data prefer an eclipse phase that is offset from the expected value for a circular orbit (see Section 3.3 for more details). As a result, the secondary eclipse is not centered in the observation, but instead occurs $78.8^{+5.0}_{-4.2}$ minutes early. In order to preserve as much of ingress as possible, we only trim 30 minutes from the beginning of each observation for this planet rather than considering a range of trim durations and optimizing to minimize the scatter in the residuals. We account for the effect of correlated noise on the 3.6 μm eclipse depth uncertainty by inflating the per-point errors (which are generally left as a free parameter in our fits) by a factor that reflects how much the variance of the residuals deviates from the expected white noise scaling (i.e. $1/\sqrt{n}$ where n is the number of points in each bin) at a characteristic timescale of 10 minutes (see Pont et al., 2006 and Lanotte et al., 2014 for more information). Because we are fitting binned light curves, we calculate this inflation factor as the amount of excess noise relative to the expected $\sqrt{n}$ scaling when we go from the binning timescale used in the fits to a binning timescale of 10 minutes (see Figure 3.4). We find that the resulting inflation factor is 2.1 for the 3.6 μm WASP-7b observation. We then take our best fit per-point error from the initial fit, multiply it by that factor, fix the per-point uncertainty to that value, and rerun our fit in order to obtain an updated eclipse depth and phase.

It is apparent in Figure 3.4 that several other observations also appear to have excess correlated noise. We calculate the inflation factor for each observation following the same process as described above, and implement a new version of the fit with an inflated per-point uncertainty for visits with inflation factors larger than 1.5. We find that correlated noise exceeding this threshold is present in both the 3.6 and 4.5 μm observations of WASP-72b (inflation factors of 1.5 and 2.0, respectively; see Figure 3.4) and both 3.6 μm observations of HAT-P-38b (inflation factors of 1.7 and 1.5 for the first and second observations, respectively). For WASP-72b, we do not detect the eclipse in the 3.6 μm bandpass, so we cannot compare the best-fit secondary eclipse phases from each channel in order to determine if this parameter is affected by correlated noise. However, the best-fit secondary eclipse phase from the 4.5 μm fit agrees with the prediction for a circular orbit, and the alternative scenario (slightly eccentric orbit biased by correlated noise to appear circular) seems unlikely.

3.3 Results

We report the best-fit eclipse depths and times and their corresponding uncertainties in Table 3.3. We detect the eclipse in both bandpasses with greater than 3σ significance for HAT-P-5b, WASP-7b, and WASP-127b. For HAT-P-38b we detect the eclipse at 3.6 μm but not at 4.5 μm, and for WASP-72b we detect the eclipse at 4.5 μm but not at 3.6 μm. This allows us to place relatively tight constraints on the eclipse depth in the bandpass with the non-detection, as the eclipse phase is effectively fixed in the joint fit by the detection in the other bandpass. We find that the best-fit eclipse phases for HAT-P-5b, HAT-P-38b, WASP-72b, and WASP-127b are all consistent with the expectation for a circular orbit to within 3σ. The posterior probability distribution for HAT-P-38b's eclipse phase is bimodal in the version of the fits where the per-point errors are left as free parameters, with one peak within 2σ of the predicted phase for a circular orbit and one peak corresponding to a secondary eclipse occurring ~30 minutes later than expected. The peak corresponding to a circular orbit is the taller of the two peaks in the initial fit, and when we inflate the per-point errors for the visits with significant correlated noise this secondary peak

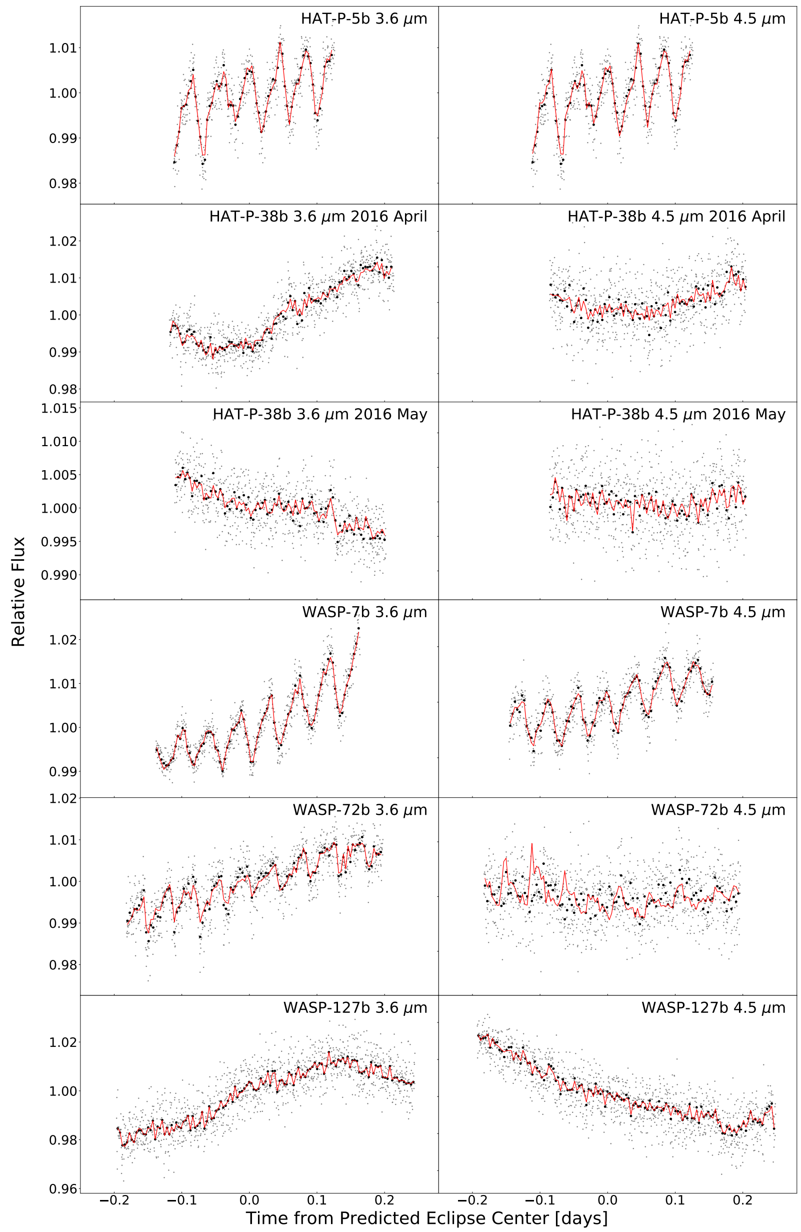

Figure 3.1: Raw *Spitzer* photometry for each visit of HAT-P-5b, HAT-P-38b, WASP-7b, WASP-72b, and WASP-127b. The normalized flux binned in 5 minute intervals is shown as black filled circles and the 30 second binned flux is shown as gray filled circled. The best-fit instrumental model is overplotted in red. Observations of HAT-P-38b are shown chronologically down each column.

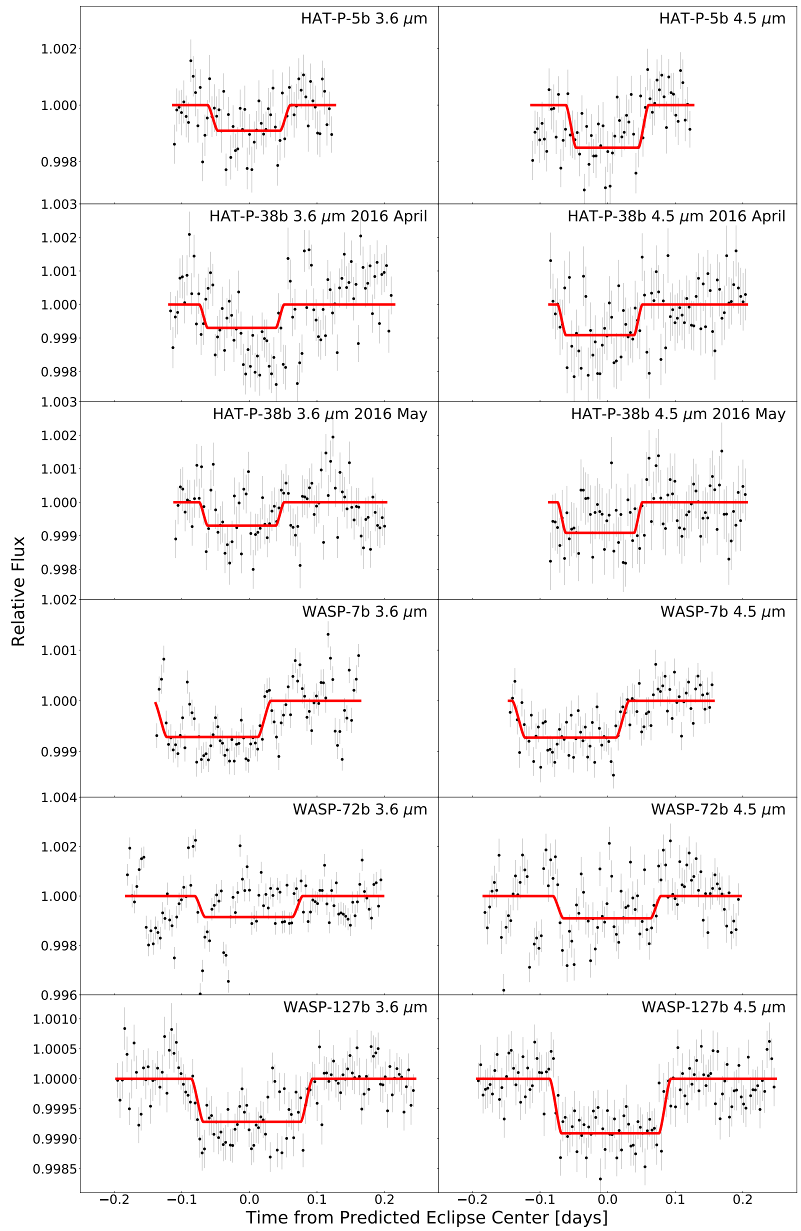

Figure 3.2: Normalized light curves for each visit of HAT-P-5b, HAT-P-38b, WASP-7b, WASP-72b, and WASP-127b from the simultaneous fits with instrumental effects removed. We show data binned in five-minute intervals (black filled circles) with error bars corresponding to the scatter in each bin divided by the square root of the number of points in each bin, and we overplot the best-fit secondary eclipse model in red. Observations of HAT-P-38b are shown chronologically down each column. The 2σ upper limits for the best-fit eclipse depths of the 4.5 μm visits of HAT-P-38b and the 3.6 μm visit of WASP-72b are shown.

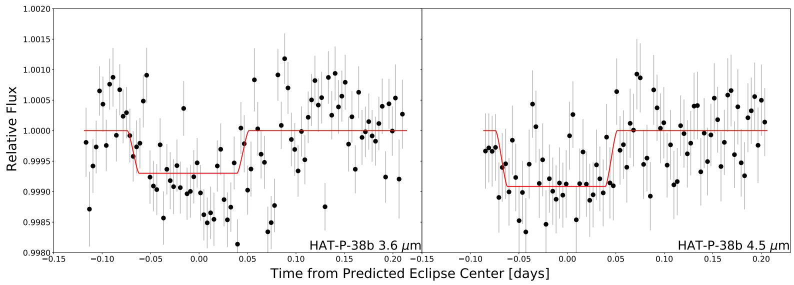

Figure 3.3: Band-averaged light curves for HAT-P-38b from the simultaneous fits with instrumental effects removed. We show data binned in five-minute intervals (black filled circles) with error bars corresponding to the scatter in each bin divided by the square root of the number of points in each bin, and overplot the best-fit eclipse model in each bandpass for comparison (red lines). The 2σ upper limit for the best-fit eclipse depth of the 4.5 μm data is shown.

is further suppressed, indicating that it is likely an artifact of the correlated noise. We therefore present the solution corresponding to the higher peak centered near a phase of 0.5 in Table 3.3.

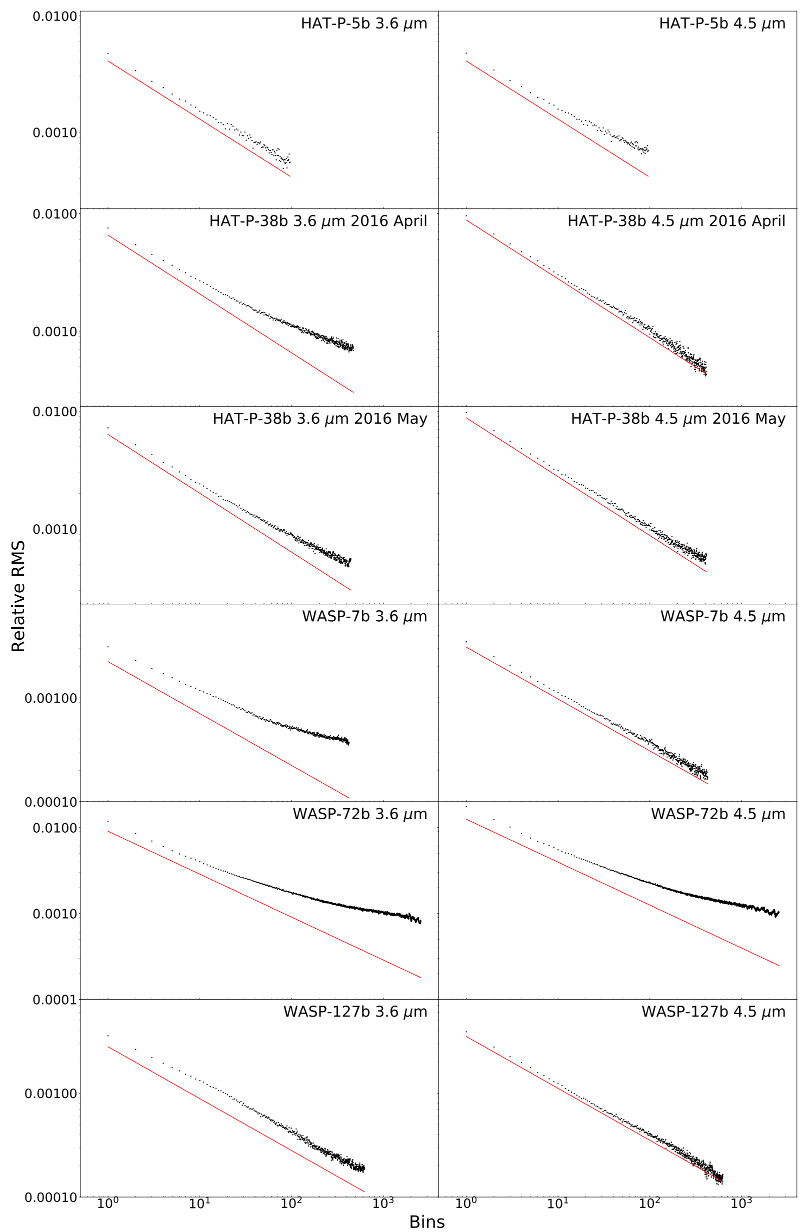

Figure 3.4: Standard deviation of the residuals as a function of bin size after removing the best-fit instrumental and astrophysical models. The solid lines show the predicted photon noise limit as a function of bin size, which follows a $1/\sqrt{N}$ scaling. Observations of HAT-P-38b are shown chronologically down each column.

Target	Band (μm)	Depth (ppm)	T_{Bright} (K)	Time Offset (days)[a]	Center of Eclipse (Phase)	$e\cos(\omega)$[b]
HAT-P-5b	3.6	908^{+202}_{-201}	1485^{+109}_{-118}	$-0.0006^{+0.0024}_{-0.0022}$	$0.4998^{+0.0009}_{-0.0008}$	$-0.0003^{+0.0014}_{-0.0012}$
	4.5	1508±266	1567^{+115}_{-121}			
HAT-P-38b	3.6	698±189[c]	1503^{+135}_{-150}	$-0.0113^{+0.0067}_{-0.0042}$[e]	$0.4976^{+0.0014}_{-0.0009}$	$-0.0038^{+0.0023}_{-0.0014}$
	4.5	<914[d]	<1425			
WASP-7b	3.6	714^{+191}_{-190}[c]	1583^{+147}_{-161}	$-0.0547^{+0.0035}_{-0.0029}$	$0.4890^{+0.0007}_{-0.0006}$	$-0.0173^{+0.0011}_{-0.0009}$
	4.5	725^{+109}_{-106}	1393^{+80}_{-82}			
WASP-72b	3.6	<852[c,d]	<2265	$-0.0009^{+0.0054}_{-0.0071}$	$0.4996^{+0.0024}_{-0.0032}$	$-0.0006^{+0.0038}_{-0.0050}$
	4.5	903^{+288}_{-294}[c]	2098^{+335}_{-364}			
WASP-127b	3.6	719±62	1454^{+42}_{-43}	$0.0038^{+0.0013}_{-0.0015}$	$0.5009^{+0.0003}_{-0.0004}$	$0.0014^{+0.0005}_{-0.0006}$
	4.5	910 ±69	1373^{+40}_{-41}			

Table 3.3: Best Fit Eclipse Parameters

[a]Time offset from predicted center of eclipse. We fit both channels with a common time of secondary eclipse.
[b] Computed using the approximation for a low eccentricity orbit.
[c] There is correlated noise present in the residuals of this fit (see Figure 3.4), and we therefore inflate the per-point errors in our fits (see §3.2 for more information).
[d]We report the 2σ upper limit for the eclipse depth.
[e]HAT-P-38b has a bimodal distribution for the time of secondary eclipse with one peak consistent with a circular orbit and a second smaller peak offset by ~30 minutes. We report the eclipse depths and time for the solution that is consistent with a circular orbit; see §3.3 for more details.

Our best fit solution for WASP-7b favors an eclipse that occurs $78.8^{+5.0}_{-4.2}$ minutes early, corresponding to an $e\cos(\omega)$ of $-0.0173^{+0.0011}_{-0.0009}$ where e is the orbital eccentricity and ω is the longitude of periastron. This time offset cannot be due to uncertainties in the planet's ephemeris, as the predicted time of secondary eclipse for a circular orbit has an uncertainty of less than 1 minute (Table 3.1). It is somewhat surprising that this planet would have an eccentric orbit, as the tidal circularization timescale for this system is predicted to be short ($\tau_{\rm circ}$<650 Myr estimated using Eq. 2 from Bodenheimer et al. (2001) and a tidal quality factor Q=10^6). This is significantly shorter than the system's 2.4 Gyr estimated age, and WASP-7b does not appear to have an exterior companion capable of maintaining a non-zero eccentricity in the face of ongoing circularization.

We can use the difference in the brightness temperatures between the two bandpasses to ascertain whether we detect changes in a planet's emission spectrum due to the presence of spectral features. For HAT-P-38b and WASP-72b, which have non-detections in one of the two bandpasses, we take a conservative 2σ upper limit as the brightness temperature in the bandpass with the non-detection. We find that all 5 planets have spectral shapes that are consistent with those of a blackbody at the 3σ level.

3.4 Discussion

We add three of our new secondary eclipse observations to the sample of all *Spitzer* secondary eclipse measurements from the literature. We include measurements of a subset of the 36 planets (27 of which were new) presented in Garhart et al. (2020) (those with detections in both bandpasses measured with a significance greater than 2.5σ; 31 planets). We also add 42 planets with published eclipses detected in both bandpasses at better than the 2.5σ level (see Table 3.4 for the full list of included planets). With more than twice the number of planets, we are able to further investigate trends in the spectral shapes of short period gas giant planets with measured *Spitzer* secondary eclipses. In order to be able to compare the thermal emission of these planets empirically, we calculate the brightness temperatures for each planet using the reported eclipse depths and planetary and stellar parameters from Southworth, 2011 (see Table 3.4 for more details).

Trends as a Function of Incident Flux

In the left-hand panel of Figure 3.5 we plot the 4.5 μm brightness temperature versus the 3.6 μm brightness temperature to see if the spectral slopes of these planets deviate

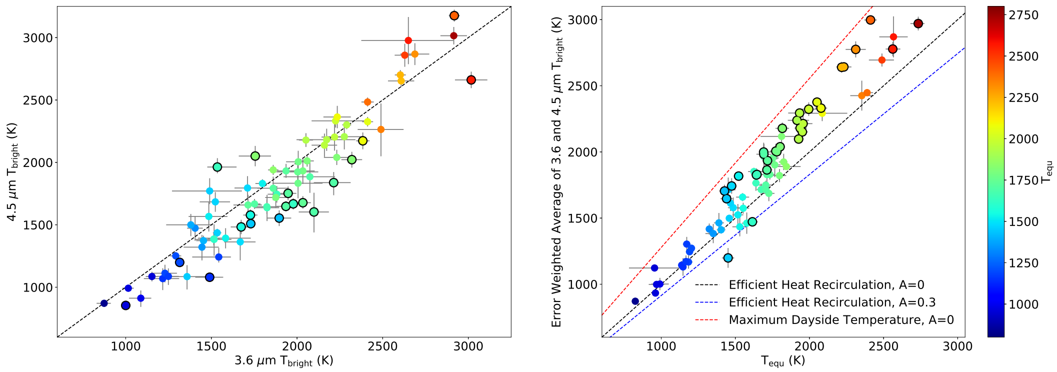

Figure 3.5: Left: Measured 4.5 μm brightness temperature versus 3.6 μm brightness temperature for the sample of all planets with published detections in both bands as well as three new planets from this study. Planets with blackbody-like spectra will lie close to the black dashed line, which corresponds to a 1:1 brightness temperature ratio in the two bands. We highlight points that deviate from this line by greater than 3σ (i.e., planets with non-blackbody emission) with black outlines. The color of the points indicates the predicted equilibrium temperature assuming efficient day-night circulation and zero albedo. Right: The error weighted average of the brightness temperatures measured in the 3.6 μm and 4.5 μm bandpasses versus the predicted equilibrium temperature. Planets that deviate by more than 3σ from the dashed black line (the expected brightness temperature for efficient heat recirculation and zero albedo) are outlined in black.

from that of a blackbody in a way that correlates with the incident flux. Garhart et al. (2020) found evidence for such a correlation in their study, but concluded that the trends they saw were not well-matched by commonly used model atmosphere grids. Baxter et al. (2020) used an expanded *Spitzer* data set to reproduce the trend found by Garhart et al. (2020) and concluded that models including temperature inversions were better able to capture the qualitative shifts in spectral shape as a function of temperature. As shown in the left-hand panel of Figure 3.5, we also find that the most highly irradiated planets tend to lie above the line (meaning their 4.5 μm brightness temperature is higher than their 3.6 μm brightness temperature). This is consistent with the predictions of models presented in Lothringer et al. (2018), who showed that planets in this temperature regime should have thermal inversions and additional opacity sources, such as H^{-}, that are not present in cooler atmospheres. At lower temperatures most of the planets in our sample tend to lie below this line, indicating that their brightness temperatures are relatively high at 3.6 μm and low at 4.5 μm. This is broadly consistent with the predictions of standard atmosphere models (Burrows et al., 1997, 2006; Fortney, 2005; Fortney et al., 2008), which suggest that the infrared spectra of these planets should be dominated by water and carbon monoxide absorption bands at these wavelengths. Because carbon monoxide overlaps significantly with the 4.5 μm *Spitzer* band, these models predict that planets in this temperature range should have brightness temperatures that are lower at 4.5 μm than at 3.6 μm (Garhart et al., 2020). This picture changes for planets with temperatures less than 1000 K (Wallack et al., 2019), where methane is predicted to be the dominant carbon-bearing molecule.

We can also use the difference between the band-averaged brightness temperatures and the expected equilibrium temperatures for each planet to investigate trends in circulation. As shown in the right-hand panel of Figure 3.5, the hottest planets in our sample appear to lie significantly above this line, indicating that they have less efficient day-night heat redistribution and low albedos. Indeed, none of these planets lie above the maximum dayside temperature line (calculated from Pass et al., 2019). As the incident flux decreases, planets move closer to the line corresponding to efficient day-night circulation, as predicted by general circulation models (Perez-Becker and Showman, 2013; Komacek and Showman, 2016). This is equivalent to the trend described in Schwartz and Cowan (2015), where the hottest planets appear to have less efficient redistribution of heat. We quantify the significance of this trend using a Monte Carlo simulation where we generate one realization of the datapoints by sampling from the probability distributions for each point assuming all errors are reasonably well-approximated by Gaussian distributions, fitting a line to the resulting realization and repeating this 10^6 times. We find that the slope of the best-fit line differs from the equilibrium temperature expectation by greater than 6σ and is qualitatively similar to the trend seen in Schwartz and Cowan (2015) despite the differences in the stellar models that we use. Schwartz and Cowan (2015) use a blackbody whereas we use a PHOENIX stellar model from Husser et al. (2013) integrated across the *Spitzer* bandpass when determining the stellar flux.

We note that a recent study by Baxter et al. (2020) was unable to reproduce this trend in their compilation of *Spitzer* secondary eclipse data when using a PHOENIX stellar model and integrating across the *Spitzer* bandpass (although when using a blackbody as in Schwartz and Cowan (2015), they were able to retrieve the trend). However, this study used the observed brightness temperature at 3.6 μm as opposed to the error weighted average of the brightness temperatures in the 3.6 and 4.5 μm bandpasses (C. Baxter, email communication). They argued that the presence of CO absorption in the 4.5 μm band makes the observed brightness temperature in this band more sensitive to potential changes in the dayside pressure-temperature profile than the 3.6 μm band. We evaluate the significance of the trend in our 3.6 μm data using the same Monte Carlo method as before. We find that using only the 3.6 μm data decreases the significance of the trend, but the best-fit line still deviates by ~3σ from the line defined by setting the brightness temperature equal to the equilibrium temperature. Although the slope of our best-fit line is consistent with the slope derived from Baxter et al. (2020) to 1σ, the error on our slope is a factor of ~2 less, resulting in an increased significance.[1] The difference in uncertainties between our best-fit slope and that found in Baxter et al. (2020) is likely due to their use of orthogonal distance regression to fit the line and their inclusion of data with large errors (we chose to exclude planets with less than 2.5σ detections in either the 3.6 or 4.5 μm bandpass).

Our study also obtains different dayside brightness temperatures than Baxter et al. (2020) for some individual planets. In some cases, this difference is due to the use of different values for the secondary eclipse depths (e.g. using Knutson et al. (2012) instead of Charbonneau et al. (2008), for the eclipse depth of HD 189733b). In other cases, it is due to the use of different values for the planet-star radius ratio and host star properties (effective temperature, metallicity, and gravity). In this study we use the most up-to-date values for the secondary eclipse depths, stellar parameters, and planetary parameters. Specifically, we source our stellar and planetary parameters from TEPCat, a database that seeks to compile the most recent and (where possible) homogeneously derived parameters for each exoplanetary system (Southworth, 2008, 2009, 2010, 2011, 2012). Unlike Baxter et al. (2020), we do not do an eccentricity cut on the planets that we include, but instead take the expected equilibrium temperature at the phase of secondary eclipse. We calculate our brightness temperatures using the same method as Baxter et al., 2020 (i.e. using a PHOENIX stellar model from Husser et al. (2013) and integrating across each *Spitzer* bandpass), and we obtain equivalent brightness temperatures when using the same input values.

We conclude that our data provide convincing evidence for a temperature-dependent change in recirculation efficiency. Although this trend might alternatively be interpreted as an increase in the dayside albedos of cooler planets, optical secondary eclipse measurements from *Kepler* suggest that most planets in this temperature

[1] We utilize the T_{equ} when calculating our slopes with effective temperature, but Baxter et al. (2020) utilize the $T_{irradiation}$. This choice is inconsequential when evaluating the statistical significance of the slopes because the difference is just a factor of $1/\sqrt{2}$, but we state this here for clarity.

regime have relatively low albedos (Heng & Demory, 2013). There are two planets (WASP-94Ab and WASP-131b) that lie more than 3σ below the zero albedo efficient circulation line, suggesting that they may have appreciably higher albedos than the other planets in this sample. Both WASP-94Ab and WASP-131b lie in the same temperature regime as Kepler-7b (Demory et al., 2011, 2013) and HATS-11b (Niraula et al., 2018), both of which have estimated geometric albedos of approximately 0.3 in the optical *Kepler* bandpass (versus < 0.1 for most gas giant planets in this temperature regime), likely due to the presence of high altitude silicate clouds (Demory et al., 2013). If WASP-94Ab and WASP-131b also have optical albedos close to 0.3, this would be sufficient to explain their lower than expected brightness temperatures.

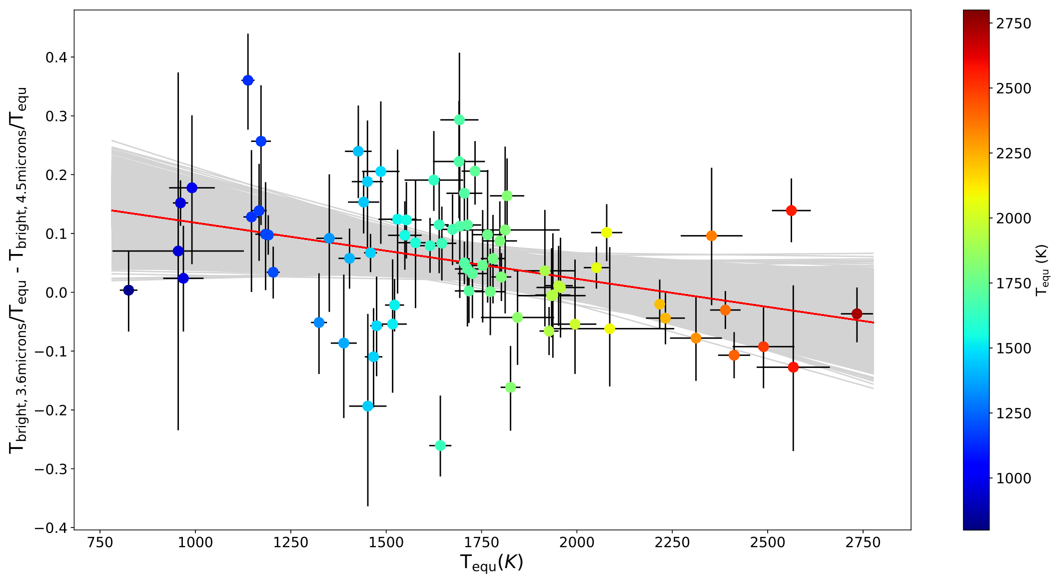

Figure 3.6: Change in 3.6−4.5 μm slope as a function of equilibrium temperature, where slopes have been normalized by the equilibrium temperature to keep the scale consistent across the full temperature range. The best fit linear trend is overplotted as a red line with a random sampling of the fit lines from the Monte Carlo shown as gray lines (see §3.4 for a description of the Monte Carlo simulations).

In order to better visualize the changes in the 3.6−4.5 μm spectral slope as a function of incident flux, we calculate the difference in brightness temperatures between the two bands and divide by the equilibrium temperature in order to keep the scale of this slope constant across the full temperature range. We plot the resulting scaled slope as a function of the predicted equilibrium temperature assuming zero albedo and efficient circulation in Figure 3.6. Unsurprisingly, the incident flux appears to be the primary driver of the observed spectral slope. We use the same Monte Carlo method as before to determine the significance of the trend in Figure 3.6. We find that negatively sloped lines are preferred at the 3.2σ level, suggesting that cooler planets tend to be brighter at 3.6 μm and dimmer at 4.5 μm than their more highly irradiated counterparts.

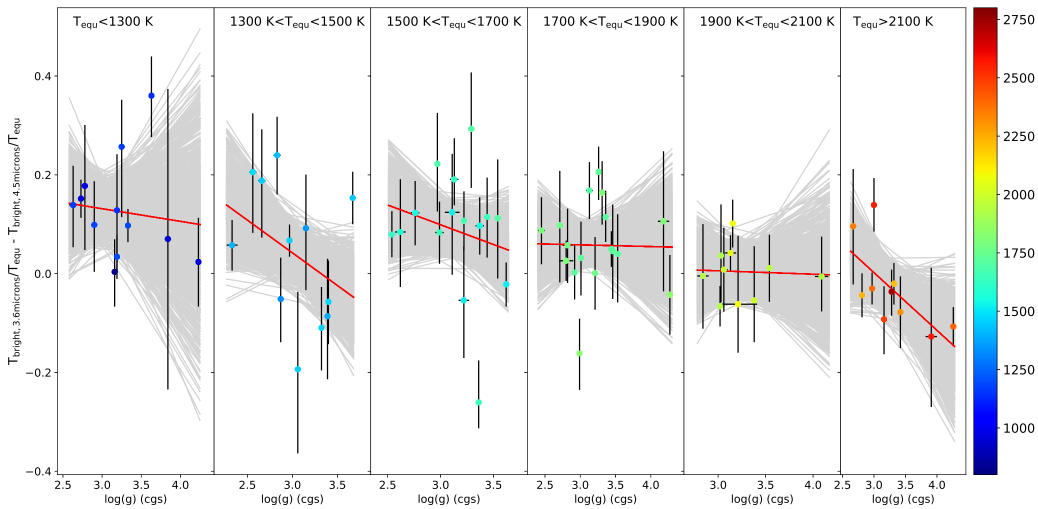

Figure 3.7: The difference in the two bandpasses, each normalized by equilibrium temperature, versus the planet gravity, divided into temperature bins. The red lines are the best fit from the Monte Carlo simulations and a random sampling of the fit lines from the Monte Carlo are shown as gray lines (see §3.4 for a description of the Monte Carlo simulations).

Trends as a Function of Surface Gravity and Host Star Metallicity

We next consider whether or not there are additional parameters beyond incident flux that correlate with the observed spectral slopes of these planets. We divide our planet sample into bins according to their predicted equilibrium temperatures and investigate trends in spectral shape within each temperature bin. We first consider whether or not surface gravity can explain some of the observed scatter in the spectral shapes of these planets (see Figure 3.7).

As before, we evaluate the significance of the trends in spectral slope as a function of surface gravity within each temperature bin using Monte Carlo simulations with 10^6 samples. We find that no temperature bin has a statistically significant slope (see Figure 3.7).

It is also possible that variations in atmospheric metallicity in this sample of planets might lead to variations in spectral slope. In Wallack et al. (2019), we found a tentative (~1.9σ) correlation between the measured spectral slope of planets with

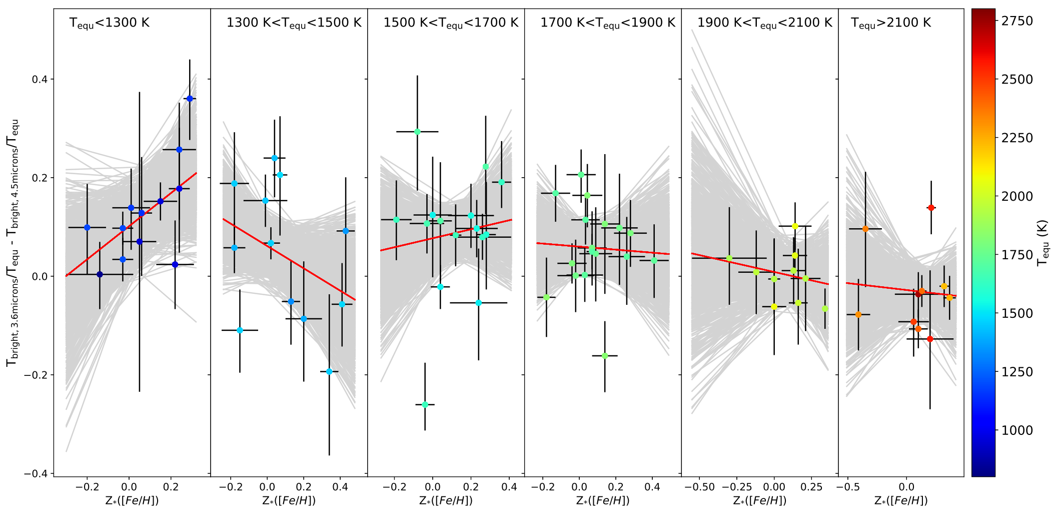

Figure 3.8: The difference in the two bandpasses, each normalized by equilibrium temperature, versus the stellar metallicity, divided into temperature bins. The red lines are the best fit from the Monte Carlo simulations and a random sampling of the fit lines from the Monte Carlo are shown as gray lines (see §3.4 for a description of the Monte Carlo simulations).

equilibrium temperatures less than ~1000 K and host stellar metallicity, which we use here as a proxy for planetary atmospheric metallicity. It is reasonable to assume that metal-rich stars should have correspondingly metal-rich disks, and therefore produce planets with correspondingly metal-enriched atmospheres. However, the range of metallicities spanned by the host stars in our planet sample only vary between −0.41 and +0.43, corresponding to a relatively small 6.9× change in bulk disk metallicity. In Wallack et al. (2019), we use a grid of atmosphere models to demonstrate that for cool ($\lesssim$ 1000 K) planets these *Spitzer* observations would only be sensitive to changes in atmospheric metallicity that are one to two orders of magnitude larger. Indeed, there are other indications that this picture is not as straightforward as one might hope. For example, Teske et al. (2019) found that there are no statistically significant correlations between host star abundances and bulk planetary metallicity for planets less than 1000 K, further complicating attempts to link stellar metallicity to the resulting planetary atmospheric and bulk metallicities.

We use our new expanded sample to search for trends in stellar metallicity within each temperature bin (Figure 3.8). Extending the equilibrium temperature bin of the cooler planets to 1300 K, we also recover the relationship between spectral slope and stellar metallicity hinted at in Wallack et al. (2019). In order to determine the significance of the trends in each panel in Figure 3.8 we again use a Monte

Carlo simulation where we sample from the probability distributions for each point. Interestingly, including these slightly warmer (1000 – 1300 K) planets in our lowest temperature bin does not greatly decrease the significance of the slope (which is still consistent with a flat line at the 1.8σ level), despite using different sources for the stellar metallicities and including warmer planets. Although we would not necessarily expect planets warmer than 1000 K to have the same metallicity-dependent shift in the ratio of methane to carbon monoxide and carbon dioxide that we see in cooler atmospheres, our previous study (as well as Drummond et al., 2018) demonstrated that for planets with C/O ratios less than 1, there is still a detectable change in the 3.6 – 4.5 μm spectral slope for these slightly warmer planets (see Wallack et al., 2019 Figure 6).

In contrast to this result, we find that negative slopes are preferred for planets in the 1300-1500 K bin, but our data are still consistent with a positive sloped or flat line at the 1.5σ level. It would not be surprising if the effects of metallicity on the spectral slope varied between temperature bins. As discussed above, changes in metallicity can alter the relative abundances of key molecules including methane, water, carbon monoxide, and carbon dioxide. For planets with high altitude cloud layers, changes in the metal content of the atmosphere might change the number density, vertical distribution, and average sizes of cloud particles (Morley et al., 2013). In general, we would expect increased cloud opacity at low pressures to suppress the amplitude of molecular features in the planet's dayside emission spectrum, making it look more like a blackbody (e.g., Morley et al., 2017) at near-infrared wavelengths. Indeed, planets with equilibrium temperatures in the 1300-1500 K temperature range are expected to host high altitude silicate cloud layers, and we might therefore expect this temperature bin to be more sensitive to metallicity-dependent changes in cloud properties at these wavelengths. At mid-infrared wavelengths on the other hand, we might expect to directly see emission peaks due to the presence of silicate clouds (Richardson et al., 2007).

3.5 Conclusions

We present new secondary eclipse depth measurements in the 3.6 and 4.5 μm *Spitzer* bands for HAT-P-5b, HAT-P-38b, WASP-7b, WASP-72b, and WASP-127b. We find that HAT-P-5b, HAT-P-38b, WASP-72b, and WASP-127b have secondary eclipse times consistent with the prediction for a circular orbit, but WASP-7b appears to have a modest orbital eccentricity ($e\cos(\omega)$ =-0.0173$^{+0.0011}_{-0.0009}$).

We combine these new detections with a sample of 73 planets with published 3.6 and 4.5 μm eclipse depths in an effort to better understand trends in the spectral shapes of these planets as a function of irradiation, surface gravity, and host star metallicity. We find that incident flux is the single most important factor for determining the atmospheric chemistry and circulation patterns of short-period gas giant planets. Although we would also expect surface gravity and host star metallicity to play a secondary role, we do not find any compelling evidence for correlations with these parameters in the current sample of *Spitzer* eclipses. Most planets in our sample with the same incident flux level have broadly similar spectral shapes, but our study also reveals a subset of planets that appear as outliers in these plots. For example, WASP-94Ab and WASP-131b appear to be cooler than expected and may have high reflective cloud layers in their dayside atmospheres. Such planets are particularly promising targets for the *James Webb Space Telescope* (JWST), which is currently scheduled for launch in 2021. The increased aperture size and wavelength coverage of *JWST* will allow us to obtain invaluable new insights into the atmospheric compositions of gas giant planets.

3.6 Appendix

We show the full list of planets (both from the literature and from this study) with detected eclipses (at the 2.5σ level or better) in both the 3.6 μm and 4.5 μm *Spitzer* bandpasses in Table 3.4. Planets shown in bold have new eclipses detected herein.

Planet	T_{equ} (K)	3.6 T_{bright} (K) [a]	4.5 T_{bright} (K) [a]	log (gravity) (cgs)	$[\mathrm{Fe/H}]_*$	refs
CoRoT-1b	1916^{+81}_{-62}	2276^{+106}_{-109}	2206^{+101}_{-102}	3.03±0.03	-0.30±0.25	1,2
CoRoT-2b	1522±25	1798^{+40}_{-41}	1831^{+34}_{-35}	3.62±0.02	0.04±0.05	1,2
HAT-P-1b	1324±21	1405^{+45}_{-47}	1473^{+96}_{-101}	2.87±0.01	0.13±0.05	1,3
HAT-P-2b[b]	1812±143	2232^{+74}_{-75}	2040±61	4.18±0.08	0.14±0.08	1,4
HAT-P-3b	1172±26	1543^{+71}_{-155}	1242^{+74}_{-44}	3.25±0.03	0.24±0.08	1,5
HAT-P-4b	1691^{+68}_{-32}	2214^{+99}_{-116}	1838^{+85}_{-101}	$2.97^{+0.02}_{-0.04}$	0.277±0.007	1,5
HAT-P-5b	1517±37	1485^{+109}_{-118}	1567^{+115}_{-121}	3.22±0.05	0.24±0.15	1,6
HAT-P-6b	1705±47	1935^{+55}_{-56}	1648±41	3.13±0.05	-0.13±0.08	1,7
HAT-P-7b	2217±13	2608^{+76}_{-77}	2653±49	3.317±0.007	0.32±0.04	1,8
HAT-P-8b	1733±35	2034^{+47}_{-68}	1677^{+53}_{-48}	3.26±0.02	0.01±0.08	1,7
HAT-P-13b	1726±38	1714^{+81}_{-85}	1659^{+82}_{-85}	3.01±0.02	0.41±0.08	1,9
HAT-P-19b	991^{+60}_{-58}	1088^{+61}_{-69}	912^{+62}_{-70}	2.78±0.03	0.24±0.05	1,10
HAT-P-20b[b]	969±53	1015^{+32}_{-35}	992±21	4.23±0.02	0.22±0.09	1,11
HAT-P-23b	1952±37	2160^{+74}_{-75}	2138^{+93}_{-94}	3.54±0.03	0.13±0.08	1,12
HAT-P-30b	1646±38	1882^{+52}_{-53}	1745^{+66}_{-67}	2.99±0.04	0.12±0.03	1,9
HAT-P-32b	1802±26	2059^{+39}_{-40}	2012±46	2.80±0.10	-0.04±0.08	1,13
HAT-P-33b	1780±32	2034^{+69}_{-71}	1932^{+101}_{-104}	2.82±0.06	0.07±0.08	1,9
HAT-P-40b	1766^{+39}_{-44}	2006^{+143}_{-150}	1833^{+117}_{-121}	2.71±0.03	0.22±0.10	1,9
HAT-P-41b	1937^{+46}_{-38}	2173^{+168}_{-176}	2182^{+88}_{-90}	2.84±0.06	0.21±0.10	1,9
HD149026b	1625^{+77}_{-39}	1978±37	1668^{+44}_{-45}	$3.13^{+0.03}_{-0.04}$	0.36±0.05	1,14
HD189733b	1191±25	1315±11	1199±9	3.33±0.02	-0.03±0.05	1,15
HD209458b[c]	1459±17	1534^{+24}_{-25}	1436^{+32}_{-33}	2.968±0.004	0.02±0.05	1,16
KELT-2Ab	1713^{+36}_{-29}	1948±48	1752^{+55}_{-56}	3.36±0.04	0.034±0.078	1,9
KELT-3b	1817^{+45}_{-46}	2320^{+60}_{-61}	2022^{+63}_{-64}	3.31±0.04	$0.044^{+0.080}_{-0.082}$	1,9
KELT-7b	2051±33	2412±32	2326±38	3.13±0.06	$0.139^{+0.075}_{-0.081}$	1,9

Planet	T_{equ} (K)	3.6 T_{bright} (K) [a]	4.5 T_{bright} (K) [a]	log (gravity) (cgs)	[Fe/H]$_*$	refs
Kepler-5b	1693^{+35}_{-29}	2075^{+147}_{-154}	1885^{+125}_{-129}	3.54±0.02	0.04±0.06	1,17
Kepler-6b	1452^{+49}_{-26}	1490^{+188}_{-220}	1771^{+102}_{-105}	$3.06^{+0.01}_{-0.02}$	0.34±0.05	1,17
Kepler-12b	1486^{+49}_{-36}	1668^{+89}_{-94}	1363^{+135}_{-148}	2.56±0.04	0.07±0.04	1,18
Kepler-13Ab	2567±96	2650^{+265}_{-275}	2977^{+188}_{-190}	3.91±0.09	0.20±0.20	1,19
Kepler-17b	1713^{+33}_{-67}	1861^{+89}_{-93}	1793^{+93}_{-96}	3.53±0.01	0.26±0.10	1,20
Qatar-1b	1389^{+34}_{-33}	1380^{+127}_{-144}	1500^{+87}_{-91}	3.39±0.01	0.20±0.10	1,9
TrES-1b	1147±21	1216^{+96}_{-110}	1069^{+83}_{-92}	3.19±0.03	0.06±0.05	1,21
TrES-2b	1467±23	1523^{+86}_{-91}	1684^{+78}_{-80}	3.323±0.006	-0.15±0.10	1,22
TrES-3b	1639±25	1825^{+71}_{-73}	1637^{+103}_{-107}	3.44±0.02	-0.19±0.08	1,23
TrES-4b	1798±45	1876^{+61}_{-62}	1719^{+83}_{-85}	2.45±0.05	0.28±0.09	1,24
WASP-1b	1826^{+26}_{-32}	1756^{+92}_{-96}	2051^{+81}_{-82}	$2.99^{+0.03}_{-0.04}$	0.14±0.07	1,25
WASP-3b	1995^{+56}_{-48}	2225^{+192}_{-140}	2333±54	3.38±0.03	0.161±0.063	1,26
WASP-4b	1674±29	1824^{+70}_{-72}	1645^{+57}_{-58}	3.221±0.009	-0.03±0.09	1,27
WASP-5b	1753±40	2004^{+120}_{-125}	1924^{+94}_{-96}	3.46±0.04	0.09±0.09	1,28
WASP-6b	1184±27	1229^{+70}_{-77}	1112^{+68}_{-73}	2.90±0.02	-0.20±0.09	1,10
WASP-7b	1530±50	1583^{+147}_{-161}	1393^{+80}_{-82}	3.11±0.07	0.00±0.10	1,6
WASP-8b[b]	1138±17	1490^{+79}_{-84}	1080^{+34}_{-36}	3.63±0.02	0.29±0.03	1,29
WASP-10b[b]	955^{+172}_{-173}	1153^{+34}_{-36}	1086^{+38}_{-39}	3.84±0.04	0.05±0.08	1,10
WASP-12b	2562^{+51}_{-48}	3017^{+94}_{-95}	2661±66	3.00±0.01	0.21±0.04	1,9
WASP-14b[b,c]	1934^{+89}_{-77}	2290±26	2301±35	$4.09^{+0.08}_{-0.07}$	0.00±0.04	1,9
WASP-18b	2412±42	2918±32	3176±48	4.26±0.02	0.10±0.08	1,9
WASP-19b[c]	2078±41	2384±39	2173^{+67}_{-68}	3.153±0.005	0.14±0.11	1,9
WASP-24b	1773±40	2007^{+70}_{-71}	2005^{+88}_{-90}	3.21±0.03	-0.02±0.10	1,30
WASP-33b	2734^{+42}_{-53}	2915^{+77}_{-78}	3015±70	3.28±0.04	0.10±0.20	1,14
WASP-39b	1167±20	1249^{+61}_{-66}	1087^{+64}_{-69}	2.63±0.05	0.01±0.09	1,10

Planet	$T_{\rm equ}$ (K)	3.6 $T_{\rm bright}$ (K) [a]	4.5 $T_{\rm bright}$ (K) [a]	log (gravity) (cgs)	[Fe/H]$_*$	refs
WASP-43b	1441±41	1730^{+24}_{-25}	1509^{+31}_{-32}	3.67±0.01	-0.01±0.12	1,9
WASP-48b	1957±63	2219^{+75}_{-76}	2203^{+108}_{-109}	3.06±0.04	-0.12±0.12	1,12
WASP-62b	1427±35	1896^{+70}_{-72}	1554^{+62}_{-64}	2.83±0.04	0.04±0.06	1,9
WASP-63b	1577^{+46}_{-32}	1516^{+101}_{-109}	1383^{+121}_{-131}	2.62±0.05	0.28±0.05	1,9
WASP-64b	1692±50	2099^{+87}_{-89}	1603^{+154}_{-164}	3.29±0.03	-0.08±0.11	1,9
WASP-69b	961±20	1000±17	854^{+18}_{-19}	2.73±0.04	0.15±0.08	1,31
WASP-74b	1927±25	2052±41	2179±55	3.02±0.01	0.34±0.02	1,9
WASP-76b	2232±51	2603±32	2701±39	2.81±0.03	0.366±0.053	1,9
WASP-77Ab	1705±22	1752±35	1667±40	3.441±0.008	0.07±0.03	1,9
WASP-78b	2353^{+81}_{-78}	2490^{+132}_{-136}	2264^{+208}_{-215}	2.67±0.04	-0.35±0.14	1,9
WASP-79b	1717^{+37}_{-34}	1936^{+51}_{-52}	1932±56	2.92±0.04	0.03±0.10	1,9
WASP-80b	825±23	874^{+39}_{-44}	871±16	3.16±0.01	-0.14±0.16	1,32
WASP-87b	2312±68	2688^{+84}_{-85}	2868^{+87}_{-88}	3.42±0.03	-0.41±0.10	1,9
WASP-94Ab	1615^{+36}_{-32}	1514^{+35}_{-36}	1386^{+50}_{-51}	2.54±0.03	0.26±0.15	1,9
WASP-97b	1549±44	1728^{+41}_{-42}	1578^{+44}_{-45}	3.37±0.04	0.23±0.11	1,9
WASP-100b	2086^{+169}_{-106}	2235^{+79}_{-81}	2364^{+89}_{-90}	$3.20^{+0.20}_{-0.10}$	0.00±0.08	1,9
WASP-101b	1553±40	1674^{+59}_{-61}	1483^{+57}_{-58}	2.76±0.04	0.20±0.12	1,9
WASP-103b[c]	2489^{+81}_{-88}	2629^{+58}_{-59}	2859^{+92}_{-93}	$3.16^{+0.02}_{-0.03}$	0.06±0.13	1,9
WASP-104b	1475±17	1711^{+73}_{-76}	1795^{+95}_{-97}	3.40±0.01	0.410±0.057	1,9
WASP-121b	2389±40	2412±36	2484±36	2.97±0.02	0.13±0.04	1,9
WASP-127b	1404±29	1454^{+42}_{-43}	1373^{+40}_{-41}	2.33±0.06	-0.18±0.06	1,6
WASP-131b	1451±41	1358^{+109}_{-122}	1085^{+92}_{-103}	2.66±0.04	-0.18±0.08	1,9
XO-1b	1204±17	1292^{+32}_{-33}	1251^{+33}_{-34}	3.19±0.01	-0.03±0.05	1,33
XO-2b	1351^{+34}_{-53}	1445^{+98}_{-107}	1321^{+98}_{-106}	3.15±0.03	0.43±0.05	1,34

Planet	T_{equ} (K)	3.6 T_{bright} (K) [a]	4.5 T_{bright} (K) [a]	log (gravity) (cgs)	$[Fe/H]_*$	refs
XO-3b[b]	1844±96	1861±30	1940±40	4.27±0.03	-0.18±0.05	1,35
XO-4b	1642^{+29}_{-25}	1535^{+112}_{-59}	1963^{+71}_{-50}	3.36±0.03	-0.04±0.05	1,7

Table 3.4: Brightness Temperatures and System Parameters

[a]Planetary system parameter values used in computing brightness temperatures from Southworth (2011).
[b]For this highly eccentric planet (Bonomo et al., 2017), we report the temperature at the planet's separation at secondary eclipse.
[c]We calculate the brightness temperature for this planet using the error-weighted average of the reported eclipses.
(1) Southworth (2011), (2) Deming et al. (2011), (3) Todorov et al. (2010), (4) Lewis et al. (2013), (5) Todorov et al. (2013), (6) this work, (7) Todorov et al. (2012), (8) Wong et al. (2016), (9) Garhart et al. (2020), (10) Kammer et al. (2015), (11) Deming et al. (2015), (12) O'Rourke et al. (2014), (13) Zhao et al. (2014), (14) S. Zhang et al. (2018), (15) Knutson et al. (2012), (16) Evans et al. (2015), (17) Désert, Charbonneau, Fortney, et al. (2011), (18) Fortney et al. (2011), (19) Shporer et al. (2014), (20) Désert, Charbonneau, Demory, et al. (2011), (21) Cubillos et al. (2014), (22) O'Donovan et al. (2010), (23) Fressin et al. (2010), (24) Knutson et al. (2009), (25) Wheatley et al. (2010), (26) Rostron et al. (2014), (27) Beerer et al. (2011), (28) Baskin et al. (2013), (29) Cubillos et al. (2013), (30) Smith et al. (2012), (31) Wallack et al. (2019), (32) Triaud et al. (2015), (33) Machalek et al. (2008), (34) Machalek et al. (2009), (35) Machalek et al. (2010)

Chapter 4

SURVEY OF PROTOPLANETARY DISKS USING THE KECK/NIRC2 VORTEX CORONAGRAPH

4.1 Introduction

Gaps, cavities, and spiral features seen in protoplanetary disks are thought to be the signposts of planet formation. Millimeter-sized dust grains are expected to rapidly drift inwards, resulting in the depletion of large dust grains at large radii (Weidenschilling, 1977). However, when imaged by facilities such as the Atacama Large Millimeter/submillimeter Array (ALMA), structures in the large dust grains are evident out to hundreds of au in many protoplanetary disks (e.g., Andrews et al., 2018; Long et al., 2018). In order to keep these dust grains at such large orbital separations, there must be mechanisms in effect that trap dust grains at large distances and produce the spiral, concentric ring, and gap substructures that seem to be prevalent among protoplanetary disks imaged with ALMA. A number of different mechanisms have been suggested to explain the protoplanetary disk dust distributions, including magnetorotational instabilities, dead zones, and condensation fronts (e.g., Isella et al., 2016; S.-F. Liu et al., 2018; Ohashi and Kataoka, 2019). However, one of the most favored explanations for the substructures in the observed millimeter dust in these disks is that they are caused by forming planets interacting with the natal disk structure. Forming giant planets can cause pressure bumps outside of their orbits and trap large dust grains into rings while less massive planets generally open gaps in the dust in the disks with no significant changes to the local gas (Paardekooper & Mellema, 2006; Zhu et al., 2014). The presence of protoplanets associated with disk substructures has also been inferred by measuring deviations from Keplerian velocity in the gas velocity field (Pinte et al., 2019; Teague et al., 2018).

Determining the masses of the planets that are carving out the gaps in the gas and dust of the disk is complicated by uncertainties on the bulk disk parameters, which can lead to large degeneracies in the masses derived from the geometry of millimeter dust cavities and gaps. For example, assuming different values for the disk viscosity, which is a largely observationally unconstrained parameter, can lead to differences in the calculated masses of planets on the order of a factor of >4 (S. Zhang et al., 2018). One way to more directly estimate the masses of planets carving these gaps is to directly detect the young planets' thermal emission.

Direct imaging is uniquely able among planet detection and characterization methods to probe the locations of the proposed wide-separation planets carving out the gaps in these young systems. Thus, direct imaging is capable of detecting planets in the act of forming, allowing us to place observational constraints both on the masses required to carve out millimeter gaps and also probe formation locations and accretion timescales. Leveraging the fact that the blackbody expectation of a cool planet would dictate more advantageous contrast in the L'-band (3.8 μm) over other wavelengths, there have been multiple direct imaging surveys of protoplanetary disks at L' (e.g., Stone et al., 2018; Launhardt et al., 2020) and more broadly in the infrared (Asensio-Torres et al., 2021). Moreover, observing in the L'-band allows for a compromise between more favorable planet-to-star contrast expectations and increased background noise at longer infrared wavelengths such as the M-band.

Conducting a survey at L' allows for more advantageous planet-to-star flux ratios over millimeter wavelengths making these infrared surveys the most sensitive to directly detecting the planets inferred by the millimeter data. Additionally, the infrared wavelength observations also provide information on the micron-sized dust distribution as inferred from scattered light. This means that this technique allows for both possible direct detection of planets while also providing a better understanding of the distribution of small dust grains, allowing for direct observations of planets interacting with their natal disks and actively accreting their atmospheres (e.g., the PDS 70 system; Benisty et al., 2018, Keppler et al., 2018).

To this end, we present a survey using the Keck/NIRC2 vortex coronagraph (Mawet et al., 2016, Serabyn et al., 2017) of protoplanetary disks previously observed at other wavelengths that show substructures and/or cavities. Utilizing the vortex coronagraph allows for high sensitivity to faint sources at small angular separations (down to 0."1), ideal for probing the cavities shown in the millimeter/sub-millimeter dust close to the host star.

In Section 4.2, we discuss the strategy for our observations. In Section 4.3, we present detection limits of all our targets using our derived contrast curves and in Section 4.4, we put these contrast curves into the broader context of the detection possibility of long-period giant planets.

4.2 Observations

Target Selection

All targets were selected for using the criteria that they (1) have published images in the millimeter/sub-millimeter or a published spectral energy distribution (SED); (2) show evidence in the ALMA data or SED for a gap and/or cavity that could have been formed due to interactions between the millimeter-sized dust and a forming protoplanet; (3) are nearby (preferably within ~300 pc); (4) are bright enough for a high-quality adaptive optics (AO) correction; and (5) are estimated to be young (<30Myr). Our targets were originally taken from papers on individual disks observed with ALMA and disks that showed evidence for gaps from their SEDs. However, following the publication of the ALMA survey of the Taurus star-forming region (Long et al., 2018), and the DSHARP survey (Andrews et al., 2018), we mostly selected targets that were from one of these two surveys because their high-resolution observations allowed for more precise estimates of gap locations in the disks and expected masses of planets that could be opening those gaps (see Table 4.1 for more information).

Observing Strategy

Observations started in observing semester 2015B and continued over the next 10 observing semesters (see Table 4.2 for more details). We observed a total of 43 protoplanetary disk targets, with some observed multiple times for follow-up observations or to account for non-ideal observing conditions.

Observations were done using two different wavefront sensors (WFSs). The observations done prior to 2019B (2019-08-01) were done primarily with the visible Shack-Hartmann WFS on the Keck II telescope. The AO correction for this WFS is operated in R-band, meaning that early in our survey we were limited to targets with bright R-band magnitudes. For the post-2019B targets in our survey, we used the recently facilitized Keck II infrared pyramid WFS, which performs wavefront sensing in H-band, meaning that we could observe redder targets with a better AO correction (Bond et al., 2020).

Our targets were observed using the Keck/NIRC2 vortex coronagraph using `QACITS`, a real-time point spread function (PSF) centering algorithm that keeps the target star well centered on the vortex mask and stabilized during the entirety of the observing sequence (Huby et al., 2017). The vortex coronagraph allows for high-contrast imaging at small angular separations (down to ~100 mas) in K, L', and M bands (see Xuan et al., 2018 for a performance characterization of the vortex coronagraph).

A combination of using the vortex coronagraph and multiple observing techniques (angular differential imaging, [ADI] and reference star differential imaging [RDI]) allows for the most advantageous scenario for the detection of exoplanets close in to their host stars. ADI and RDI are largely complementary observing strategies enabling detection of point sources close in to the central star and characterization of any extended structure in the image.

The ADI strategy (M. C. Liu, 2004; Marois et al., 2006) takes advantage of the field rotation of the sky as seen by alt-azimuth telescopes, causing any circumstellar sources (planet or disk) to rotate with time on the detector and any non-astrophysical signals due to optical effects (such as diffraction and high-order wavefront errors) to stay mostly static in time. After subtracting most quasi-static speckles using the sequence of frames, the astrophysical sources should remain, allowing for possible detection of disk structures or point sources that would otherwise be embedded in the diffracted starlight from the host star. ADI is most sensitive to point sources at regions a few diffracted beamwidths (λ/D, where λ is the wavelength and D is the telescope diameter) from the star.

The RDI observing strategy uses the point spread function of similar stars (in terms of stellar type and airmass at time of observation) to characterize and remove any remaining stellar contribution (which was not suppressed by the coronagraph). See Ruane et al., 2019 for a full discussion of the benefits of utilizing RDI in the context of observing with the vortex coronagraph on Keck/NIRC2. RDI is most sensitive to areas at smaller angular separations ($\lesssim$0."3) in the frame, making it beneficial to use both observing strategies (Ruane et al., 2017). We utilize two methods of RDI, targeted RDI and single-night RDI. While we observed all of our targets in the L'-band at least using ADI, for a subset of the targets we also obtained specifically targeted reference stars for RDI. These targeted RDI observations consisted of observing our science target symmetrically around transit (minimum airmass) and then observing a specifically chosen reference star (to be as similar in magnitude and airmass as possible) for the same amount of time also centered at its transit. We chose reference stars to best represent the PSFs of our science targets but without known planets, stellar companions, or disk material. When possible, we observed each reference star centered on its time of transit for enough time so that the total number of frames and integration time were similar to those of the science target.

In addition to the use of specifically targeted reference stars, we also utilized RDI within an observing night when multiple targets were observed at L' within a night. Despite the stellar PSFs not being manually matched to the PSFs of the science targets, in the absence of specifically selected reference stars, this form of single night RDI gives us a preliminary analysis that often achieves better contrast at smaller separations ($\lesssim$0."3) than ADI. A more refined RDI analysis with optimized reference frames taken from the library of L' vortex observations might allow for deeper achieved contrasts.

Regardless of observing strategy, we corrected the frames for bad pixels, flat-fielded them, subtracted the sky background, registered them, and applied principal component analysis (PCA). PCA was utilized in order to estimate the stellar contribution in the images via the Vortex Image Processing (`VIP`) package[1] (Gomez Gonzalez et al., 2017) and the `pyKLIP` package[2] (J. J. Wang et al., 2015).

4.3 Results

Survey Sensitivity Estimates

We first compute the 5σ contrast curves for each of our targets using `VIP` (Figure 4.1). These contrast curves are computed in the same manner as described in Xuan et al. (2018). In brief, for each observation, we determine the optimal contrast curve among our different combinations of inner and outer mask sizes, reduction method (ADI and RDI), and numbers of principal components by determining the optimal contrast in any of the different combinations of those parameters in steps of 1-pixel. We do this by first generating a 5σ contrast curve for each combination of mask and frame size, number of principal components, and reduction method using `VIP` (Gomez Gonzalez et al., 2017) and accounting for the effects of small sample statistics as described in Mawet et al. (2014). `VIP` utilizes the fake companion method of determining the throughput (Gomez Gonzalez et al., 2017). This method involves injection and recovery of a series of fake companions into the images in order to determine the contrast limits. We compare the contrast in each 1-pixel step obtained for all combinations of inner and outer mask size, reduction method, and number of principal components and take the minimum contrast achieved. We repeat this process for each 1-pixel step until we have an optimal contrast curve across all radial separations, which in reality represents multiple post-processing frame configurations. In the case that we have multiple datasets of the same object, we only consider the contrast curve corresponding to the more sensitive contrast

[1] Available under open-source license at https://github.com/vortex-exoplanet/VIP.
[2] Available under open-source license at https://bitbucket.org/pyKLIP/pyklip.

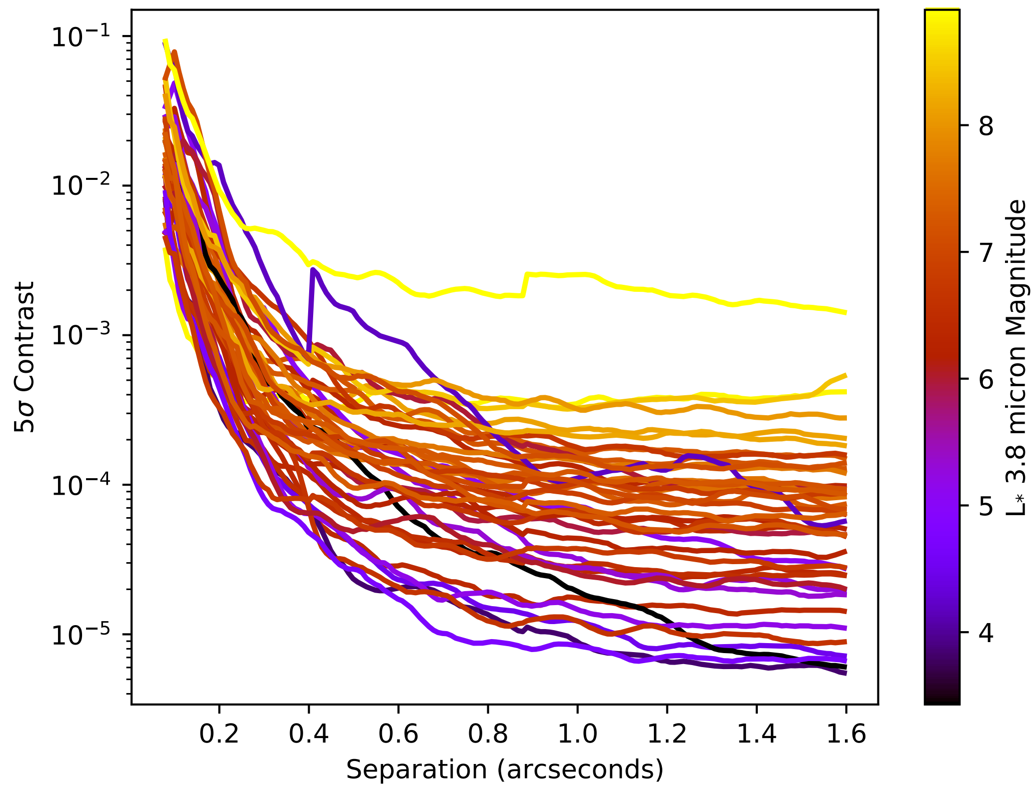

Figure 4.1: Optimal contrast curves for our sample of protoplanetary disks colored by L′ magnitude. Each line is the most optimal 5σ contrast for a different disk.

in subsequent analyses (and present the optimal contrast curve for each system in Figure 4.1).

For our study, we focus primarily on our `VIP` reductions, but we also compute the corresponding contrast curves using the `pyKLIP` package. For the `pyKLIP` reductions, after image preprocessing and registration, each image is high-pass filtered using a Gaussian kernel with a width equal to twice the full width at half maximum (FWHM) of the off-axis (when the star is not on the vortex coronagraph) point spread function. We then run `pyKLIP` in ADI mode with the following parameters: an exclusion parameter of half the FWHM, 30 Karhunen–Loève modes, an inner working angle equal to twice the FWHM, an annuli width equal to about half the FWHM, and a number of reference frames limited to the 200 most correlated images for each science frame (see Ruffio et al., 2017, for a more detailed description of the algorithm). After speckle subtraction, the images of a dataset are coadded and a Gaussian matched filter is used as described in Ruffio et al. (2017). The width of the Gaussian kernel is equal to the PSF FWHM. The algorithm throughput is

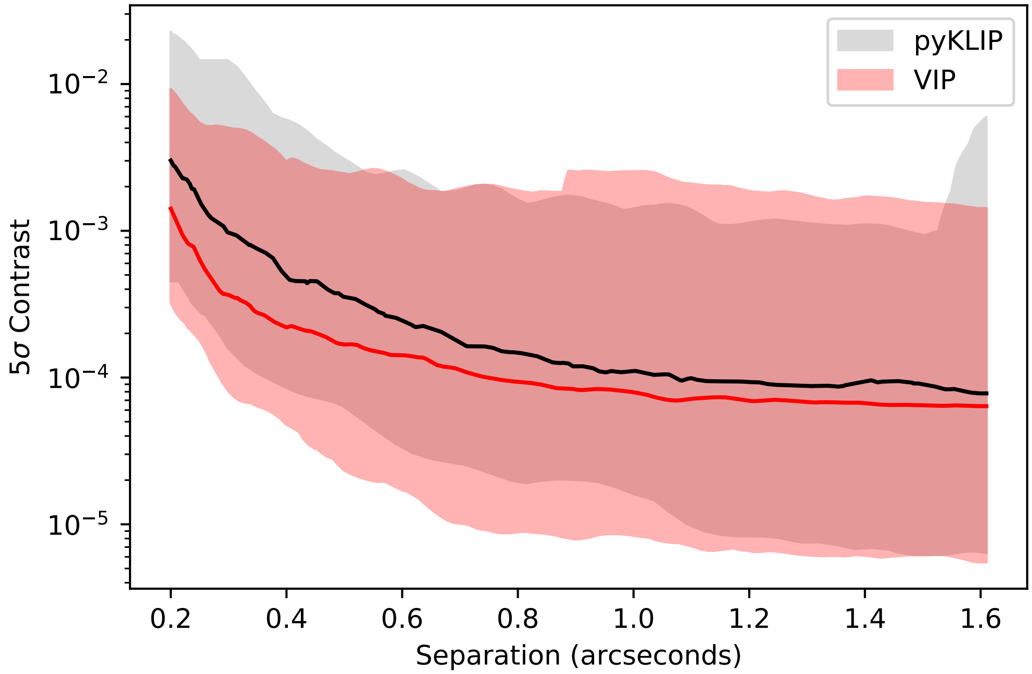

Figure 4.2: A comparison of the contrasts achieved using the `pyKLIP` and `VIP` reductions. The solid lines are the median contrasts of all of the contrast curves and the shaded regions represent the range of contrasts. We use ADI for the `pyKLIP` reductions and a combination of ADI and RDI for the `VIP` reductions.

calculated from the injection and recovery of 160 simulated planets. Despite high-pass filtering the `pyKLIP` reductions and not high-pass filtering the `VIP` reductions, the contrasts that are achieved by the two reductions are comparable (Figure 4.2). We utilize both sets of reductions in order to thoroughly vet detected point sources. For `pyKLIP`, we primarily focus on the aforementioned ADI reductions. However, with `VIP`, we utilize a combination of ADI and RDI, because RDI outperformed the ADI at small separations using `VIP`, which likely accounts for the better contrast limits for the `VIP` reductions at small separations.

Point Source Detection

In order to determine if we detect any significant point sources in our images, we generate a signal-to-noise ratio (SNR) map for each different combination of frame sizes, number of principal components, and reduction methods that were determined to be the optimal combination at each 1-pixel step in separation utilizing the `VIP` package (Gomez Gonzalez et al., 2017). We then create an optimal SNR map representative of our composite optimal contrast curve by taking the SNR map corresponding to the frame size, number of principal components, and reduction method that best optimized the contrast in each 1-pixel step and making a composite SNR map consisting of each of the respective 1-pixel annuli. Since we are interested in the region of the disks where structure is seen in the millimeter, we focus on the region between 0."15 and 1."6.

Direct imaging data is plagued by stellar residuals due to imperfect removal of the stellar PSFs. Some of these residual speckles can mimic the appearance of point sources in our data. Without the use of multi-wavelength data on these speckles in order to ascertain whether they have spectra similar to that of the host star, these speckles can be mistaken for astrophysical point sources. However, many of these speckles are post-processing specific and different reduction pipelines can generate artifacts in different locations and at different SNRs.

We determine if there are any physical point sources detected in any of our observations by first generating a list of all point sources outside of our central 0."15 mask and inside 1."6 with SNR $>$ 5, utilizing the SNR maps generated from the `VIP` reductions (the locations of which are shown in Figure 4.11). We achieve slightly better contrast limits using the `VIP` reductions (Figure 4.2), so we search for point sources in that set of reductions. We exclude known binary companions from our list of detected point sources in order to search for previously unknown companions. While we also do clearly detect PDS 70b in our observations, we do not discuss the planet nor its disk (other than showing the accompanying scattered light disk in the context of its millimeter continuum in Section 4.3), as we have thoroughly characterized the planet and its disk using the data presented herein in J. J. Wang et al. (2020).

In order to determine whether the detected point sources are real astrophysical signals instead of residual diffracted starlight, we compare the contrasts of the point sources detected with the `VIP` reductions to those of the contrasts at the same locations in the observations analyzed using `pyKLIP` (Figure 4.3). If these point sources were real, the fluxes measured between the two reductions should be consistent. The SNR maps using `pyKLIP` are derived from computing the standard deviation in 2-pixel-wide concentric annuli. For each of the 30 point sources with SNR $>$ 5 in the `VIP` SNR maps, we determine the flux and uncertainty of that point source using the maximum likelihood estimated method of the negative fake companion technique implemented in `VIP` for both our `VIP` and `pyKLIP` reductions.

The majority (24) of the 30 point sources detected in the `VIP` reductions do not have

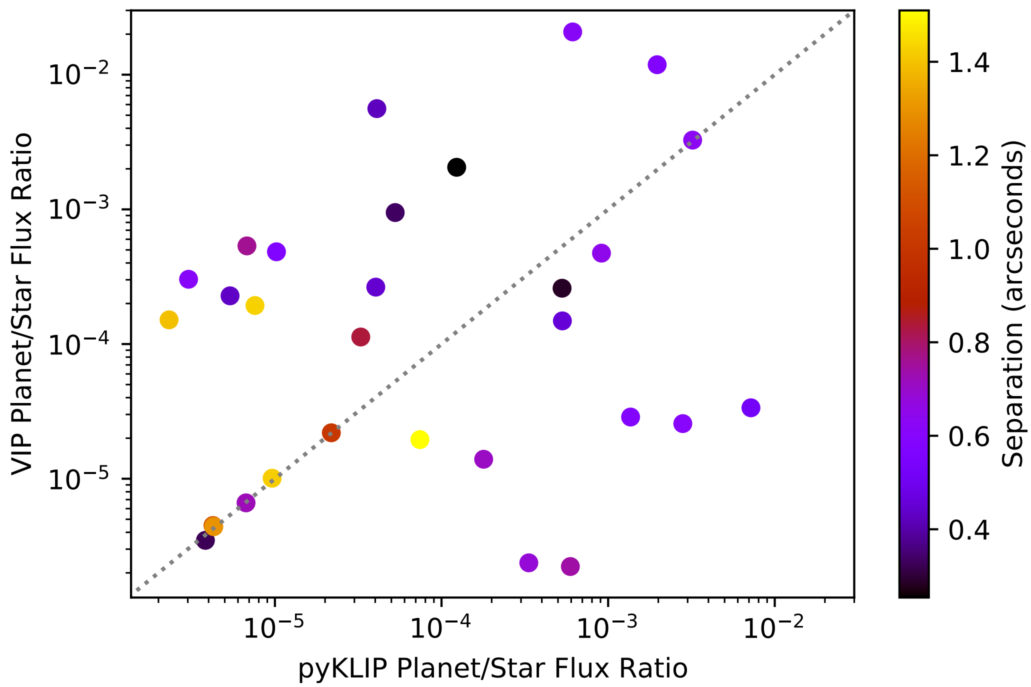

Figure 4.3: Comparison of the planet-to-star flux ratio of the point sources in Figure 4.11 determined from the `VIP` reductions versus the planet-to-star flux ratio in the same location in the `pyKLIP` reductions. A perfectly consistent flux ratio is designated by the dotted line.

consistent (at the 2σ level or better) fluxes detected in the `pyKLIP` reductions, and are therefore likely not physical. The other 6 point sources represent a combination of real disk detections that are consistent between the different reductions and observations where there are many residual speckles in the datasets due to imperfect speckle subtraction by both reduction algorithms. Of these 6 point sources, 1 (in HD 179218) is due to residual effects in the `VIP` RDI reductions due to poor reference star PSFs and a particularly noisy corresponding `pyKLIP` ADI reduction, 2 (1 in CQ Tau and 1 in LkCa 15) are due to real disk structures that appear to be point-like but are consistent with extended structure, 2 (in HL Tau) do not have the typical PSFs of point sources and instead have extended appearances likely due to diffraction from the telescope support structures, and 1 appears in the AS209 dataset with the poorer contrast and not in the observation with a better detection limit, indicating that it is not real. Therefore, by a combination of automatic and manual vetting, we do not convincingly detect any new point sources in our observations in the area between 0"15 and 1"6.

While we utilized both pyKLIP and VIP in order to vet potential point sources in our data, our VIP reductions generally achieved better contrasts than our pyKLIP reductions (Figure 4.2). Therefore, in all subsequent analyses presented herein, we present results utilizing our VIP reductions.

Scattered Light Disks

The direct detection of substructures in large grain dust as detected by ALMA and/or evidence of a gap or cavity in the stellar SED was a requirement of our target selection. Therefore, we might expect to see evidence of disk structure in all of our observations. However, in the case of the ALMA observed disks, the thermal emission of the millimeter/submillimeter sized dust grains is what is being detected, whereas in the case of near-IR observations, we are sensitive to the scattered light of the micron-sized dust. Owing to viewing geometries, the scattering properties of dust grains at different wavelengths, the luminosity of the host star, data reduction techniques, and the sensitivity of our study, we would not expect to see evidence of scattered light disks in all of our targets. We do, however, see disk structures in a subset of our observations which are consistent with the ALMA observations for these systems (Figure 4.4). We optimize the images shown in Figure 4.4 by selecting the number of principal components in our full frame images that best shows the extended structure.

For purposes of our initial survey, we limit our RDI analyses to single nights (where to first order, we expect the most similar AO correction) where the stellar PSFs of any other objects observed on the same night by the vortex coronagraph at L' act as our reference library. In this initial census of detected scattered light disks, we do not optimize this reference library herein, therefore we are not detecting every disk that would be evident from a library where stellar properties are more closely matched to the science target (such as the SR 21 disk that we present in Uyama et al. (2020), where the reference PSFs are selected across different observing nights). We also do not combine multiple observing nights that might allow for the increase in SNR needed to make the scattered light disk more evident (such as in the case of the HD 163296 disk presented in Guidi et al. (2018), where the disk was more visible when data over two consecutive nights were combined).

Stellar Parameters

Planet mass limits derived from infrared observational contrasts are a strong function of age. Therefore, it is of the utmost importance that we determine accurate ages

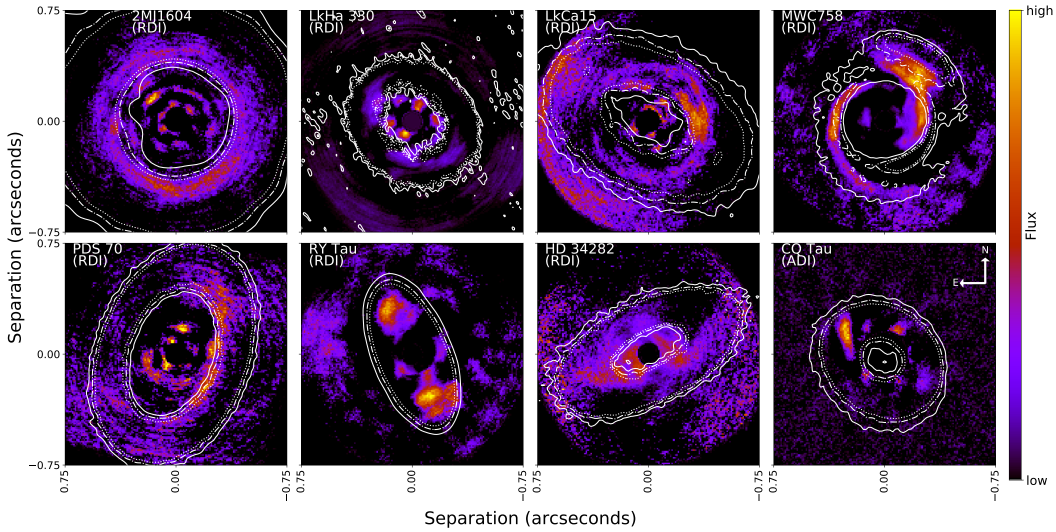

Figure 4.4: The disks in our survey that show evidence of structure which is indicative of scattered light disks. We show the 1σ (solid lines), 2σ (dashed lines), and 3σ (dotted lines) ALMA contours (from references in Table 4.1) overlaid on our 3.8 micron images for reference. North is up and east is left in all of the images. We show the reduction method and number of principal components that optimizes the appearance of the extended structure.

for our host stars (and therefore planetary systems). However, the ages of young stars are notoriously difficult to determine, so in order to allow for direct, population level analyses of planet mass upper limits, we derive uniform ages for our sample of systems.

In order to estimate the stellar ages for these protoplanetary disk-hosting stars, we first attempt to compile the stellar parameters (L_{star}, T_{eff}) required to calculate the ages of these systems as consistently as possible. Since many of the stellar parameters are sourced from references that pre-date updated Gaia distances (*Gaia* Collaboration et al., 2021), when applicable, we first rescale the stellar luminosities from the sources in Table 4.1 to account for the updated distances from Gaia. In the cases where uncertainties on the stellar luminosity and effective temperature are not published, we assume a 10% uncertainty in $\log(L_{star})$ and 2% uncertainty in T_{eff} (Pascucci et al., 2016).

We then estimate the stellar ages and masses using isochrones from Choi et al. (2016) in the range of 0.5 to 50 Myr. We interpolate the tracks to probe the mass range from 0.05 to 1.4 M_{sun}, in steps of 0.01 M_{sun}. We adopt the method described in Andrews et al. (2013) to determine stellar masses and ages. We first evaluate a likelihood function for each set of luminosities and effective temperatures (equation 1 in Andrews et al., 2013). We then marginalize the likelihood distribution and take the median of the marginalized distribution to estimate the age and mass of the star. We estimate the uncertainties as the 16% and 84% percentiles of these marginalized distributions (which takes into account the uncertainties on the stellar luminosity and effective temperature).

Our calculated ages are generally consistent at the 1σ level with those presented in the references in Table 4.1, with variations in the ages mostly due to updates to the distances to these stars as determined from updated parallaxes from Gaia (*Gaia* Collaboration et al., 2021). Therefore, we adopt our calculated ages in subsequent analyses. We modify our procedure for the close binary V4046 Sgr. While our derived age for this system is in agreement with a portion of the published literature for this system, it is not in agreement with the age of the β Pictoris moving group for which it is a member. Our calculated age from our isochrone fit is $5.62^{+4.38}_{-2.46}$ Myr and the age of the β Pictoris moving group is 23±3 Myr (Mamajek & Bell, 2014). Notably, our calculated mass of $0.9^{+0.09}_{-0.13}$ M_{sun} is in good agreement with the dynamical mass of 0.90±0.05 M_{sun} from Rosenfeld et al. (2012). Older system ages result in higher mass estimates, therefore to be most conservative, we adopt the older age of the moving group in case the luminosity measurement was contaminated from the binary component as was noted as a possibility in McCarthy and White (2012). Moreover, owing to the fact that all methods of estimating the ages of young stars (both the method that we employ and the methods employed in the literature for these systems) are rife with assumptions that bias the resulting ages, we also present the analyses in Section 4.3 and Section 4.4 independent of system age in Appendix C to show the effect of age estimation on our mass limits.

Determining Stellar L' Magnitudes

In the absence of detecting any previously unknown point sources, we seek to place constraints on the upper limits of the masses of planets that could be creating the substructures seen at other wavelengths in these disks. We can utilize our contrast limits in each of the gaps and cavities indicated by longer wavelength observations. Owing to our observing wavelength, we are more sensitive than millimeter observations to directly detecting the thermal emission of these proposed planets, and therefore our observations, despite being non-detections, can be useful in constraining the properties of these planets.

Our contrast curves can be used to estimate our mass sensitivity when paired with a host star magnitude and an evolutionary model which predicts the expected planet mass from its magnitude. In order to estimate the stellar magnitude, we utilize the WISE (for systems with $W1$ <4.5) and CATWISE (for systems with $W1$ >4.5) $W1$ and $W2$ measurements for each of our systems (3.4 and 4.6 microns; Marocco et al., 2021), and determine a predicted L' magnitude in order to determine the sensitivity of our observations. This is necessary as each of the WISE $W1$ and $W2$ bandpasses only cover a portion of the L' bandpass. Following Keppler et al. (2018), we estimate the corresponding L' magnitude by interpolating logarithmically between the $W1$ and $W2$ bands. This is necessary because these protoplanetary disk hosting stars show strong infrared excesses and therefore are often redder than would be expected for a bare stellar photosphere.

Planetary Mass Upper Limits

In order to determine the planetary masses corresponding to our contrast constraints, we use the AMES-Cond and AMES-Dusty models (Allard et al., 2012; Baraffe et al., 2003). These models provide the expected magnitude of a planet given a mass and age. We use these grids (interpolating between the grid points), the absolute magnitude limits from our 5σ contrast limits, and the estimated stellar ages to calculate the upper limits on the planet masses.

High-resolution sub-millimeter observations of disks with substructures allow us to constrain the locations of possible gap-carving planets, and can provide information about the masses of those possible planets. S. Zhang et al. (2018) carried out a series of 2D hydrodynamical simulations to infer the relationship between gaps in disks imaged with ALMA as part of the DSHARP survey (Andrews et al., 2018) and planet mass. This leads to direct predictions of masses for the objects that could be clearing out the gaps in the millimeter observations of these systems. S. Wang et al. (2021) utilized ALMA disk morphology and estimated the masses of planetary substructure drivers using the pebble isolation mass for a sample of systems that included the DSHARP (Andrews et al., 2018) sample and the systems imaged in Long et al. (2018). Lodato et al. (2019) also estimated the masses of planets in systems imaged as part of the DSHARP (Andrews et al., 2018) survey and systems in Long et al. (2018) using empirical scaling relationships. These different methods of estimating gap-opening planet masses result in differences in the masses of these objects, which can all be compared against our planet mass upper limits.

For systems from Long et al. (2018) or Andrews et al. (2018), Figure 4.5 compares our mass limits, as computed from our observed 5σ contrast limits at the radial location of the planet estimated from the ALMA radial profiles, to the masses predicted in Lodato et al. (2019), S. Wang et al. (2021), and S. Zhang et al. (2018). We account for projection effects using published inclinations in each of the references cited in Table 4.1 and account for the new parallaxes from Gaia (*Gaia* Collaboration et al., 2021) to adjust the radial separations when necessary. When systems are inclined, planetary orbits trace out ellipses, resulting in changing angular separations from the host star with inclination. In order to be conservative in our mass limits, we take the smallest angular separation consistent with the inclination. Overall, our current mass limits are not sensitive enough to probe down to the expected masses of the planets derived from the ALMA data, consistent with the lack of new point source detections herein.

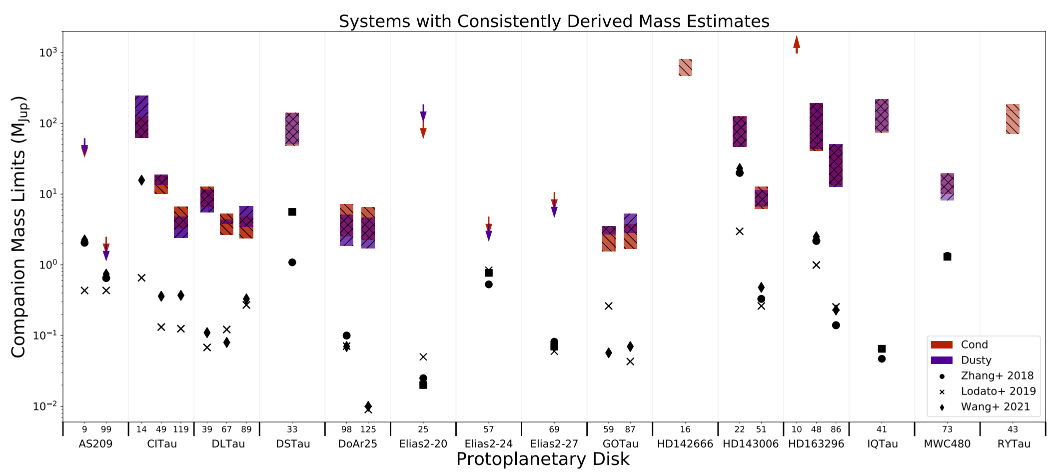

Figure 4.5: We show a comparison of the mass estimates from the ALMA data and our observational mass limits for the subset of our systems observed as part of the DSHARP Survey (Andrews et al., 2018) or the survey of the Taurus star-forming region (Long et al., 2018). We show the ALMA derived planet masses (in M_{Jup}) as the points with the mass estimates derived using the AMES-Cond models from our 5σ contrast limits shown as the orange bars for each observed gap from the ALMA data (specified in au as the numbers above each system designation). The lengths of the bars incorporate the 1σ uncertainties on the ages, stellar host magnitudes, and distances. The ages for Elias 2-20 and Elias 2-24 are lower than the youngest age in the grids. Therefore, we show the masses assuming 1 Myr as upper limits to the ages, as younger systems would result in smaller masses. The 1σ lower limit on the age of Elias 2-27 is also lower than the youngest age in the AMES-Cond grid, so we show the 1σ upper limit instead of a bar. We also show the associated masses assuming the AMES-Dusty models when the masses were within the grid in purple.

Many of our other observed systems have detected gaps in the millimeter continuum images but are not of high enough quality to be able to use the aforementioned methods from Lodato et al. (2019), S. Wang et al. (2021), and S. Zhang et al. (2018) to ascertain the planet mass. Some of these systems also show a large inner cavity devoid of dust at longer wavelengths. Those mass estimation methods from the ALMA data require a gap surrounded by dust, meaning that we cannot estimate the mass of a planet that could be carving out an inner cavity. This inner cavity could also be due to accretion of disk material onto the host star, making decoupling the influence of the possible planet on the disk in that inner region difficult. What is more, it is possible that the planets could visually (but not physically) co-locate with the scattered light from small dust grains outside of large cavities in our observations, making disk modeling a likely necessity to disentangle the two physical signals (e.g., PDS 70c in J. J. Wang et al., 2020; also see Quiroz et al., 2022 for more details about the benefits of utilizing disk modeling for increased sensitivity to planets). Additionally, bright disk signals at similar radii to planets may bias both contrast curve and SNR estimates of point-like sources and due to the filtering of extended signals into point-like sources, the use of dedicated techniques (e.g., MAYONNAISE (Pairet et al., 2021), REXPACO (Flasseur et al., 2021)) may be necessary to reliably image both point sources and extended signals. However, there are a number of other methods to estimate the masses of planets that could be creating the cavities and gaps seen in the millimeter. We show the estimated masses of the putative companions, where available in the published literature, in Figure 4.6.

The other systems in our survey do not have high enough resolution ALMA data (DoAr 28 and DO Tau), clear evidence for a gap in millimeter images but were taken as part of the DSHARP survey (Andrews et al., 2018; AS 205 and WSB 52), or are spiral systems without a consistent radial distance for which a gap is cleared (WaOph 6 and MWC 758). Therefore, instead of comparing our mass detection limits to locations of interest in each disk, we calculate our mass limits over all radial separations from the host star (Figure 4.7). Additionally, we show our average survey sensitivity over all separations in Figure 4.8 determined using `Exo_DMC` (Bonavita, 2020). In brief, `Exo_DMC` uses a Monte Carlo approach to determine the fraction of planets on Keplerian orbits that would have been recovered given an observational mass limit with separation.

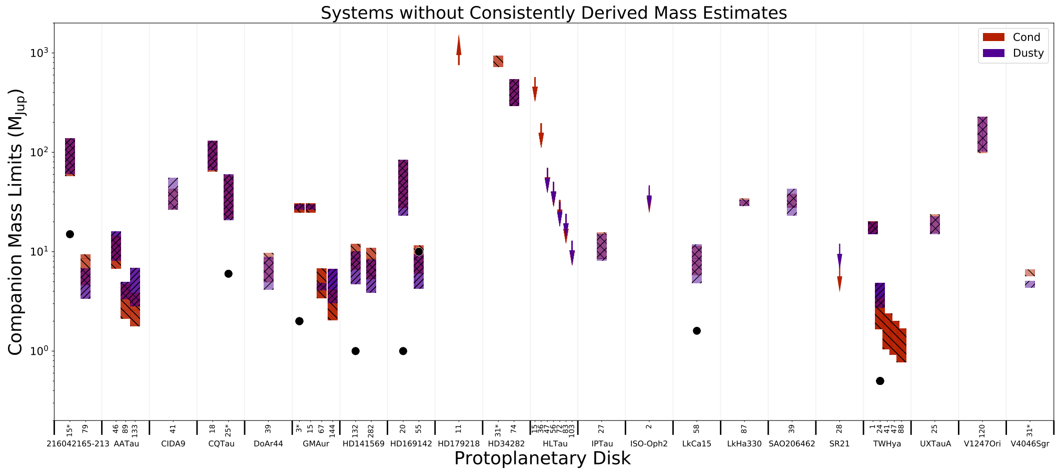

Figure 4.6: We show the mass estimates derived from our 5σ contrast limits (in M_{Jup}) in each gap/cavity (specified in au above each system designation) as the bars colored by radial distance from the host star. The lengths of the bars incorporate the 1σ uncertainties on the ages, stellar host magnitudes, and distances. The ages for HL Tau, ISO-Oph 2, and SR 21 are lower than the youngest age in the grids, therefore we show the masses assuming an age of 1 Myr as an upper limit to the ages, as a younger system would correspond to smaller mass. We also show the associated masses assuming the AMES-Dusty models when the masses were within the grid in purple. There is a subset of systems that have estimates of planetary masses not ascertained via the Lodato et al. (2019), S. Wang et al. (2021), and S. Zhang et al. (2018) methods. The putative companion at 15 au in 2MASS J16042165-2130284 is detailed in Canovas et al. (2017), the putative companion at 25 au in CQ Tau is detailed in Wölfer et al. (2021), the putative companion in HD 141569 is detailed in Konishi et al. (2016), and the putative companion in GM Aur at 3 au is detailed in Rice et al. (2003). The putative companions in each of the two gaps in HD 169142 have mass estimates of between 0.1-1M_{Jup} for the inner planet and 1-10M_{Jup} for the outer planet, so we show the upper limits for these masses (Fedele et al., 2017). The putative companion in TW Hya is detailed in Dong and Fung (2017). We show the expected planet masses as the circles. In cases where a planet was hypothesized to be creating the observed substructure, but is not thought to be present in the location of the gap, we designate the location with a star next to the radial location.

4.4 Discussion

Investigating Disk Viscosity Constraints

Determining the mass of a planet carving out a gap at sub-millimeter wavelengths requires assumptions about the natal disk's viscosity, α (S. Wang et al., 2021; S. Zhang et al., 2018). Therefore, if we compare the calculated masses of planets using different values for the disk viscosity, and find that our sensitivity at L' predicts a mass that is below one or more of the masses calculated using different

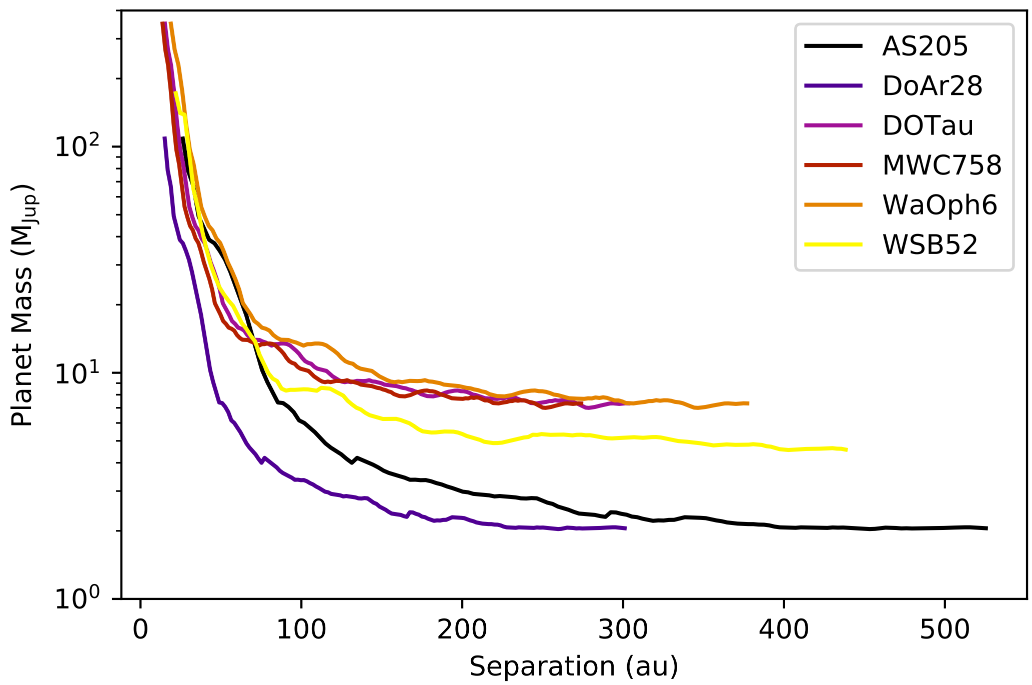

Figure 4.7: Companion mass upper limits as a function of separation (in au) for the systems studied herein which did not have clear locations where a planet would be present.

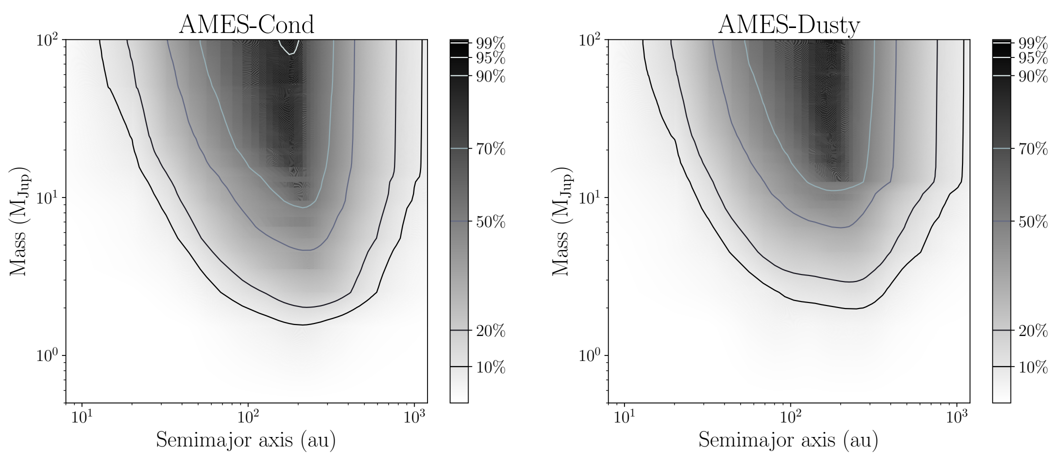

Figure 4.8: A map of the average sensitivity of our survey in planet mass (calculated using the AMES-Cond and AMES-Dusty models) versus separation in au calculated using `Exo_DMC` (Bonavita, 2020).

disk viscosities, we may be able to place observational constraints on this parameter with the caveat that we are assuming the AMES-Cond and AMES-Dusty models. In order to compare our mass limits with those of masses determined with different values for α, we again utilize the subset of our observations with ALMA data taken as part of the DSHARP survey (Andrews et al., 2018) or the survey of systems in the Taurus star-forming region (Long et al., 2018). The DSHARP survey is one of the highest angular resolution surveys at millimeter wavelengths, which allows for robust planetary mass predictions. Moreover, S. Zhang et al. (2018) directly computed the predicted masses of substructure drivers for different values of α for the DSHARP sample. S. Wang et al. (2021) also directly computed the predicted masses of substructure driving planets at different values for α for systems in Andrews et al. (2018) and Long et al. (2018).

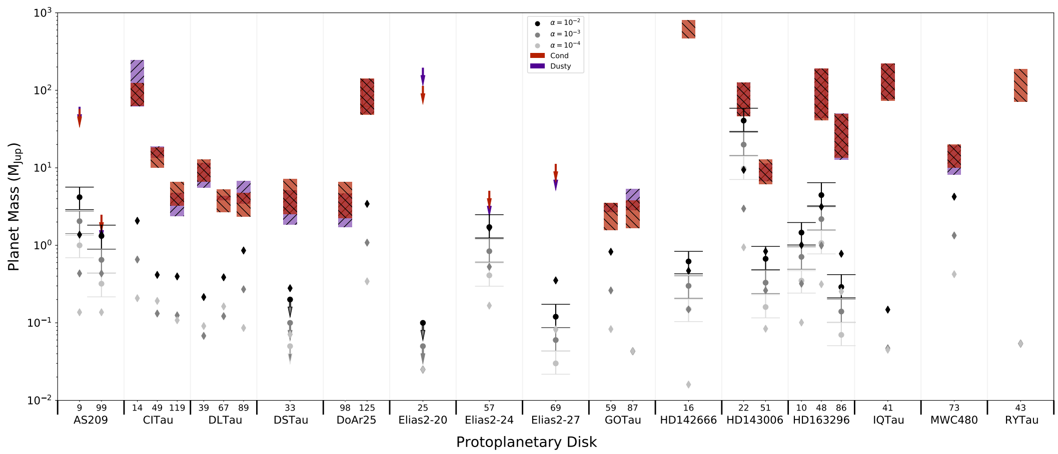

Figure 4.9: Expected planet masses from S. Wang et al. (2021) (diamonds) and S. Zhang et al. (2018) (circles), using different values for the disk viscosity, α, are shown as black and gray points. We show our planet mass detection limits for comparison using the AMES-Cond and AMES-Dusty models (Allard et al., 2012; Baraffe et al., 2003) for the subset of our systems observed as part of the DSHARP survey (Andrews et al., 2018) or the survey of the Taurus star-forming region (Long et al., 2018). The ages for Elias 2-20 and Elias 2-24 are lower than the youngest age in the grids. Therefore, we show the masses assuming 1 Myr as upper limits to the ages, as younger systems would result in smaller masses. The 1σ lower limit on the age of Elias 2-27 is also lower than the youngest age in the grids, so we show the 1σ upper limit instead of a bar. Otherwise, the lengths of the bars account for the 1σ spread in the mass limits owing to the uncertainties on the system ages, stellar host magnitudes, and system distances.

As shown in Figure 4.9, our L' mass sensitivities do overlap with the masses predicted from the method in S. Zhang et al. (2018) for a number of targets when assuming α=10^{-2}. These overlapping values within their errors means that we cannot conclusively exclude this α=10^{-2} value observationally, but it does indicate that we would possibly be sensitive to massive planets in AS 209, Elias 2-24, and

HD 143006. As with the mass estimations, uncertainties in the ages estimated for the host stars also add uncertainty to conclusions that can be made about the disk viscosity (see Figure 4.14 for a comparison of the masses derived from our 5σ contrast limits at different system ages with the masses estimated using different disk viscosities). The fact that we do not detect planets in any of these systems, might be tentative evidence that the disk viscosity for these systems (and indeed protoplanetary disks in general), might be less than this 10^{-2} value. This is consistent with α constraints from millimeter CO measurements (for example, Flaherty et al. (2018) constrained the disk viscosity to α <0.007 within a narrow region around the midplane of TW Hya and Villenave et al. (2022) found that α <10^{-5} at 100 au in Oph163131). However, an important caveat to this is that we are not sensitive enough to detect planets regardless of the disk viscosity assumed using the mass estimates from S. Wang et al. (2021).

Limits on Planetary Accretion Rates

Although we do not detect any new planets, and indeed do not seem to be able to achieve the sensitivity needed to directly detect the thermal emission of the planets thought to be creating the substructures seen at millimeter wavelengths (Figure 4.5), we can still place observational constraints on the nature of these planets. As forming protoplanets accrete their envelopes from their natal disks, the brightness associated with this accretion can surpass the intrinsic luminosity of the planet's residual heat of formation (Szulágyi et al., 2019; Zhu, 2015). Therefore, assuming that we are not sensitive enough to detect the planet's thermal emission, we can utilize our contrast limits to place constraints on the accretion, assuming all of the luminosity that would be visible would be due to accretion. Zhu (2015) related the expected magnitude to the circumplanetary accretion rate $M_p\dot{M}$. Generally, the mass of the planet cannot be disentangled from the mass accretion rate using infrared photometry, but utilizing the mass constraints from ALMA observations, and our contrast limits, we can break this degeneracy. We show the upper limits to the mass accretion rates for the planets studied herein with masses derived in S. Wang et al. (2021) and S. Zhang et al. (2018) as a function of circumplanetary disk radius, R_{in}, in Figure 4.10. The mass accretion rates that we derive are larger than those from Hα measurements of the actively accreting protoplanet PDS 70c ($10^{-8.0\pm0.4}$ $M_{Jup}yr^{-1}$; Benisty et al., 2018, Haffert et al., 2019), but are consistent with those derived from infrared observational limits (Ruane et al., 2017).

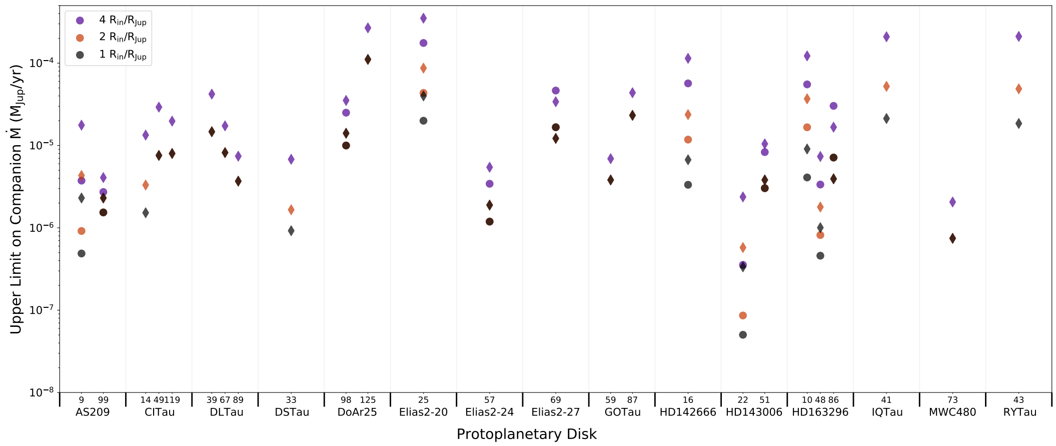

Figure 4.10: Upper limits on the mass accretion rates as a function of circumplanetary disk radius, R_{in}, for the subset of our systems observed as part of the DSHARP Survey (Andrews et al., 2018) or the survey of the Taurus star-forming region (Long et al., 2018), derived from Zhu (2015) and determined from our contrast limits (and the AMES-Cond models) and masses from S. Wang et al., 2021 (diamonds) and S. Zhang et al., 2018 (circles) assuming a disk viscosity of α=10^{-3}.

4.5 Conclusions

We present new deep L' observations of 43 protoplanetary disks using the NIRC2 vortex coronagraph at Keck. We primarily selected systems that had evidence of substructures in their millimeter/sub-millimeter continuum images in order to ascertain if we could directly detect planets that could be forming these substructures. While we do not detect any novel point sources, we are able to utilize our detection limits to place robust upper limits on the masses of planets in these disks. We present contrast curves for these systems and utilizing newly derived stellar ages, stellar L' magnitudes, and the AMES-Cond and AMES-Dusty models (Allard et al., 2012; Baraffe et al., 2003) are able to place upper limits on the masses of planets in these systems. While we are not sensitive enough to observe planets of the masses predicted by sub-millimeter observations, we do probe down to ~1 M_{Jup} for a number of systems that we observed. Meaning that if planets are the primary driver for the observed substructures in the sub-millimeter observations of these disks, then they must be under our observational sensitivity for each system and sub-Jovian for a number of our observed systems. Utilizing our mass upper limits, we also investigate constraints that we can place on the viscosity of the disk, possibly allowing us to exclude α >10^{-2}. From our observational sensitivities and the masses derived from ALMA observations, we are able to place limits on the mass accretion rates for a subset of systems studied herein.

We also detect scattered light disks in a number of our observations, which will allow for a detailed study of the properties of the dust in protoplanetary disks when observed at multiple wavelengths. Multi-wavelength studies of protoplanetary disks will provide insight into the radial distributions of different sized dust in these disks, ultimately allowing for a better understanding of the natal disk environment and the availability of planetary building blocks.

Future observations of these systems with the next generation of larger primary mirror ground-based telescopes will likely be needed in order to reach down to the sensitivities required to detect these planets directly. Achieving the sensitivity needed to observe planets of the masses predicted by millimeter observations will be needed to definitively ascertain the nature of the disk substructures revealed by ALMA.

4.6 Appendix

System Parameters and Observing Details

We show the system parameters in Table 4.1 and the observation details in Table 4.2.

System	Distance[a] (pc)	T_{eff} (K)	L[b] (L_{sun})	M_{star}[c] (M_{sun})	Age[c] (Myr)	L'[d] (mag)	Ref.[e]
2MJ1604[f]	145.31±0.57	4898±180	0.58±0.33	$1.06^{+0.13}_{-0.16}$	$12.59^{+12.53}_{-5.51}$	7.58±0.02	1,2
AA Tau	134.67±1.57	3763±173[g]	0.41±0.10	$0.56^{+0.16}_{-0.12}$	$2.51^{+2.50}_{-1.10}$	7.19±0.02	3,4
AS 205	142.14±2.81	4266±295	2.64±0.75	$0.88^{+0.33}_{-0.26}$	$0.63^{+0.95}_{-0.35}$	4.19±0.34	5,5
AS 209	121.25±0.43	4266±295	1.42±0.67	$0.87^{+0.23}_{-0.22}$	$1.58^{+3.43}_{-0.95}$	6.53±0.03	5,5
CIDA 9	175.08±2.69	3585±165[g]	0.21±0.05	$0.45^{+0.14}_{-0.1}$	$4.47^{+4.45}_{-2.23}$	8.91±0.01	3,6
CI Tau	160.32±0.53	4277±197[g]	0.83±0.19	$0.92^{+0.14}_{-0.17}$	$2.82^{+2.19}_{-1.23}$	6.79±0.02	3,6
CQ Tau	149.37±1.34	6900±318	8.93±2.07	$1.57^{+0.11}_{-0.1}$	$11.22^{+11.17}_{-2.31}$	6.63±0.06	7,8
DL Tau	159.94±0.50	4277±197[g]	0.65±0.15	$0.92^{+0.12}_{-0.15}$	$3.98^{+3.10}_{-1.74}$	7.20±0.02	3,6
DoAr 25	138.16±0.82	4266±295	0.96±0.46	$0.86^{+0.21}_{-0.2}$	$2.51^{+4.57}_{-1.39}$	6.78±0.02	5,5
DoAr 28	135.60±0.49	4350±200	1.28±0.30	$0.95^{+0.18}_{-0.18}$	$1.78^{+1.38}_{-0.78}$	7.24±0.02	9,10
DoAr 44	146.32±0.49	4730±218	1.92±0.45	$1.26^{+0.12}_{-0.19}$	$2.00^{+1.55}_{-0.87}$	8.13±0.02	11,12
DO Tau	138.52±0.68	3806±175[g]	0.22±0.05	$0.61^{+0.12}_{-0.13}$	$7.08^{+5.51}_{-3.10}$	6.68±0.03	3,13
DS Tau	158.35±0.53	3792±175[g]	0.24±0.06	$0.61^{+0.12}_{-0.13}$	$6.31^{+4.91}_{-3.15}$	7.26±0.02	3,6
Elias 2-20	137.53±3.96	3890±269	2.22±1.07	$0.58^{+0.22}_{-0.13}$	$0.63^{+4.38}_{-0.41}$	5.95±0.05	5,5
Elias 2-24	139.26±1.24	4266±295	6.32±2.87	$0.92^{+0.36}_{-0.22}$	$0.35^{+1.23}_{-0.20}$	6.42±0.03	5,5
Elias 2-27	110.07±10.30	3890±269	0.82±0.51	$0.61^{+0.2}_{-0.18}$	$2.51^{+8.71}_{-1.80}$	7.22±0.02	5,5
GM Aur	158.11±1.22	4115±190[g]	0.62±0.15	$0.81^{+0.14}_{-0.16}$	$3.16^{+2.46}_{-1.38}$	8.17±0.01	3,14
GO Tau	142.38±0.41	3516±162[g]	0.21±0.05	$0.4^{+0.13}_{-0.1}$	$3.16^{+3.92}_{-1.38}$	8.84±0.02	3,6
HD 141569	111.61±0.36	9750±125	25.34±0.58	$2.2^{+0.01}_{-0.01}$	$17.78^{+17.70}_{-8.87}$	6.70±0.02	15,16
HD 142666	146.25±0.46	7500±250	9.28±4.58	$1.6^{+0.11}_{-0.07}$	$19.95^{+15.53}_{-9.95}$	5.32±0.08	5,5
HD 143006	167.34±0.51	5623±259	3.91±1.34	$1.68^{+0.26}_{-0.25}$	$4.47^{+4.45}_{-1.95}$	6.28±0.04	5,5

System	Distance[a] (pc)	T_{eff} (K)	L[b] (L_{sun})	M_{star}[c] (M_{sun})	Age[c] (Myr)	L'[d] (mag)	Ref.[e]
HD 163296	100.97±0.42	9250±250	16.97±12.69	$2.02^{+0.09}_{-0.06}$	$15.85^{+15.77}_{-6.94}$	3.43±0.44	5,5
HD 169142	114.87±0.35	7500±346	5.90±25.48	$1.6^{+0.18}_{-0.1}$	$17.78^{+17.70}_{-8.87}$	6.30±0.04	17,18
HD 179218	260.09±2.23	9640±444	104.85±30.00	$2.52^{+0.34}_{-0.32}$	$3.55^{+14.23}_{-1.31}$	4.48±0.25	19,20
HD 34282	308.61±2.20	9250±125	14.66±0.67	$1.95^{+0.02}_{-0.01}$	$19.95^{+15.53}_{-7.36}$	7.04±0.02	15,21
HL Tau[h]	147.30±0.50	4400±203	9.25±5.50	$1.03^{+0.28}_{-0.2}$	$0.32^{+1.68}_{-0.17}$	5.07±0.08	22,23
IP Tau	129.38±0.29	3763±173[g]	0.33±0.08	$0.58^{+0.14}_{-0.13}$	$3.55^{+3.53}_{-1.55}$	7.62±0.01	3,6
IQ Tau	131.51±0.62	3690±170[g]	0.22±0.05	$0.53^{+0.14}_{-0.12}$	$5.62^{+5.60}_{-2.81}$	7.13±0.02	3,6
ISO-Oph2	134.25±7.56	3467±160	0.71±0.17	$0.31^{+0.09}_{-0.05}$	$0.40^{+0.40}_{-0.24}$	8.44±0.02	24,25
LkCa 15	157.19±0.65	4277±197[g]	0.77±0.18	$0.92^{+0.14}_{-0.16}$	$3.16^{+2.46}_{-1.38}$	7.67±0.02	3,26
LkHa 330	318.22±3.49	6220±287[g]	16.55±3.84	$2.24^{+0.32}_{-0.26}$	$3.16^{+1.85}_{-1.17}$	6.40±0.04	3,10
MWC 480	156.22±1.26	8250±380	17.81±5.50	$1.85^{+0.12}_{-0.1}$	$14.13^{+17.50}_{-7.05}$	4.73±0.09	6,16
MWC 758	155.87±0.76	8130±375	16.30±3.79	$1.84^{+0.11}_{-0.09}$	$12.59^{+15.59}_{-5.51}$	5.18±0.10	27,28
PDS 70	112.39±0.24	3972±36	0.34±0.09	$0.75^{+0.03}_{-0.04}$	$5.62^{+4.38}_{-2.08}$	8.01±0.02	29,30
RY Tau	138.22±3.88	5930±273[g]	11.93±2.77	$2.28^{+0.34}_{-0.31}$	$2.51^{+1.95}_{-1.10}$	3.82±0.11	3,6
SAO 206462	135.00±0.44	6250±125	5.17±0.12	$1.45^{+0.04}_{-0.01}$	$10.00^{+1.22}_{-1.09}$	5.26±0.09	15,31
SR 21	136.43±0.56	4571±211	3.77±0.88	$1.2^{+0.29}_{-0.25}$	$0.71^{+0.70}_{-0.31}$	6.04±0.03	24,32
TW Hya	60.14±0.05	3776±174[g]	0.24±0.05	$0.59^{+0.13}_{-0.13}$	$6.31^{+4.91}_{-3.15}$	7.20±0.02	3,33
UX TauA	142.23±0.67	4870±224[g]	1.64±0.38	$1.27^{+0.09}_{-0.13}$	$3.16^{+3.15}_{-1.38}$	6.87±0.02	3,10
V1247 Ori	401.30±3.16	8500±250	14.59±1.50	$1.88^{+0.06}_{-0.04}$	$15.85^{+15.77}_{-6.94}$	6.42±0.03	34,35

System	Distance[a] (pc)	T_{eff} (K)	L[b] (L_{sun})	M_{star}[c] (M_{sun})	Age[c] (Myr)	L'[d] (mag)	Ref.[e]
V4046 Sgr	71.48±0.11	4260±196	0.49±0.11	$0.9^{+0.09}_{-0.13}$	$5.62^{+4.38}_{-2.46}$, 23±3[i]	7.27±0.02	36,37
Wa Oph 6	122.53±0.35	4169±288	2.86±1.38	$0.78^{+0.28}_{-0.2}$	$0.71^{+2.45}_{-0.46}$	6.36±0.03	5,5
WSB 52	135.27±0.92	3715±257	0.70±0.34	$0.51^{+0.19}_{-0.17}$	$1.78^{+7.13}_{-1.22}$	7.32±0.02	5,5

Table 4.1: System Parameters

[a]We use parallax values from Gaia EDR3 (*Gaia* Collaboration et al., 2021).
[b]We scale the luminosities in the cited references to the new distances from Gaia EDR3 (*Gaia* Collaboration et al., 2021).
[c]Our ages and stellar masses, computed using fits to isochrones (as described in Section 4.3).
[d]We calculate L' magnitudes by logarithmically interpolating the WISE $W1$ and $W2$ magnitudes.
[e]References: the source of the initial stellar parameters that were rescaled when necessary to account for new distances from Gaia EDR3 (*Gaia* Collaboration et al., 2021), a reference for a longer-wavelength observation for the disk.
[f]Full name: 2MASS J16042165-2130284
[g]The T_{eff} for this system is determined using Table 5 in Herczeg and Hillenbrand (2014), where we interpolate between stellar types when necessary.
[h]Parallax measurement from Galli et al. (2018).
[i]While the mass that we derive from our isochrone fit is consistent with the published dynamical mass (Rosenfeld et al., 2013) and our derived age ($5.62^{+4.38}_{-2.46}$ Myr) is consistent with a portion of the published ages for this system, the age is at odds with that of the β Pictoris moving group (23±3 Myr) for which it is a member (Mamajek & Bell, 2014). V4046 Sgr is a tight binary, so despite the agreement of our masses, we elect to use 23±3 Myr as the age of this system to mitigate any possible contamination on the stellar luminosity from the binary component.

(1) Carpenter et al. (2014), (2) K. Zhang et al. (2014), (3) Herczeg and Hillenbrand (2014), (4) Loomis et al. (2017), (5)Andrews et al. (2018), (6) Long et al. (2018), (7) Testi et al. (2003), (8)Ubeira Gabellini et al. (2019), (9) Kim et al. (2013), (10) Rich et al. (2015), (11) Andrews et al. (2011), (12) Cieza et al. (2021), (13) Kwon et al. (2015), (14) Huang et al. (2020), (15) Guzmán-Díaz et al. (2021), (16) Konishi et al. (2016), (17) Meeus et al. (2012), (18) Fedele et al. (2017), (19) Menu et al. (2015), (20) Kluska et al. (2018), (21) van der Plas et al. (2017), (22) van der Marel et al. (2019), (23) Carrasco-González et al. (2019), (24) Manara et al. (2015), (25) González-Ruilova et al. (2020), (26) Isella et al. (2012), (27)Boehler et al. (2018), (28) Dong et al. (2018), (29)Keppler et al. (2018), (30) Keppler et al. (2019), (31) van der Marel et al. (2016), (32) Pinilla et al. (2015), (33) Nomura et al. (2016), (34) Kraus et al. (2013), (35) Kraus et al. (2017), (36) McCarthy and White (2012), (37) Rosenfeld et al. (2013)

Locations of Point Source Detections

We show the locations of the point sources that had SNR>5 between 0."15 and 1."6 in our `VIP` reductions. We vet these point sources in Section 4.3, which all appear to be false positives. As evident by the weighted histogram in Figure 4.11, we have more false positives at smaller separations due to imperfect starlight suppression.

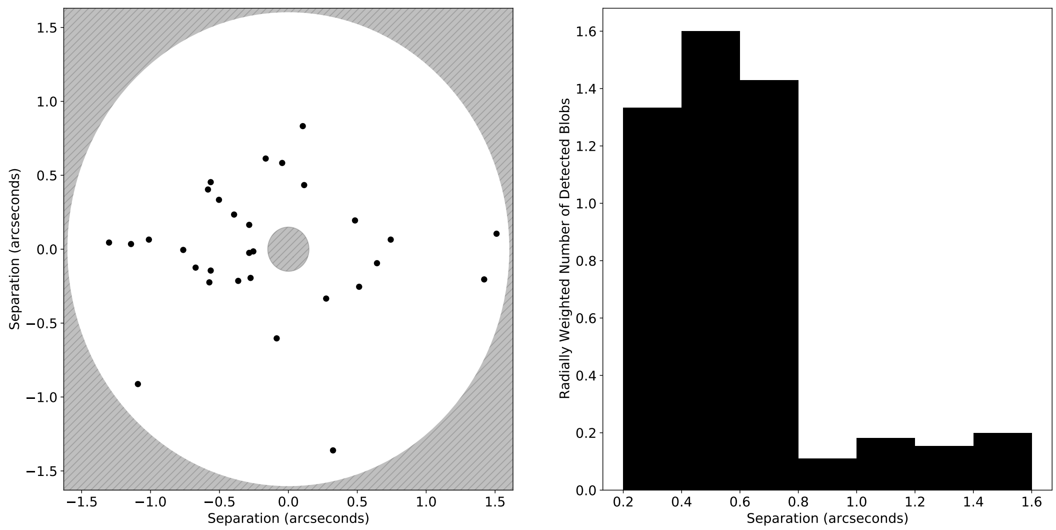

Figure 4.11: Left: Locations of all point sources detected in our observations with SNR >5. The central 0."15 and separations> 1."6 are hatched and represent the regions where we do not search for point sources. Right: A histogram, weighted by area, of the separations of the detected point sources.

Age Independent Mass Estimates

The ages of young stars are notoriously difficult to ascertain. In Figures 4.5-4.9, we utilize our best isochrone determined ages when estimating our planetary mass limits. Here we show our gap and cavity mass plots for a variety of system ages.

System	UT Date	Total Frames	Total Integration Time (s)	PA rotation (°)
2MJ1604[a]	2017-05-10	73	3285	36.2
AA Tau	2020-10-25	153	459	161.3
AS 205	2019-06-18	43	129	139.4
AS 209	2018-05-26	60	270	33.0
	2018-05-28	145	435	54
	2018-07-23	90	270	27.1
	2018-07-30	120	360	44.5
CIDA 9	2020-10-25	83	249	18.5
CI Tau	2018-10-21	132	396	161.2
	2018-12-23	87	261	182.0
CQ Tau	2018-12-24	60	180	111.0
DL Tau	2019-01-09	160	480	220.3
DoAr 25	2019-06-08	64	192	30.9
DoAr 28	2017-07-01	90	405	41.7
DoAr 44	2017-06-13	54	162	21.4
	2017-06-30	100	375	42.1
DO Tau	2020-10-09	44	1188	19.0
DS Tau	2020-10-09	65	195	78.9
Elias 2-20	2020-05-29	143	715	72.4
Elias 2-24	2019-02-17	20	60	8.2
	2020-06-01	161	483	56.9
Elias 2-27	2019-05-22	30	90	16.9
	2020-05-30	131	393	54.7
GM Aur	2017-01-14	120	540	126.7
GO Tau	2020-11-27	90	270	11.5
HD 141569	2015-06-11	39	78	49.3
HD 142666	2019-06-18	75	225	38.7
HD 143006	2019-05-21	76	228	42.5
	2019-06-08	60	180	29.2
HD 163296	2017-05-31	80	240	40.4
HD 169142	2020-05-31	78	234	28.9
HD 179218	2016-08-14	45	2025	130.1
	2016-09-11	25	120	0.4
	2016-10-17	30	144	0.8
	2017-06-01	80	240	131
HD 34282	2017-02-07	73	3285	61.3
	2017-10-12	49	147	24.6
	2017-10-13	139	417	60.7

System	UT Date	Total Frames	Total Integration Time (s)	PA rotation (°)
HL Tau	2015-10-22	10	25	0.1
	2017-12-26	105	210	161.3
IP Tau	2017-10-03	130	546	211.6
IQ Tau	2020-11-27	84	252	16.5
ISO-Oph 2	2021-05-19	237	711	68.4
LkCa 15	2015-10-22	81	2025	156.9
	2015-10-24	22	55	8.5
	2015-12-27	50	150	129.6
	2017-01-12	101	2272.5	160.8
	2017-12-24	17	51	1.4
	2020-10-10	101	303	43.7
LkHa 330	2015-10-22	44	110	41.1
	2018-12-25	93	279	38.3
MWC 480	2018-12-23	80	240	132.2
	2018-12-24	140	420	87.9
MWC 758	2015-10-24	81	2025	128.8
	2016-10-24	80	320	173.2
PDS 70	2019-06-08	42	126	27.8
RY Tau	2015-10-22	33	825	12.0
	2015-10-24	83	2075	105.3
	2017-12-24	20	90	33.3
SAO 206462	2016-05-27	80	240	23.0
SR 21	2020-05-31	137	411	56.3
TW Hya	2016-04-13	70	210	21.6
	2017-01-09	120	540	44.4
	2017-01-13	117	5265	44.7
	2019-02-17	64	192	33.2
UX Tau A	2016-10-16	116	232	199.5
	2017-02-11	50	120	156.3
	2017-10-04	128	5376	164.2
V1247 Ori	2017-12-27	51	153	4.0
V4046 Sgr	2017-05-11	70	315	28.3
WaOph 6	2020-05-30	41	123	13.3
WSB 52	2020-06-02	168	504	68.3

Table 4.2: Observation Log

[a]Full name: 2MASS J16042165-2130284

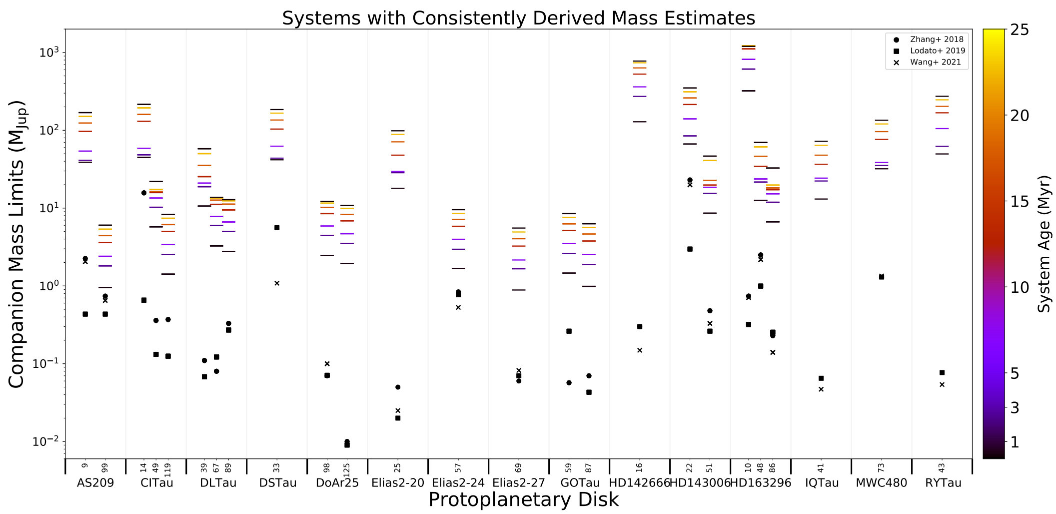

Figure 4.12: Similar to Figure 4.5, but showing the mass estimates derived from our 5σ contrast limits for a number of different system ages for systems observed as part of the DSHARP survey (Andrews et al., 2018) or the survey of the Taurus star-forming region (Long et al., 2018). We show the ALMA derived planet masses (in M_{Jup}) as the points with our mass estimates using the AMES-Cond model shown as bars colored by system age. We specify the radial locations of the gaps that we are probing as numbers (in au) above each system name. There are a number of gaps where the derived masses are outside of the AMES-Cond model grid for certain ages and are therefore not shown.

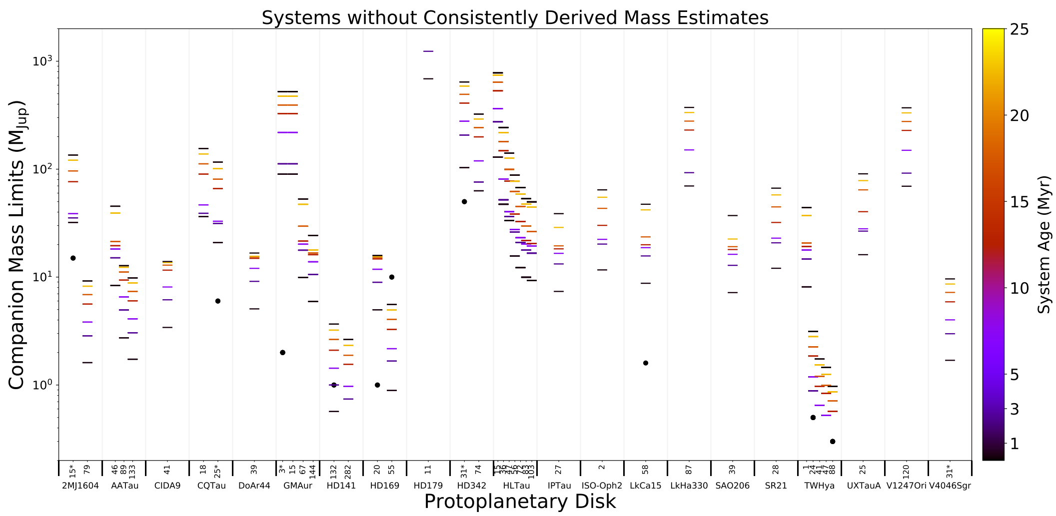

Figure 4.13: Similar to Figure 4.6, but showing the mass estimates derived from our 5σ contrast limits for a number of different system ages. We show our mass estimates using the AMES-Cond model as bars colored by system age. We specify the radial locations of the gaps that we are probing as numbers (in au) above each system name. There are a number of ages for the multiple gaps in TW Hya which produce mass limits outside of the AMES-Cond model grid, so we do not show those limits. In cases where a planet was hypothesized to be creating the observed substructure, but is not thought to be present in the location of the gap, we designate the location with a star next to the radial location.

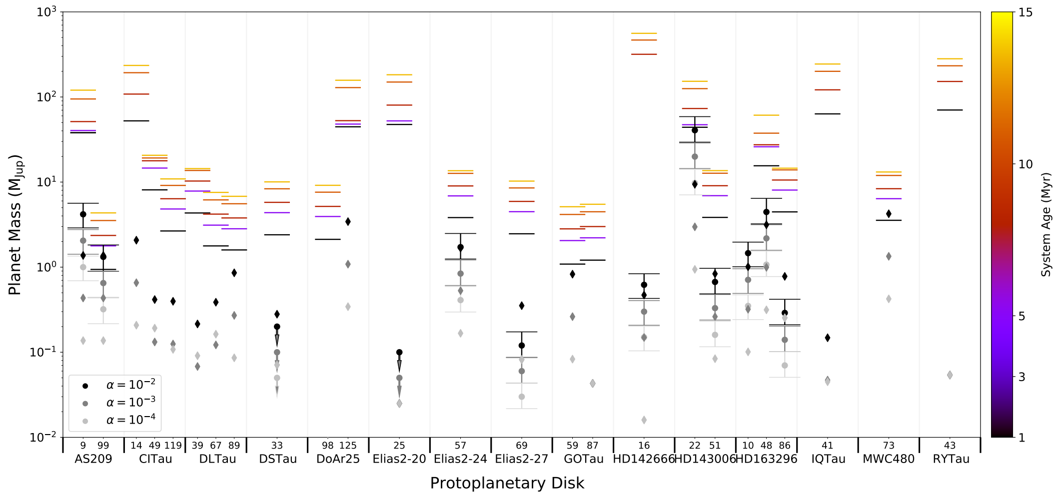

Figure 4.14: Similar to Figure 4.9, expected planet masses from S. Wang et al. (2021) (diamonds) and S. Zhang et al. (2018) (circles) for the subset of our systems observed as part of the DSHARP survey (Andrews et al., 2018) or the survey of the Taurus star-forming region (Long et al., 2018) calculated using different values for the disk viscosity, α, are shown as black and gray points. We show the planet mass estimates derived from our 5σ contrast limits for comparison using the AMES-Cond models (Baraffe et al., 2003). There are a number of gaps where the derived masses are outside of the AMES-Cond model grid for certain ages and are therefore not shown.

Chapter 5

CONCLUSIONS

In this thesis, we have explored the formation and evolution of gas giant exoplanets utilizing both direct imaging constraints and atmospheric characterization of transiting planets. In Chapter 2, we studied the atmospheric metallicity of a subset of transiting close-in gas giant planets as viewed in secondary eclipse in order to determine if the trend that is seen in the solar system giant planets is generalizable to all planetary systems. The giant planets in our own solar system show a tight trend of decreasing atmospheric metallicity with increasing planet mass (e.g., Lodders, 2003). If this is a fundamental part of the planet formation process, this trend should also be evident in exoplanets. In order to probe atmospheric metallicity, we focused on just the $\lesssim$1000 K close-in transiting gas giants, where we could take advantage of the equilibrium chemistry expectations for carbon bearing species. We detected new *Spitzer* secondary eclipses for four (out of five total) cool planets, greatly expanding the sample of planets with thermal emission measurements in this temperature regime. Using our newly expanded sample, we did not recover the solar system trend of increasing metallicity with decreasing mass, indicating that planets of similar mass appear to have diverse atmospheric compositions that reflect their varied formation histories. In hindsight this should not have been surprising, as these systems also have architectures that are quite different than that of the solar system.

In Chapter 3, we measured new *Spitzer Space Telescope* eclipse depths for five planets. We then went on to place these new detections into the broader context of all planets with detected *Spitzer* secondary eclipses in order to explore what factors govern the thermal emission of short period gas giant planets in an effort to better understand the formation histories of this population of planets. The atmospheric compositions of these objects are primarily influenced by their stellar environment. We were also able to reconfirm a trend of decreasing planetary circulation efficiency with increasing equilibrium temperature using one of the largest samples of planets currently published.

While we were able to get a first look at the chemistry and physics of the atmospheres of short-period gas giant exoplanets using the *Spitzer Space Telescope* in Chapters

2 and 3, impending observations by the *James Webb Space Telescope* (*JWST*) at higher signal to noise and higher spectral resolution will provide significantly more precise measurements of their atmospheric compositions (Bean et al., 2018). While we were limited to two relatively low signal-to-noise broadband photometric data points for these analyses, *JWST* will be able to resolve individual molecular bands, and resolve degeneracies inherent in the interpretation of many *Spitzer* data sets. Many of the targets that were studied herein will be observed with *JWST* and allow for updated constraints on the nature of their atmospheres.

In Chapter 4, we focus on the constraints we can put on giant planet formation using direct imaging. We observed 43 protoplanetary disks that showed substructure thought to be due to planet-disk interactions in the L′-band using Keck/NIRC2. Although we were not able to directly detect any substructure driving planets, using our observational sensitivities we were able to place upper limits on the masses of planets in these systems down to a few Jupiter masses for a portion of our survey targets. If planets are the primary drivers of the observed substructure, our current observational capabilities are not sensitive enough to directly detect planets of those masses. However, the next generation of larger primary mirror ground-based telescopes will allow us to gain new insight into these systems (Bowens et al., 2021; Currie et al., 2019). These larger telescopes will allow for increased angular resolution, allowing us to probe closer in to the host stars, and increased sensitivity to lower mass planets. These new instruments will likely uncover a larger population of planets embedded in protoplanetary disks, providing new insight into planet-disk interactions. New instruments to characterize the atmospheres of directly imaged giant planet at high spectral resolution (e.g., the Keck Planet Imager and Characterizer; Delorme et al., 2021) will further allow us to understand the atmospheres of giant planets in the context of their natal disks.

BIBLIOGRAPHY

Agúndez, M., Parmentier, V., Venot, O., Hersant, F., & Selsis, F. (2014). Pseudo 2D chemical model of hot-Jupiter atmospheres: Application to HD 209458b and HD 189733b. *Astronomy & Astrophysics*, *564*, Article A73, A73.

Albrecht, S., Winn, J. N., Butler, R. P., Crane, J. D., Shectman, S. A., Thompson, I. B., Hirano, T., & Wittenmyer, R. A. (2012). A high stellar obliquity in the WASP-7 exoplanetary system. *The Astrophysical Journal*, *744*, 189.

Allard, F., Homeier, D., & Freytag, B. (2012). Models of very-low-mass stars, brown dwarfs and exoplanets. *Philosophical Transactions of the Royal Society of London Series A*, *370*(1968), 2765–2777.

Allen, M., Yung, Y. L., & Waters, J. W. (1981). Vertical transport and photochemistry in the terrestrial mesosphere and lower thermosphere /50-120 km/. *Journal of Geophysical Research*, *86*, 3617–3627.

Anderson, D. R., Collier Cameron, A., Delrez, L., Doyle, A. P., Faedi, F., Fumel, A., Gillon, M., Gómez Maqueo Chew, Y., Hellier, C., Jehin, E., Lendl, M., Maxted, P. F. L., Pepe, F., Pollacco, D., Queloz, D., Ségransan, D., Skillen, I., Smalley, B., Smith, A. M. S., . . . West, R. G. (2014). Three newly discovered sub-Jupiter-mass planets: WASP-69b and WASP-84b transit active K dwarfs and WASP-70Ab transits the evolved primary of a G4+K3 binary. *Monthly Notices of the Royal Astronomical Society*, *445*(2), 1114–1129.

Andrews, S. M., Rosenfeld, K. A., Kraus, A. L., & Wilner, D. J. (2013). The Mass Dependence between Protoplanetary Disks and their Stellar Hosts. *The Astrophysical Journal*, *771*(2), Article 129, 129.

Andrews, S. M., Wilner, D. J., Espaillat, C., Hughes, A. M., Dullemond, C. P., McClure, M. K., Qi, C., & Brown, J. M. (2011). Resolved Images of Large Cavities in Protoplanetary Transition Disks. *The Astrophysical Journal*, *732*(1), Article 42, 42.

Andrews, S. M., Huang, J., Pérez, L. M., Isella, A., Dullemond, C. P., Kurtovic, N. T., Guzmán, V. V., Carpenter, J. M., Wilner, D. J., Zhang, S., Zhu, Z., Birnstiel, T., Bai, X.-N., Benisty, M., Hughes, A. M., Öberg, K. I., & Ricci, L. (2018). The Disk Substructures at High Angular Resolution Project (DSHARP). I. Motivation, Sample, Calibration, and Overview. *The Astrophysical Journal*, *869*(2), Article L41, L41.

Asensio-Torres, R., Henning, T., Cantalloube, F., Pinilla, P., Mesa, D., Garufi, A., Jorquera, S., Gratton, R., Chauvin, G., Szulágyi, J., van Boekel, R., Dong, R., Marleau, G. .-., Benisty, M., Villenave, M., Bergez-Casalou, C., Desgrange, C., Janson, M., Keppler, M., . . . Ramos, J. (2021). Perturbers: SPHERE detection limits to planetary-mass companions in protoplanetary disks. *Astronomy & Astrophysics*, *652*, Article A101, A101.

Bakos, G. Á., Shporer, A., Pál, A., Torres, G., Kovács, G., Latham, D. W., Mazeh, T., Ofir, A., Noyes, R. W., Sasselov, D. D., Bouchy, F., Pont, F., Queloz, D., Udry, S., Esquerdo, G., Sipőcz, B., Kovács, G., Stefanik, R., Lázár, J., . . . Sári, P. (2007). HAT-P-5b: A Jupiter-like Hot Jupiter Transiting a Bright Star. *Astrophysical Journal Letters*, *671*(2), L173–L176.

Bakos, G. Á., Hartman, J., Torres, G., Latham, D. W., Kovcs, G., Noyes, R. W., Fischer, D. A., Johnson, J. A., Marcy, G. W., Howard, A. W., Kipping, D., Esquerdo, G. A., Shporer, A., Béky, B., Buchhave, L. A., Perumpilly, G., Everett, M., Sasselov, D. D., Stefanik, R. P., . . . Sári, P. (2011). HAT-P-20b-HAT-P-23b: Four massive transiting extrasolar planets. *The Astrophysical Journal*, *742*(2).

Baraffe, I., Chabrier, G., Barman, T. S., Allard, F., & Hauschildt, P. H. (2003). Evolutionary models for cool brown dwarfs and extrasolar giant planets. The case of HD 209458. *Astronomy & Astrophysics*, *402*, 701–712.

Barstow, J. K., Aigrain, S., Irwin, P. G. J., & Sing, D. K. (2017). A consistent retrieval analysis of 10 Hot Jupiters observed in transmission. *The Astrophysical Journal*, *834*(1), 50.

Baskin, N. J., Knutson, H. A., Burrows, A., Fortney, J. J., Lewis, N. K., Agol, E., Charbonneau, D., Cowan, N. B., Deming, D., Desert, J. M., Langton, J., Laughlin, G., & Showman, A. P. (2013). Secondary eclipse photometry of the exoplanet Wasp-5b with warm spitzer. *The Astrophysical Journal*, *773*(2), 124.

Baxter, C., Désert, J. M., Parmentier, V., Line, M., Fortney, J., Arcangeli, J., Bean, J. L., Todorov, K. O., & Mansfield, M. (2020). A transition between the hot and the ultra-hot Jupiter atmospheres. *Astronomy & Astrophysics*, *639*, A36.

Bean, J. L., Stevenson, K. B., Batalha, N. M., Berta-Thompson, Z., Kreidberg, L., Crouzet, N., Benneke, B., Line, M. R., Sing, D. K., Wakeford, H. R., Knutson, H. A., Kempton, E. M. .-., Désert, J.-M., Crossfield, I., Batalha, N. E., de Wit, J., Parmentier, V., Harrington, J., Moses, J. I., . . . Zingales, T. (2018). The Transiting Exoplanet Community Early Release Science Program for JWST. *Publications of the Astronomical Society of the Pacific*, *130*(993), 114402.

Beerer, I. M., Knutson, H. A., Burrows, A., Fortney, J. J., Agol, E., Charbonneau, D., Cowan, N. B., Deming, D., Desert, J. M., Langton, J., Laughlin, G., Lewis, N. K., & Showman, A. P. (2011). Secondary eclipse photometry of WASP-4b with warm spitzer. *The Astrophysical Journal*, *727*(1), 23.

Benisty, M., Juhász, A., Facchini, S., Pinilla, P., de Boer, J., Pérez, L. M., Keppler, M., Muro-Arena, G., Villenave, M., Andrews, S., Dominik, C., Dullemond, C. P., Gallenne, A., Garufi, A., Ginski, C., & Isella, A. (2018). Shadows and asymmetries in the T Tauri disk HD 143006: evidence for a misaligned inner disk. *Astronomy & Astrophysics*, *619*, Article A171, A171.

Benisty, M., Bae, J., Facchini, S., Keppler, M., Teague, R., Isella, A., Kurtovic, N. T., Pérez, L. M., Sierra, A., Andrews, S. M., Carpenter, J., Czekala, I., Dominik, C., Henning, T., Menard, F., Pinilla, P., & Zurlo, A. (2021). A Circumplanetary Disk around PDS70c. *The Astrophysical Journal Letters*, *916*(1), Article L2, L2.

Benneke, B., & Seager, S. (2012). Atmospheric retrieval for super-earths: Uniquely constraining the atmospheric composition with transmission spectroscopy. *The Astrophysical Journal*, *753*(2).

Benneke, B., Knutson, H. A., Lothringer, J., Crossfield, I. J. M., Moses, J. I., Morley, C., Kreidberg, L., Fulton, B. J., Dragomir, D., Howard, A. W., Wong, I., Désert, J.-M., McCullough, P. R., Kempton, E. M. .-., Fortney, J., Gilliland, R., Deming, D., & Kammer, J. (2019). A sub-Neptune exoplanet with a low-metallicity methane-depleted atmosphere and Mie-scattering clouds. *Nature Astronomy*, 377.

Biddle, L. I., Pearson, K. A., Crossfield, I. J., Fulton, B. J., Ciceri, S., Eastman, J., Barman, T., Mann, A. W., Henry, G. W., Howard, A. W., Williamson, M. H., Sinukoff, E., Dragomir, D., Vican, L., Mancini, L., Southworth, J., Greenberg, A., Turner, J. D., Thompson, R., . . . Webber, M. W. (2014). Warm ice giant GJ 3470b - II. Revised planetary and stellar parameters from optical to near-infrared transit photometry. *Monthly Notices of the Royal Astronomical Society*, *443*(2), 1810–1820.

Bodenheimer, P., Lin, D. N. C., & Mardling, R. A. (2001). On the Tidal Inflation of Short-Period Extrasolar Planets. *The Astrophysical Journal*, *548*(1), 466–472.

Boehler, Y., Ricci, L., Weaver, E., Isella, A., Benisty, M., Carpenter, J., Grady, C., Shen, B.-T., Tang, Y.-W., & Perez, L. (2018). The Complex Morphology of the Young Disk MWC 758: Spirals and Dust Clumps around a Large Cavity. *The Astrophysical Journal*, *853*(2), Article 162, 162.

Bonavita, M. (2020). Exo-DMC: Exoplanet Detection Map Calculator.

Bond, C. Z., Cetre, S., Lilley, S., Wizinowich, P., Mawet, D., Chun, M., Wetherell, E., Jacobson, S., Lockhart, C., Warmbier, E., Ragland, S., Alvarez, C., Guyon, O., Goebel, S., Delorme, J.-R., Jovanovic, N., Hall, D. N., Wallace, J. K., Taheri, M., . . . Chambouleyron, V. (2020). Adaptive optics with an infrared pyramid wavefront sensor at Keck. *Journal of Astronomical Telescopes, Instruments, and Systems*, *6*, Article 039003, 039003.

Bonomo, A. S., Desidera, S., Benatti, S., Borsa, F., Crespi, S., Damasso, M., Lanza, A. F., Sozzetti, A., Lodato, G., Marzari, F., Boccato, C., Claudi, R. U., Cosentino, R., Covino, E., Gratton, R., Maggio, A., Micela, G., Molinari, E., Pagano, I., . . . Scandariato, G. (2017). The GAPS Programme with HARPS-N at TNG. *Astronomy & Astrophysics*, *602*, A107.

Bordwell, B., Brown, B. P., & Oishi, J. S. (2018). Convective dynamics and disequilibrium chemistry in the atmospheres of giant planets and brown dwarfs. *The Astrophysical Journal*, *854*(1), 8.

Boss, A. P. (1997). Giant planet formation by gravitational instability. *Science*, *276*, 1836–1839.

Boss, A. P. (1998). Evolution of the Solar Nebula. IV. Giant Gaseous Protoplanet Formation. *The Astrophysical Journal*, *503*(2), 923–937.

Bowens, R., Meyer, M. R., Delacroix, C., Absil, O., van Boekel, R., Quanz, S. P., Shinde, M., Kenworthy, M., Carlomagno, B., Orban de Xivry, G., Cantalloube, F., & Pathak, P. (2021). Exoplanets with ELT-METIS. I. Estimating the direct imaging exoplanet yield around stars within 6.5 parsecs. *Astronomy & Astrophysics*, *653*, Article A8, A8.

Brogi, M., Line, M., Bean, J., Désert, J.-M., & Schwarz, H. (2017). A Framework to Combine Low- and High-resolution Spectroscopy for the Atmospheres of Transiting Exoplanets. *Astrophysical Journal Letters*, *839*(1), L2.

Burrows, A., Budaj, J., & Hubeny, I. (2008). Theoretical Spectra and Light Curves of Close-in Extrasolar Giant Planets and Comparison with Data. *The Astrophysical Journal*, *678*(2), 1436–1457.

Burrows, A., Sudarsky, D., & Hubeny, I. (2006). Theory for the Secondary Eclipse Fluxes, Spectra, Atmospheres, and Light Curves of Transiting Extrasolar Giant Planets. *The Astrophysical Journal*, *650*(2), 1140–1149.

Burrows, A., Marley, M., Hubbard, W. B., Lunine, J. I., Guillot, T., Saumon, D., Freedman, R., Sudarsky, D., & Sharp, C. (1997). A Nongray Theory of Extrasolar Giant Planets and Brown Dwarfs. *The Astrophysical Journal*, *491*(2), 856–875.

Canovas, H., Hardy, A., Zurlo, A., Wahhaj, Z., Schreiber, M. R., Vigan, A., Villaver, E., Olofsson, J., Meeus, G., Ménard, F., Caceres, C., Cieza, L. A., & Garufi, A. (2017). Constraining the mass of the planet(s) sculpting a disk cavity. The intriguing case of 2MASS J16042165-2130284. *Astronomy & Astrophysics*, *598*, Article A43, A43.

Carpenter, J. M., Ricci, L., & Isella, A. (2014). An ALMA Continuum Survey of Circumstellar Disks in the Upper Scorpius OB Association. *The Astrophysical Journal*, *787*(1), Article 42, 42.

Carrasco-González, C., Sierra, A., Flock, M., Zhu, Z., Henning, T., Chandler, C., Galván-Madrid, R., Macías, E., Anglada, G., Linz, H., Osorio, M., Rodríguez, L. F., Testi, L., Torrelles, J. M., Pérez, L., & Liu, Y. (2019). The Radial Distribution of Dust Particles in the HL Tau Disk from ALMA and VLA Observations. *The Astrophysical Journal*, *883*(1), Article 71, 71.

Casasayas-Barris, N., Palle, E., Nowak, G., Yan, F., Nortmann, L., & Murgas, F. (2017). Detection of sodium in the atmosphere of WASP-69b. *Astronomy & Astrophysics*, *608*, Article A135, A135.

Charbonneau, D., Allen, L. E., Megeath, S. T., Torres, G., Alonso, R., Brown, T. M., Gilliland, R. L., Latham, D. W., Mandushev, G., O'Donovan, F. T., & Sozzetti, A. (2005). Detection of Thermal Emission from an Extrasolar Planet. *The Astrophysical Journal*, *626*, 523.

Charbonneau, D., Knutson, H. A., Barman, T., Allen, L. E., Mayor, M., Megeath, S. T., Queloz, D., & Udry, S. (2008). The Broadband Infrared Emission Spectrum of the Exoplanet HD 189733b. *The Astrophysical Journal*, *686*(2), 1341–1348.

Chen, G., Pallé, E., Wellbanks, L., Prieto-Arranz, J., Madhusudhan, N., Gandhi, S., Casasayas-Barris, N., Murgas, F., Nortmann, L., Crouzet, N., Parviainen, H., & Gandolfi, D. (2018). The GTC exoplanet transit spectroscopy survey. *Astronomy & Astrophysics*, *616*, A145.

Choi, J., Dotter, A., Conroy, C., Cantiello, M., Paxton, B., & Johnson, B. D. (2016). Mesa Isochrones and Stellar Tracks (MIST). I. Solar-scaled Models. *The Astrophysical Journal*, *823*(2), Article 102, 102.

Cieza, L. A., González-Ruilova, C., Hales, A. S., Pinilla, P., Ruíz-Rodríguez, D., Zurlo, A., Casassus, S., Pérez, S., Cánovas, H., Arce-Tord, C., Flock, M., Kurtovic, N., Marino, S., Nogueira, P. H., Perez, L., Price, D. J., Principe, D. A., & Williams, J. P. (2021). The Ophiuchus DIsc Survey Employing ALMA (ODISEA) - III. The evolution of substructures in massive discs at 3-5 au resolution. *Monthly Notices of the Royal Astronomical Society*, *501*(2), 2934–2953.

Cooper, C. S., & Showman, A. P. (2005). Dynamic Meteorology at the Photosphere of HD 209458b. *The Astrophysical Journal*, (1), 45–48.

Cowan, N. B., & Agol, E. (2011). A model for thermal phase variations of circular and eccentric exoplanets. *The Astrophysical Journal*, *726*(2), 82.

Crouzet, N., McCullough, P. R., Deming, D., & Madhusudhan, N. (2014). Water vapor in the spectrum of the extrasolar planet HD 189733b. II. the eclipse. *The Astrophysical Journal*, *795*(2).

Cubillos, P., Harrington, J., Madhusudhan, N., Stevenson, K. B., Hardy, R. A., Blecic, J., Anderson, D. R., Hardin, M., & Campo, C. J. (2013). WASP-8b: Characterization of a cool and eccentric exoplanet with spitzer. *The Astrophysical Journal*, *768*(1), 42.

Cubillos, P., Harrington, J., Madhusudhan, N., Foster, A. S., Lust, N. B., Hardy, R. A., & Bowman, M. O. (2014). A spitzer five-band analysis of the jupiter-sized planet TrES-1. *The Astrophysical Journal*, *797*(1), 42.

Currie, T., Belikov, R., Guyon, O., Kasdin, N. J., Marois, C., Marley, M. S., Cahoy, K., Mawet, D., McElwain, M., Bendek, E., Kuchner, M. J., & Meyer, M. R. (2019). The Critical Strategic Importance of Adaptive Optics-Assisted Ground-Based Telescopes for the Success of Future NASA Exoplanet Direct Imaging Missions. *Bulletin of the American Astronomical Society*, *51*(3), Article 154, 154.

Delorme, J.-R., Jovanovic, N., Echeverri, D., Mawet, D., Kent Wallace, J., Bartos, R. D., Cetre, S., Wizinowich, P., Ragland, S., Lilley, S., Wetherell, E., Doppmann, G., Wang, J. J., Morris, E. C., Ruffio, J.-B., Martin, E. C., Fitzgerald, M. P., Ruane, G., Schofield, T., . . . Skemer, A. J. (2021). Keck Planet Imager and Characterizer: A dedicated single-mode fiber injection unit for high-resolution exoplanet spectroscopy. *Journal of Astronomical Telescopes, Instruments, and Systems*, *7*, Article 035006, 035006.

Deming, D., Knutson, H., Agol, E., Desert, J. M., Burrows, A., Fortney, J. J., Charbonneau, D., Cowan, N. B., Laughlin, G., Langton, J., Showman, A. P., & Lewis, N. K. (2011). Warm spitzer photometry of the transiting exoplanets CoRoT-1 and CoRoT-2 at secondary eclipse. *The Astrophysical Journal*, *726*(2), 95.

Deming, D., Knutson, H., Kammer, J., Fulton, B. J., Ingalls, J., Carey, S., Burrows, A., Fortney, J. J., Todorov, K., Agol, E., Cowan, N., Desert, J. M., Fraine, J., Langton, J., Morley, C., & Showman, A. P. (2015). Spitzer secondary eclipses of the dense, modestly-irradiated, giant exoplanet HAT-P-20b using pixel-level decorrelation. *The Astrophysical Journal*, *805*, 132.

Demory, B. O., Seager, S., Madhusudhan, N., Kjeldsen, H., Christensen-Dalsgaard, J., Gillon, M., Rowe, J. F., Welsh, W. F., Adams, E. R., Dupree, A., McCarthy, D., Kulesa, C., Borucki, W. J., & Koch, D. G. (2011). The high albedo of the hot Jupiter Kepler-7b. *Astrophysical Journal Letters*, *735*(1), L12.

Demory, B. O., De Wit, J., Lewis, N., Fortney, J., Zsom, A., Seager, S., Knutson, H., Heng, K., Madhusudhan, N., Gillon, M., Barclay, T., Desert, J. M., Parmentier, V., & Cowan, N. B. (2013). Inference of inhomogeneous clouds in an exoplanet atmosphere. *Astrophysical Journal Letters*, *776*(2), L25.

Désert, J. M., Charbonneau, D., Demory, B. O., Ballard, S., Carter, J. A., Fortney, J. J., Cochran, W. D., Endl, M., Quinn, S. N., Isaacson, H. T., Fressin, F., Buchhave, L. A., Latham, D. W., Knutson, H. A., Bryson, S. T., Torres, G., Rowe, J. F., Batalha, N. M., Borucki, W. J., . . . Winn, J. N. (2011). The hot-Jupiter Kepler-17b: Discovery, obliquity from stroboscopic starspots, and atmospheric characterization. *Astrophysical Journal Supplement Series*, *197*(1), 14.

Désert, J. M., Charbonneau, D., Fortney, J. J., Madhusudhan, N., Knutson, H. A., Fressin, F., Deming, D., Borucki, W. J., Brown, T. M., Caldwell, D., Ford, E. B., Gilliland, R. L., Latham, D. W., Marcy, G. W., & Seager, S. (2011). The atmospheres of the hot-Jupiters Kepler-5b and Kepler-6b observed during occultations with Warm-Spitzer and Kepler. *Astrophysical Journal Supplement Series*, *197*(1), 11.

Dong, R., & Fung, J. (2017). What is the Mass of a Gap-opening Planet? *The Astrophysical Journal*, *835*(2), Article 146, 146.

Dong, R., Liu, S.-y., Eisner, J., Andrews, S., Fung, J., Zhu, Z., Chiang, E., Hashimoto, J., Liu, H. B., Casassus, S., Esposito, T., Hasegawa, Y., Muto, T., Pavlyuchenkov, Y., Wilner, D., Akiyama, E., Tamura, M., & Wisniewski, J. (2018). The Eccentric Cavity, Triple Rings, Two-armed Spirals, and Double Clumps of the MWC 758 Disk. *The Astrophysical Journal*, *860*(2), Article 124, 124.

Drummond, B., Mayne, N. J., Baraffe, I., Tremblin, P., Manners, J., Amundsen, D. S., Goyal, J., & Acreman, D. (2018). The effect of metallicity on the atmospheres of exoplanets with fully coupled 3D hydrodynamics, equilibrium chemistry, and radiative transfer. *Astronomy & Astrophysics*, *612*, A105.

Espinoza, N., Fortney, J., Miguel, Y., Thorngren, D., & Murray-Clay, R. (2017). Metal enrichment leads to low atmospheric C/O ratios in transiting giant exoplanets. *Astrophysical Journal Letters*, *838*(1), L9.

Evans, T. M., Aigrain, S., Gibson, N., Barstow, J. K., Amundsen, D. S., Tremblin, P., & Mourier, P. (2015). A uniform analysis of HD 209458b Spitzer/IRAC light curves with Gaussian process models. *Monthly Notices of the Royal Astronomical Society*, *451*(1), 680–694.

Evans, T. M., Sing, D. K., Kataria, T., Goyal, J., Nikolov, N., Wakeford, H. R., Deming, D., Marley, M. S., Amundsen, D. S., Ballester, G. E., Barstow, J. K., Ben-Jaffel, L., Bourrier, V., Buchhave, L. A., Cohen, O., Ehrenreich, D., García Muñoz, A., Henry, G. W., Knutson, H., . . . Lupu, R. (2017). An ultrahot gas-giant exoplanet with a stratosphere. *Nature*, *548*(7665), 58–61.

Fazio, G. G., Hora, J. L., Allen, L. E., Ashby, M. L. N., Barmby, P., Deutsch, L. K., Huang, J.-S., Kleiner, S., Marengo, M., Megeath, S. T., Melnick, G. J., Pahre, M. A., Patten, B. M., Polizotti, J., Smith, H. A., Taylor, R. S., Wang, Z., Willner, S. P., Hoffmann, W. F., . . . Cohen, M. (2004). The Infrared Array Camera (IRAC) for the Spitzer Space Telescope. *Astrophysical Journal Supplement Series*, *154*(1), 10–17.

Fedele, D., Carney, M., Hogerheijde, M. R., Walsh, C., Miotello, A., Klaassen, P., Bruderer, S., Henning, T., & van Dishoeck, E. F. (2017). ALMA unveils rings and gaps in the protoplanetary system HD 169142: signatures of two giant protoplanets. *Astronomy & Astrophysics*, *600*, Article A72, A72.

Fischer, D. A., & Valenti, J. (2005). The Planet-Metallicity Correlation. *The Astrophysical Journal*, *622*(2), 1102–1117.

Flaherty, K. M., Hughes, A. M., Teague, R., Simon, J. B., Andrews, S. M., & Wilner, D. J. (2018). Turbulence in the TW Hya Disk. *The Astrophysical Journal*, *856*(2), Article 117, 117.

Flasseur, O., Thé, S., Denis, L., Thiébaut, É., & Langlois, M. (2021). REXPACO: An algorithm for high contrast reconstruction of the circumstellar environment by angular differential imaging. *Astronomy & Astrophysics*, *651*, Article A62, A62.

Foreman-Mackey, D., Hogg, D. W., Lang, D., & Goodman, J. (2013). emcee: The MCMC Hammer. *Publications of the Astronomical Society of the Pacific*, *125*, 306–312.

Foreman-Mackey, D., Hogg, D. W., Lang, D., & Goodman, J. (2019). emcee : The MCMC Hammer. *JOSS*, *4*(43), 1864.

Fortney, J. J. (2005). The effect of condensates on the characterization of transiting planet atmospheres with transmission spectroscopy. *Monthly Notices of the Royal Astronomical Society*, *364*(2), 649–653.

Fortney, J. J., Lodders, K., Marley, M. S., & Freedman, R. S. (2008). A Unified Theory for the Atmospheres of the Hot and Very Hot Jupiters: Two Classes of Irradiated Atmospheres. *The Astrophysical Journal*, *678*, 1419–1435.

Fortney, J. J., Demory, B. O., Désert, J. M., Rowe, J., Marcy, G. W., Isaacson, H., Buchhave, L. A., Ciardi, D., Gautier, T. N., Batalha, N. M., Caldwell, D. A., Bryson, S. T., Nutzman, P., Jenkins, J. M., Howard, A., Charbonneau, D., Knutson, H. A., Howell, S. B., Everett, M., . . . Geary, J. C. (2011). Discovery and atmospheric characterization of giant planet Kepler-12b: An inflated radius outlier. *Astrophysical Journal Supplement Series*, *197*(1), 9.

Fraine, J., Deming, D., Benneke, B., Knutson, H., Jordán, A., Espinoza, N., Madhusudhan, N., Wilkins, A., & Todorov, K. (2014). Water vapour absorption in the clear atmosphere of a Neptune-sized exoplanet. *Nature*, *513*(7519), 526–529.

Freedman, R. S., Marley, M. S., & Lodders, K. (2008). Line and Mean Opacities for Ultracool Dwarfs and Extrasolar Planets. *Astrophysical Journal Supplement Series*, *174*(2), 504–513.

Freedman, R. S., Lustig-Yaeger, J., Fortney, J. J., Lupu, R. E., Marley, M. S., & Lodders, K. (2014). Gaseous mean opacities for giant planet and ultracool dwarf atmospheres over a range of metallicities and temperatures. *Astrophysical Journal Supplement Series*, *214*(2).

Fressin, F., Knutson, H. A., Charbonneau, D., O'Donovan, F. T., Burrows, A., Deming, D., Mandushev, G., & Spiegel, D. (2010). The broadband infrared emission spectrum of the exoplanet TrES-3. *The Astrophysical Journal*, *711*(1), 374–379.

Fulton, B. J., Howard, A. W., Winn, J. N., Albrecht, S., Marcy, G. W., Crepp, J. R., Bakos, G. A., Johnson, J. A., Hartman, J. D., Isaacson, H., Knutson, H. A., & Zhao, M. (2013). The stellar obliquity and the long-period planet in the hat-p-17 exoplanetary system. *The Astrophysical Journal*, *772*(2).

Galli, P. A. B., Loinard, L., Ortiz-Léon, G. N., Kounkel, M., Dzib, S. A., Mioduszewski, A. J., Rodríguez, L. F., Hartmann, L., Teixeira, R., Torres, R. M., Rivera, J. L., Boden, A. F., Evans II, N. J., Briceño, C., Tobin, J. J., & Heyer, M. (2018). The Gould's Belt Distances Survey (GOBELINS). IV. Distance, Depth, and Kinematics of the Taurus Star-forming Region. *The Astrophysical Journal*, *859*(1), 33.

Garhart, E., Deming, D., Mandell, A., Knutson, H. A., Wallack, N., Burrows, A., Fortney, J. J., Hood, C., Seay, C., Sing, D. K., Benneke, B., Fraine, J. D., Kataria, T., Lewis, N., Madhusudhan, N., Mccullough, P., & Stevenson, K. B. (2020). Statistical Characterization of Hot Jupiter Atmospheres Using Spitzer's Secondary Eclipses. *The Astronomical Journal*, *159*(4), 137.

Gillon, M., Anderson, D. R., Collier-Cameron, A., Doyle, A. P., Fumel, A., Hellier, C., Jehin, E., Lendl, M., Maxted, P. F. L., Montalbán, J., Pepe, F., Pollacco, D., Queloz, D., Ségransan, D., Smith, A. M. S., Smalley, B., Southworth, J., Triaud, A. H. M. J., Udry, S., & West, R. G. (2013). WASP-64 b and WASP-72 b: two new transiting highly irradiated giant planets. *Astronomy & Astrophysics*, *552*, A82.

Gomez Gonzalez, C. A., Wertz, O., Absil, O., Christiaens, V., Defrère, D., Mawet, D., Milli, J., Absil, P.-A., Van Droogenbroeck, M., Cantalloube, F., Hinz, P. M., Skemer, A. J., Karlsson, M., & Surdej, J. (2017). VIP: Vortex Image Processing Package for High-contrast Direct Imaging. *The Astronomical Journal*, *154*(1), Article 7, 7.

González-Ruilova, C., Cieza, L. A., Hales, A. S., Pérez, S., Zurlo, A., Arce-Tord, C., Casassus, S., Cánovas, H., Flock, M., Herczeg, G. J., Pinilla, P., Price, D. J., Principe, D. A., Ruíz-Rodríguez, D., & Williams, J. P. (2020). A Tale of Two Transition Disks: ALMA Long-baseline Observations of ISO-Oph 2 Reveal Two Closely Packed Nonaxisymmetric Rings and a ~2 au Cavity. *The Astrophysical Journal*, *902*(2), Article L33, L33.

Guidi, G., Ruane, G., Williams, J. P., Mawet, D., Testi, L., Zurlo, A., Absil, O., Bottom, M., Choquet, É., Christiaens, V., Femenía Castellá, B., Huby, E., Isella, A., Kastner, J., Meshkat, T., Reggiani, M., Riggs, A., Serabyn, E., & Wallack, N. (2018). High-contrast imaging of HD 163296 with the Keck/NIRC2 L'-band vortex coronograph. *Monthly Notices of the Royal Astronomical Society*, *479*(2), 1505–1513.

Guzmán-Díaz, J., Mendigutía, I., Montesinos, B., Oudmaijer, R. D., Vioque, M., Rodrigo, C., Solano, E., Meeus, G., & Marcos-Arenal, P. (2021). Homogeneous study of Herbig Ae/Be stars from spectral energy distributions and Gaia EDR3. *Astronomy & Astrophysics*, *650*, Article A182, A182.

Haffert, S. Y., Bohn, A. J., de Boer, J., Snellen, I. A. G., Brinchmann, J., Girard, J. H., Keller, C. U., & Bacon, R. (2019). Two accreting protoplanets around the young star PDS 70. *Nature Astronomy*, *3*, 749–754.

Hartman, J. D., Bakos, G. Á., Kipping, D. M., Torres, G., Kovács, G., Noyes, R. W., Latham, D. W., Howard, A. W., Fischer, D. A., Johnson, J. A., Marcy, G. W., Isaacson, H., Quinn, S. N., Buchhave, L. A., Béky, B., Sasselov, D. D., Stefanik, R. P., Esquerdo, G. A., Everett, M., . . . Sári, P. (2011). HAT-P-26b: A low-density Neptune-mass planet transiting a K star. *The Astrophysical Journal*, *728*(2).

Hartman, J. D., Bakos, G. Á., Sato, B., Torres, G., Noyes, R. W., Latham, D. W., Kovács, G., Fischer, D. A., Howard, A. W., Johnson, J. A., Marcy, G. W., Buchhave, L. A., Füresz, G., Perumpilly, G., Béky, B., Stefanik, R. P., Sasselov, D. D., Esquerdo, G. A., Everett, M., . . . Sári, P. (2011). HAT-P-18b and HAT-P-19b: Two low-density Saturn-mass planets transiting metal-rich K stars. *The Astrophysical Journal*, *726*(1).

Hartman, J. D., Bakos, G. Á., Torres, G., Kovcs, G., Noyes, R. W., Pál, A., Latham, D. W., Sipc'z, B., Fischer, D. A., Johnson, J. A., Marcy, G. W., Butler, R. P., Howard, A. W., Esquerdo, G. A., Sasselov, D. D., Kovács, G., Stefanik, R. P., Fernandez, J. M., Lázár, J., . . . Sári, P. (2009). HAT-P-12b: A low-density sub-saturn mass planet transiting a metal-poor K dwarf. *Astrophysical Journal*, *706*(1), 785–796.

Hellier, C., Anderson, D. R., Gillon, M., Lister, T. A., Maxted, P. F., Queloz, D., Smalley, B., Triaud, A. H., West, R. G., Wilson, D. M., Alsubai, K., Bentley, S. J., Cameron, A. C., Hebb, L., Horne, K., Irwin, J., Kane, S. R., Mayor, M., Pepe, F., . . . Todd, I. (2009). Wasp-7: A bright transiting-exoplanet system in the southern hemisphere. *The Astrophysical Journal*, *690*(1 PART 2), 89–91.

Heng, K., & Demory, B. O. (2013). Understanding trends associated with clouds in irradiated exoplanets. *The Astrophysical Journal*, *777*(2), 100.

Heng, K., & Marley, M. S. (2018). Atmospheres. *in Handbook of Exoplanets, ed. H. Deeg & J. Belmonte (Cham: Springer)*, 2137–2152.

Herczeg, G. J., & Hillenbrand, L. A. (2014). An Optical Spectroscopic Study of T Tauri Stars. I. Photospheric Properties. *The Astrophysical Journal*, *786*(2), Article 97, 97.

Howard, A. W., Bakos, G. Á., Hartman, J., Torres, G., Shporer, A., Mazeh, T., Kovács, G., Latham, D. W., Noyes, R. W., Fischer, D. A., Johnson, J. A., Marcy, G. W., Esquerdo, G. A., Béky, B., Butler, R. P., Sasselov, D. D., Stefanik, R. P., Perumpilly, G., Lázár, J., . . . Sári, P. (2012). HAT-P-17b,c: A transiting, eccentric, hot saturn and a long-period, cold Jupiter. *The Astrophysical Journal*, *749*(2).

Huang, J., Andrews, S. M., Dullemond, C. P., Öberg, K. I., Qi, C., Zhu, Z., Birnstiel, T., Carpenter, J. M., Isella, A., Macías, E., McClure, M. K., Pérez, L. M., Teague, R., Wilner, D. J., & Zhang, S. (2020). A Multifrequency ALMA

Characterization of Substructures in the GM Aur Protoplanetary Disk. *The Astrophysical Journal*, *891*(1), Article 48, 48.

Huby, E., Bottom, M., Femenia, B., Ngo, H., Mawet, D., Serabyn, E., & Absil, O. (2017). On-sky performance of the QACITS pointing control technique with the Keck/NIRC2 vortex coronagraph. *Astronomy & Astrophysics*, *600*, Article A46, A46.

Humphries, R. J., & Nayakshin, S. (2018). Changes in the metallicity of gas giant planets due to pebble accretion. *Monthly Notices of the Royal Astronomical Society*, *477*(1), 593–615.

Husser, T. .-., Wende-von Berg, S., Dreizler, S., Homeier, D., Reiners, A., Barman, T., & Hauschildt, P. H. (2013). A new extensive library of PHOENIX stellar atmospheres and synthetic spectra. *Astronomy & Astrophysics*, *553*, Article A6, A6.

Ingalls, J. G., Krick, J. E., Carey, S. J., Laine, S., Surace, J. A., Glaccum, W. J., Grillmair, C. C., & Lowrance, P. J. (2012). Intra-pixel gain variations and high-precision photometry with the Infrared Array Camera (IRAC). *Proc. SPIE*, *8442*(2), 84421Y.

Isella, A., Pérez, L. M., & Carpenter, J. M. (2012). On the Nature of the Transition Disk around LkCa 15. *The Astrophysical Journal*, *747*(2), Article 136, 136.

Isella, A., Guidi, G., Testi, L., Liu, S., Li, H., Li, S., Weaver, E., Boehler, Y., Carperter, J. M., De Gregorio-Monsalvo, I., Manara, C. F., Natta, A., Pérez, L. M., Ricci, L., Sargent, A., Tazzari, M., & Turner, N. (2016). Ringed Structures of the HD 163296 Protoplanetary Disk Revealed by ALMA. *Physical Review Letters*, *117*(25), Article 251101, 251101.

Johansen, A., & Lambrechts, M. (2017). Forming Planets via Pebble Accretion. *Annual Review of Earth and Planetary Sciences*, *45*(1), 359–387.

Johansen, A., Blum, J., Tanaka, H., Ormel, C., Bizzarro, M., & Rickman, H. (2014). The multifaceted planetesimal formation process. *Protostars and Planets VI*, 547.

Kammer, J. A., Knutson, H. A., Line, M. R., Fortney, J. J., Deming, D., Burrows, A., Cowan, N. B., Triaud, A. H., Agol, E., Desert, J. M., Fulton, B. J., Howard, A. W., Laughlin, G. P., Lewis, N. K., Morley, C. V., Moses, J. I., Showman, A. P., & Todorov, K. O. (2015). Spitzer Secondary Eclipse Observations of Five Cool Gas Giant Planets and Empirical Trends in Cool Planet Emission Spectra. *The Astrophysical Journal*, *810*(2), 118.

Keppler, M., Benisty, M., Müller, A., Henning, T., van Boekel, R., Cantalloube, F., Ginski, C., van Holstein, R. G., Maire, A. .-., Pohl, A., Samland, M., Avenhaus, H., Baudino, J. .-., Boccaletti, A., de Boer, J., Bonnefoy, M., Chauvin, G., Desidera, S., Langlois, M., . . . Weber, L. (2018). Discovery of a planetary-mass companion within the gap of the transition disk around PDS 70. *Astronomy & Astrophysics*, *617*, Article A44, A44.

Keppler, M., Teague, R., Bae, J., Benisty, M., Henning, T., van Boekel, R., Chapillon, E., Pinilla, P., Williams, J. P., Bertrang, G. H. .-., Facchini, S., Flock, M., Ginski, C., Juhasz, A., Klahr, H., Liu, Y., Müller, A., Pérez, L. M., Pohl, A., . . . Semenov, D. (2019). Highly structured disk around the planet host PDS 70 revealed by high-angular resolution observations with ALMA. *Astronomy & Astrophysics*, *625*, Article A118, A118.

Kim, K. H., Watson, D. M., Manoj, P., Forrest, W. J., Najita, J., Furlan, E., Sargent, B., Espaillat, C., Muzerolle, J., Megeath, S. T., Calvet, N., Green, J. D., & Arnold, L. (2013). Transitional Disks and Their Origins: An Infrared Spectroscopic Survey of Orion A. *The Astrophysical Journal*, *769*(2), Article 149, 149.

Kirk, J., Wheatley, P. J., Louden, T., Doyle, A. P., Skillen, I., McCormac, J., Irwin, P. G. J., & Karjalainen, R. (2017). Rayleigh scattering in the transmission spectrum of HAT-P-18b. *Monthly Notices of the Royal Astronomical Society*, *3916*(2018), 3907–3916.

Kluska, J., Kraus, S., Davies, C. L., Harries, T., Willson, M., Monnier, J. D., Aarnio, A., Baron, F., Millan-Gabet, R., Ten Brummelaar, T., Che, X., Hinkley, S., Preibisch, T., Sturmann, J., Sturmann, L., & Touhami, Y. (2018). A Multi-instrument and Multi-wavelength High Angular Resolution Study of MWC 614: Quantum Heated Particles Inside the Disk Cavity. *The Astrophysical Journal*, *855*(1), Article 44, 44.

Knutson, H. A., Benneke, B., Deming, D., & Homeier, D. (2014). A featureless transmission spectrum for the Neptune-mass exoplanet GJ 436b. *Nature*, *505*(7481), 66–68.

Knutson, H. A., Charbonneau, D., Allen, L. E., Burrows, A., & Megeath, S. T. (2008). The 3.6–8.0 μm Broadband Emission Spectrum of HD 209458b: Evidence for an Atmospheric Temperature Inversion. *The Astrophysical Journal*, *673*(1), 526–531.

Knutson, H. A., Charbonneau, D., Burrows, A., O'Donovan, F. T., & Mandushev, G. (2009). Detection of a temperature inversion in the broadband infrared emission spectrum of TrES-4. *The Astrophysical Journal*, *691*(1), 866–874.

Knutson, H. A., Fulton, B. J., Montet, B. T., Kao, M., Ngo, H., Howard, A. W., Crepp, J. R., Hinkley, S., Bakos, G. Á., Batygin, K., Johnson, J. A., Morton, T. D., & Muirhead, P. S. (2014). Friends of hot jupiters. I. A radial velocity search for massive, long-period companions to close-in gas giant planets. *The Astrophysical Journal*, *785*(2).

Knutson, H. A., Lewis, N., Fortney, J. J., Burrows, A., Showman, A. P., Cowan, N. B., Agol, E., Aigrain, S., Charbonneau, D., Deming, D., Désert, J. M., Henry, G. W., Langton, J., & Laughlin, G. (2012). 3.6 and 4.5 μm phase curves and evidence for non-equilibrium chemistry in the atmosphere of extrasolar planet HD 189733b. *The Astrophysical Journal*, *754*, 22.

Komacek, T. D., & Showman, A. P. (2016). Atmospheric Circulation of Hot Jupiters: Dayside–Nightside Temperature Differences. *The Astrophysical Journal*, *821*(1), 16.

Konishi, M., Grady, C. A., Schneider, G., Shibai, H., McElwain, M. W., Nesvold, E. R., Kuchner, M. J., Carson, J., Debes, J. H., Gaspar, A., Henning, T. K., Hines, D. C., Hinz, P. M., Jang-Condell, H., Moro-Martín, A., Perrin, M., Rodigas, T. J., Serabyn, E., Silverstone, M. D., . . . Wisniewski, J. P. (2016). Discovery of an Inner Disk Component around HD 141569 A. *The Astrophysical Journal*, *818*(2), Article L23, L23.

Kovács, G., Bakos, G. Á., Hartman, J. D., Torres, G., Noyes, R. W., Latham, D. W., Howard, A. W., Fischer, D. A., Johnson, J. A., Marcy, G. W., Isaacson, H., Sasselov, D. D., Stefanik, R. P., Esquerdo, G. A., Fernandez, J. M., Lázár, B. B. J., Papp, I., & Sári, P. (2010). HAT-P-15b: A 10.9 day extrasolar planet transiting a solar-type star. *The Astrophysical Journal*, *724*(2), 866–877.

Kraus, S., Ireland, M. J., Sitko, M. L., Monnier, J. D., Calvet, N., Espaillat, C., Grady, C. A., Harries, T. J., Hönig, S. F., Russell, R. W., Swearingen, J. R., Werren, C., & Wilner, D. J. (2013). Resolving the Gap and AU-scale Asymmetries in the Pre-transitional Disk of V1247 Orionis. *The Astrophysical Journal*, *768*(1), Article 80, 80.

Kraus, S., Kreplin, A., Fukugawa, M., Muto, T., Sitko, M. L., Young, A. K., Bate, M. R., Grady, C., Harries, T. T., Monnier, J. D., Willson, M., & Wisniewski, J. (2017). Dust-trapping Vortices and a Potentially Planet-triggered Spiral Wake in the Pre-transitional Disk of V1247 Orionis. *The Astrophysical Journal*, *848*(1), Article L11, L11.

Kreidberg, L. (2015). batman: BAsic Transit Model cAlculatioN in Python. *Publications of the Astronomical Society of the Pacific*, *127*, 1161–1165.

Kreidberg, L., Line, M. R., Parmentier, V., Stevenson, K. B., Louden, T., Bonnefoy, M., Faherty, J. K., Henry, G. W., Williamson, M. H., Stassun, K., Beatty, T. G., Bean, J. L., Fortney, J. J., Showman, A. P., Désert, J.-M., & Arcangeli, J. (2018). Global Climate and Atmospheric Composition of the Ultra-hot Jupiter WASP-103b from HST and Spitzer Phase Curve Observations. *The Astronomical Journal*, *156*(1), 17.

Kwon, W., Looney, L. W., Mundy, L. G., & Welch, W. J. (2015). Resolving Protoplanetary Disks at Millimeter Wavelengths with CARMA. *The Astrophysical Journal*, *808*(1), Article 102, 102.

Lam, K. W. F., Faedi, F., Brown, D. J. A., Anderson, D. R., Delrez, L., Gillon, M., Hébrard, G., Lendl, M., Mancini, L., Southworth, J., Smalley, B., Triaud, A. H. M., Turner, O. D., Hay, K. L., Armstrong, D. J., Barros, S. C. C., Bonomo, A. S., Bouchy, F., Boumis, P., . . . Wheatley, P. J. (2017). From dense hot Jupiter to low-density Neptune: The discovery of WASP-127b, WASP-136b, and WASP-138b. *Astronomy & Astrophysics*, *599*, A3.

Lambrechts, M., & Johansen, A. (2012). Rapid growth of gas-giant cores by pebble accretion. *Astronomy & Astrophysics*, *544*, Article A32, A32.

Lanotte, A. A., Gillon, M., Demory, B.-O., Fortney, J. J., Astudillo, N., Bonfils, X., Magain, P., Delfosse, X., Forveille, T., Lovis, C., Mayor, M., Neves, V., Pepe, F., Queloz, D., Santos, N., & Udry, S. (2014). A global analysis of Spitzer and new HARPS data confirms the loneliness and metal-richness of GJ 436 b. *Astronomy & Astrophysics*, *572*, A73.

Laughlin, G., Crismani, M., & Adams, F. C. (2011). On the anomalous radii of the transiting extrasolar planets. *Astrophysical Journal Letters*, *729*(1 PART II), 3–7.

Launhardt, R., Henning, T., Quirrenbach, A., Ségransan, D., Avenhaus, H., van Boekel, R., Brems, S. S., Cheetham, A. C., Cugno, G., Girard, J., Godoy, N., Kennedy, G. M., Maire, A. .-., Metchev, S., Müller, A., Musso Barcucci, A., Olofsson, J., Pepe, F., Quanz, S. P., . . . Samland, M. (2020). ISPY-NACO Imaging Survey for Planets around Young stars. Survey description and results from the first 2.5 years of observations. *Astronomy & Astrophysics*, *635*, Article A162, A162.

Lee, G., Dobbs-Dixon, I., Helling, C., Bognar, K., & Woitke, P. (2016). Dynamic mineral clouds on HD 189733b. *Astronomy & Astrophysics*, *594*, A48.

Lewis, N. K., Knutson, H. A., Showman, A. P., Cowan, N. B., Laughlin, G., Burrows, A., Deming, D., Crepp, J. R., Mighell, K. J., Agol, E., Bakos, G. Á., Charbonneau, D., Désert, J. M., Fischer, D. A., Fortney, J. J., Hartman, J. D., Hinkley, S., Howard, A. W., Johnson, J. A., . . . Marcy, G. W. (2013). Orbital phase variations of the eccentric giant planet HAT-P-2b. *The Astrophysical Journal*, *766*, 95.

Lindgren, S., & Heiter, U. (2017). Metallicity determination of M dwarfs Expanded parameter range in metallicity and effective temperature. *Astronomy & Astrophysics*, *604*.

Lines, S., Mayne, N. J., Boutle, I. A., Manners, J., Lee, G. K. H., Helling, C., Drummond, B., Amundsen, D. S., Goyal, J., Acreman, D. M., Tremblin, P., & Kerslake, M. (2018). Simulating the cloudy atmospheres of HD 209458 b and HD 189733 b with the 3D Met Office Unified Model. *Astronomy & Astrophysics*, *97*.

Liu, M. C. (2004). Substructure in the Circumstellar Disk Around the Young Star AU Microscopii. *Science*, *305*(5689), 1442–1444.

Liu, S.-F., Jin, S., Li, S., Isella, A., & Li, H. (2018). New Constraints on Turbulence and Embedded Planet Mass in the HD 163296 Disk from Planet-Disk Hydrodynamic Simulations. *The Astrophysical Journal*, *857*(2), Article 87, 87.

Lodato, G., Dipierro, G., Ragusa, E., Long, F., Herczeg, G. J., Pascucci, I., Pinilla, P., Manara, C. F., Tazzari, M., Liu, Y., Mulders, G. D., Harsono, D., Boehler, Y., Ménard, F., Johnstone, D., Salyk, C., van der Plas, G., Cabrit, S., Edwards, S., . . . Gully-Santiago, M. (2019). The newborn planet population emerging from ring-like structures in discs. *Monthly Notices of the Royal Astronomical Society*, *486*(1), 453–461.

Lodders, K., Palme, H., & Gail, H.-P. (2009). Abundances of the Elements in the Solar System. *Landolt Börnstein*, 712.

Lodders, K. (2003). Solar system abundances and condensation temperatures of the elements. *The Astrophysical Journal*, 1220–1247.

Long, F., Pinilla, P., Herczeg, G. J., Harsono, D., Dipierro, G., Pascucci, I., Hendler, N., Tazzari, M., Ragusa, E., Salyk, C., Edwards, S., Lodato, G., van de Plas, G., Johnstone, D., Liu, Y., Boehler, Y., Cabrit, S., Manara, C. F., Menard, F., . . . Gully-Santiago, M. (2018). Gaps and Rings in an ALMA Survey of Disks in the Taurus Star-forming Region. *The Astrophysical Journal*, *869*(1), 17.

Loomis, R. A., Öberg, K. I., Andrews, S. M., & MacGregor, M. A. (2017). A Multi-ringed, Modestly Inclined Protoplanetary Disk around AA Tau. *The Astrophysical Journal*, *840*(1), Article 23, 23.

Lothringer, J. D., Barman, T., & Koskinen, T. (2018). Extremely Irradiated Hot Jupiters: Non-oxide Inversions, H - Opacity, and Thermal Dissociation of Molecules. *The Astrophysical Journal*, *866*(1), 27.

Machalek, P., McCullough, P. R., Burke, C. J., Valenti, J. A., Burrows, A., & Hora, J. L. (2008). Thermal Emission of Exoplanet XO-1b. *The Astrophysical Journal*, *684*(2), 1427–1432.

Machalek, P., McCullough, P. R., Burrows, A., Burke, C. J., Hora, J. L., & Johns-Krull, C. M. (2009). Detection of Thermal Emission of XO-2b: Evidence for a Weak Temperature Inversion. *The Astrophysical Journal*, *701*(1), 514–520.

Machalek, P., Greene, T., McCullough, P. R., Burrows, A., Burke, C. J., Hora, J. L., Johns-Krull, C. M., & Deming, D. L. (2010). Thermal emission and tidal heating of the heavy and eccentric planet XO-3b. *The Astrophysical Journal*, *711*(1), 111–118.

Mamajek, E. E., & Bell, C. P. M. (2014). On the age of the β Pictoris moving group. *Monthly Notices of the Royal Astronomical Society*, *445*(3), 2169–2180.

Manara, C. F., Testi, L., Natta, A., & Alcalá, J. M. (2015). X-Shooter study of accretion in ρ-Ophiucus: Very low-mass stars and brown dwarfs. *Astronomy & Astrophysics*, *579*, Article A66, A66.

Mancini, L., Southworth, J., Ciceri, S., Calchi Novati, S., Dominik, M., Henning, T., Jørgensen, U. G., Korhonen, H., Nikolov, N., Alsubai, K. A., Bozza, V., Bramich, D. M., D'Ago, G., Figuera Jaimes, R., Galianni, P., Gu, S.-H., Harpsøe, K., Hinse, T. C., Hundertmark, M., . . . Wertz, O. (2014). Physical properties of the WASP-67 planetary system from multi-colour photometry. *Astronomy & Astrophysics*, *568*, A127.

Mandel, K., & Agol, E. (2002). Analytic Light Curves for Planetary Transit Searches. *The Astrophysical Journal*, *580*(2), L171–L175.

Marocco, F., Eisenhardt, P. R. M., Fowler, J. W., Kirkpatrick, J. D., Meisner, A. M., Schlafly, E. F., Stanford, S. A., Garcia, N., Caselden, D., Cushing, M. C., Cutri, R. M., Faherty, J. K., Gelino, C. R., Gonzalez, A. H., Jarrett, T. H., Koontz, R., Mainzer, A., Marchese, E. J., Mobasher, B., . . . Wright, E. L. (2021). The CatWISE2020 Catalog. *The Astrophysical Journal Supplement Series*, *253*(1), Article 8, 8.

Marois, C., Lafrenière, D., Doyon, R., Macintosh, B., & Nadeau, D. (2006). Angular Differential Imaging: A Powerful High-Contrast Imaging Technique. *The Astrophysical Journal*, *641*(1), 556–564.

Mawet, D., Milli, J., Wahhaj, Z., Pelat, D., Absil, O., Delacroix, C., Boccaletti, A., Kasper, M., Kenworthy, M., Marois, C., Mennesson, B., & Pueyo, L. (2014). Fundamental Limitations of High Contrast Imaging Set by Small Sample Statistics. *The Astrophysical Journal*, *792*(2), Article 97, 97.

Mawet, D., Choquet, É., Absil, O., Huby, E., Bottom, M., Serabyn, E., Femenia, B., Lebreton, J., Matthews, K., Gonzalez, C. A. G., Wertz, O., Carlomagno, B., Christiaens, V., Defrère, D., Delacroix, C., Forsberg, P., Habraken, S., Jolivet, A., Karlsson, M., . . . Catalan, E. V. (2016). Characterization of the inner disk around HD 141569 A from Keck/NIRC2 L-band vortex coronagraphy. *The Astronomical Journal*, *153*(1), 1–10.

Mayor, M., & Queloz, D. (1995). A Jupiter-mass companion to a solar-type star. *Nature*, *378*(6555), 355–359.

McCarthy, K., & White, R. J. (2012). The Sizes of the Nearest Young Stars. *The Astronomical Journal*, *143*(6), Article 134, 134.

Meeus, G., Montesinos, B., Mendigutía, I., Kamp, I., Thi, W. F., Eiroa, C., Grady, C. A., Mathews, G., Sandell, G., Martin-Zaıdi, C., Brittain, S., Dent, W. R. F., Howard, C., Ménard, F., Pinte, C., Roberge, A., Vandenbussche, B., & Williams, J. P. (2012). Observations of Herbig Ae/Be stars with Herschel/PACS. The atomic and molecular contents of their protoplanetary discs. *Astronomy & Astrophysics*, *544*, Article A78, A78.

Mendonça, J. M., Tsai, S.-M., Matej, M., Grimm, S. L., & Heng, K. (2018). Three-Dimensional Circulation Driving Chemical Disequilibrium in WASP-43b. *The Astrophysical Journal*, *869*(2), 107.

Menu, J., van Boekel, R., Henning, T., Leinert, C., Waelkens, C., & Waters, L. B. F. M. (2015). The structure of disks around intermediate-mass young stars from mid-infrared interferometry. Evidence for a population of group II disks with gaps. *Astronomy & Astrophysics*, *581*, Article A107, A107.

Miller, N., & Fortney, J. J. (2011). The heavy-element masses of extrasolar giant planets, revealed. *Astrophysical Journal Letters*, *736*(2).

Molaverdikhani, K., Henning, T., & Mollière, P. (2018). From cold to hot irradiated gaseous exoplanets: Toward an observation-based classification scheme. *The Astrophysical Journal*, *873*(1), 32.

Morales-Calderon, M., Stauffer, J. R., Kirkpatrick, J. D., Carey, S., Gelino, C. R., Barrado Y Nevascues, D., Rebull, L., Lowrance, P., Marley, M. S., Charbonneau, D., Patten, B., Megeath, S. T., & Buzasi, D. (2006). A Sensitive Search for Variability in Late L Dwarfs: The Quest for Weather. *The Astrophysical Journal*, *653*(4), 1454.

Morley, C. V., Fortney, J. J., Kempton, E. M., Marley, M. S., Vissher, C., & Zahnle, K. (2013). Quantitatively assessing the role of clouds in the transmission spectrum of GJ 1214b. *The Astrophysical Journal*, *775*(1), 33.

Morley, C. V., Fortney, J. J., Marley, M. S., Zahnle, K., Line, M., Kempton, E., Lewis, N., & Cahoy, K. (2015). Thermal emission and reflected light spectra of super earths with flat transmission spectra. *Astrophysical Journal*, *815*(2), 110.

Morley, C. V., Knutson, H., Line, M., Fortney, J. J., Thorngren, D., Marley, M. S., Teal, D., & Lupu, R. (2017). Forward and Inverse Modeling of the Emission and Transmission Spectrum of GJ 436b: Investigating Metal Enrichment, Tidal Heating, and Clouds. *The Astronomical Journal*, *153*(2), 86.

Mortier, A., Santos, N. C., Sousa, S. G., Adibekyan, V. Z., Delgado Mena, E., Tsantaki, M., Israelian, G., & Mayor, M. (2013). New and updated stellar parameters for 71 evolved planet hosts. *Astronomy & Astrophysics*, *557*, A70.

Moses, J. I., Line, M. R., Visscher, C., Richardson, M. R., Nettelmann, N., Fortney, J. J., Barman, T. S., Stevenson, K. B., & Madhusudhan, N. (2013). Compositional diversity in the atmospheres of hot neptunes, with application to GJ 436b. *The Astrophysical Journal*, *777*(1).

Moses, J. I., Madhusudhan, N., Visscher, C., & Freedman, R. S. (2013). Chemical consequences of the C/O ratio on hot jupiters: Examples from WASP-12b, CoRoT-2b, XO-1b, and HD 189733b. *The Astrophysical Journal*, *763*(1), 25.

Moses, J. I., Visscher, C., Fortney, J. J., Showman, A. P., Lewis, N. K., Griffith, C. A., Klippenstein, S. J., Shabram, M., Friedson, A. J., Marley, M. S., & Freedman, R. S. (2011). Disequilibrium Carbon, Oxygen, and Nitrogen Chemistry in the Atmospheres of HD 189733b and HD 209458b. *The Astrophysical Journal*, *737*, Article 15, 15.

Moses, J. I., Marley, M. S., Zahnle, K., Line, M. R., Fortney, J. J., Barman, T. S., Visscher, C., Lewis, N. K., & Wolff, M. J. (2016). On the Composition of Young, Directly Imaged Giant Planets. *The Astrophysical Journal*, *829*, Article 66, 66.

Moses, J. I. (2014). Chemical kinetics on extrasolar planets. *Philosophical Transactions of the Royal Society*, *A372*(2014), 20130073.

Niraula, P., Redfield, S., de Wit, J., Dai, F., Mireles, I., Serindag, D., & Shporer, A. (2018). Discovery of Six Optical Phase Curves with K2. *arXiv:1812.09227*.

Nomura, H., Tsukagoshi, T., Kawabe, R., Ishimoto, D., Okuzumi, S., Muto, T., Kanagawa, K. D., Ida, S., Walsh, C., Millar, T. J., & Bai, X.-N. (2016). ALMA Observations of a Gap and a Ring in the Protoplanetary Disk around TW Hya. *The Astrophysical Journal*, *819*(1), Article L7, L7.

Nugroho, S. K., Kawahara, H., Masuda, K., Hirano, T., Kotani, T., & Tajitsu, A. (2017). High-Resolution Spectroscopic Detection of TiO and Stratosphere in the Day-side of WASP-33b. *The Astronomical Journal*, *154*(6), 221.

Öberg, K. I., Murray-Clay, R., & Bergin, E. A. (2011). The effects of snowlines on C/O in planetary atmospheres. *Astrophysical Journal Letters*, *743*(1).

O'Donovan, F. T., Charbonneau, D., Harrington, J., Madhusudhan, N., Seager, S., Deming, D., & Knutson, H. A. (2010). Detection of planetary emission from the exoplanet TrES-2 using spitzer/IRAC. *The Astrophysical Journal*, *710*(2), 1551–1556.

Ohashi, S., & Kataoka, A. (2019). Radial Variations in Grain Sizes and Dust Scale Heights in the Protoplanetary Disk around HD 163296 Revealed by ALMA Polarization Observations. *The Astrophysical Journal*, *886*(2), Article 103, 103.

O'Rourke, J. G., Knutson, H. A., Zhao, M., Fortney, J. J., Burrows, A., Agol, E., Deming, D., Désert, J. M., Howard, A. W., Lewis, N. K., Showman, A. P., & Todorov, K. O. (2014). Warm spitzer and palomar near-ir secondary eclipse photometry of two hot jupiters: WASP-48b and HAT-P-23b. *The Astrophysical Journal*, *781*(2), 109.

Paardekooper, S.-J., & Mellema, G. (2006). Dust flow in gas disks in the presence of embedded planets. *Astronomy & Astrophysics*, *453*(3), 1129–1140.

Pairet, B., Cantalloube, F., & Jacques, L. (2021). MAYONNAISE: A morphological components analysis pipeline for circumstellar discs and exoplanets imaging in the near-infrared. *Monthly Notices of the Royal Astronomical Society*, *503*(3), 3724–3742.

Pál, A., Bakos, G. Á., Torres, G., Noyes, R. W., Fischer, D. A., Johnson, J. A., Henry, G. W., Butler, R. P., Marcy, G. W., Howard, A. W., Sipcz, B., Latham, D. W., & Esquerdo, G. A. (2010). Refined stellar, orbital and planetary parameters of the eccentric HAT-P-2 planetary system. *Monthly Notices of the Royal Astronomical Society*, *401*(4), 2665–2674.

Parmentier, V., Fortney, J. J., Showman, A. P., Morley, C. V., & Marley, M. S. (2016). Transitions in the cloud composition of hot Jupiters. *The Astrophysical Journal*, *828*(1), 1–19.

Pascucci, I., Testi, L., Herczeg, G. J., Long, F., Manara, C. F., Hendler, N., Mulders, G. D., Krijt, S., Ciesla, F., Henning, T., Mohanty, S., Drabek-Maunder, E., Apai, D., Szucs, L., Sacco, G., & Olofsson, J. (2016). A Steeper than Linear Disk Mass-Stellar Mass Scaling Relation. *The Astrophysical Journal*, *831*(2), Article 125, 125.

Pass, E. K., Cowan, N. B., Cubillos, P. E., & Sklar, J. G. (2019). Estimating dayside effective temperatures of hot Jupiters and associated uncertainties through Gaussian process regression. *Monthly Notices of the Royal Astronomical Society*, *489*(1), 941–950.

Pedregosa, F., Varoquaux, G., Gramfort, A., Michel, V., Thirion, B., Grisel, O., Blondel, M., Prettenhofer, P., Weiss, R., Dubourg, V., Vanderplas, J., Passos, A., Cournapeau, D., Brucher, M., Perrot, M., & Duchesnay, É. (2011). Scikit-learn: Machine Learning in Python. *J. Mach. Learn. Res.*, *12*, 2825–2830.

Perez-Becker, D., & Showman, A. P. (2013). Atmospheric heat redistribution on hot jupiters. *The Astrophysical Journal*, *776*(2), 134.

Pinilla, P., van der Marel, N., Pérez, L. M., van Dishoeck, E. F., Andrews, S., Birnstiel, T., Herczeg, G., Pontoppidan, K. M., & van Kempen, T. (2015). Testing particle trapping in transition disks with ALMA. *Astronomy & Astrophysics*, *584*, Article A16, A16.

Pinte, C., van der Plas, G., Ménard, F., Price, D. J., Christiaens, V., Hill, T., Mentiplay, D., Ginski, C., Choquet, E., Boehler, Y., Duchéne, G., Perez, S., & Casassus, S. (2019). Kinematic detection of a planet carving a gap in a protoplanetary disk. *Nature Astronomy*, *3*, 1109–1114.

Pollack, J. B., Hubickyj, O., Bodenheimer, P., Lissauer, J. J., Podolak, M., & Greenzweig, Y. (1996). Formation of the giant planets by concurrent accretion of solids and gas. *Icarus*, *124*(1), 62–85.

Pont, F., Zucker, S., & Queloz, D. (2006). The effect of red noise on planetary transit detection. *Monthly Notices of the Royal Astronomical Society*, *373*(1), 231–242.

Quiroz, J., Wallack, N. L., Ren, B., Dong, R., Xuan, J. W., Mawet, D., Millar-Blanchaer, M. A., & Ruane, G. (2022). Improving Planet Detection with Disk Modeling: Keck/NIRC2 Imaging of the HD 34282 Single-armed Protoplanetary Disk. *The Astrophysical Journal*, *924*(1), Article L4, L4.

Raymond, S. N., & Izidoro, A. (2017). Origin of water in the inner Solar System: Planetesimals scattered inward during Jupiter and Saturn's rapid gas accretion. *Icarus*, *297*, 134–148.

Reach, W. T., Megeath, S. T., Cohen, M., Hora, J., Carey, S., Surace, J., Willner, S. P., Barmby, P., Wilson, G., Glaccum, W., Lowrance, P., Marengo, M., & Fazio, G. G. (2005). Absolute Calibration of the Infrared Array Camera on the Spitzer Space Telescope. *Publications of the Astronomical Society of the Pacific*, *117*(835), 978–990.

Rice, W. K. M., Wood, K., Armitage, P. J., Whitney, B. A., & Bjorkman, J. E. (2003). Constraints on a planetary origin for the gap in the protoplanetary disc of GM Aurigae. *Monthly Notices of the Royal Astronomical Society*, *342*(1), 79–85.

Rich, E. A., Wisniewski, J. P., Mayama, S., Brandt, T. D., Hashimoto, J., Kudo, T., Kusakabe, N., Espaillat, C., Abe, L., Akiyama, E., Brandner, W., Carson, J. C., Currie, T., Egner, S., Feldt, M., Follette, K., Goto, M., Grady, C. A., Guyon, O., . . . Tamura, M. (2015). Near-IR Polarized Scattered Light Imagery of the DoAr 28 Transitional Disk. *The Astronomical Journal*, *150*(3), Article 86, 86.

Richardson, L. J., Deming, D., Horning, K., Seager, S., & Harrington, J. (2007). A spectrum of an extrasolar planet. *Nature*, *445*(7130), 892–895.

Rojas-Ayala, B., Covey, K. R., Muirhead, P. S., & Lloyd, J. P. (2012). Metallicity and temperature indicators in Mdwarf K-band spectra: Testing new and updated calibrations with observations of 133 solar neighborhood Mdwarfs. *The Astrophysical Journal*, *748*(2).

Rosenfeld, K. A., Andrews, S. M., Wilner, D. J., Kastner, J. H., & McClure, M. K. (2013). The Structure of the Evolved Circumbinary Disk around V4046 Sgr. *The Astrophysical Journal*, *775*(2), Article 136, 136.

Rosenfeld, K. A., Andrews, S. M., Wilner, D. J., & Stempels, H. C. (2012). A Disk-based Dynamical Mass Estimate for the Young Binary V4046 Sgr. *The Astrophysical Journal*, *759*(2), Article 119, 119.

Rostron, J. W., Wheatley, P. J., Anderson, D. R., Cameron, A. C., Fortney, J. J., Harrington, J., Knutson, H. A., & Pollacco, D. L. (2014). The thermal emission of the exoplanet WASP-3b. *Monthly Notices of the Royal Astronomical Society*, *441*(4), 3666–3678.

Ruane, G., Mawet, D., Kastner, J., Meshkat, T., Bottom, M., Femenía Castellá, B., Absil, O., Gomez Gonzalez, C., Huby, E., Zhu, Z., Jensen-Clem, R., Choquet, É., & Serabyn, E. (2017). Deep Imaging Search for Planets Forming in the TW Hya Protoplanetary Disk with the Keck/NIRC2 Vortex Coronagraph. *The Astronomical Journal*, *154*(2), Article 73, 73.

Ruane, G., Ngo, H., Mawet, D., Absil, O., Choquet, É., Cook, T., Gomez Gonzalez, C., Huby, E., Matthews, K., Meshkat, T., Reggiani, M., Serabyn, E., Wallack, N., & Xuan, W. J. (2019). Reference Star Differential Imaging of Close-in Companions and Circumstellar Disks with the NIRC2 Vortex Coronagraph at the W. M. Keck Observatory. *The Astronomical Journal*, *157*(3), Article 118, 118.

Ruffio, J.-B., Macintosh, B., Wang, J. J., Pueyo, L., Nielsen, E. L., De Rosa, R. J., Czekala, I., Marley, M. S., Arriaga, P., Bailey, V. P., Barman, T., Bulger, J., Chilcote, J., Cotten, T., Doyon, R., Duchéne, G., Fitzgerald, M. P., Follette, K. B., Gerard, B. L., . . . Wolff, S. (2017). Improving and Assessing Planet Sensitivity of the GPI Exoplanet Survey with a Forward Model Matched Filter. *The Astrophysical Journal*, *842*, Article 14, 14.

Santos, N. C., Sousa, S. G., Mortier, A., Neves, V., Adibekyan, V., Tsantaki, M., Delgado Mena, E., Bonfils, X., Israelian, G., Mayor, M., & Udry, S. (2013). SWEET-Cat: A catalogue of parameters for Stars With ExoplanETs. *Astronomy & Astrophysics*, *556*, A150.

Sato, B., Hartman, J. D., Bakos, G. Á., Béky, B., Torres, G., Latham, D. W., Kovács, G., Csubry, Z., Penev, K., Noyes, R. W., Buchhave, L. A., Quinn, S. N., Everett, M., Esquerdo, G. A., Fischer, D. A., Howard, A. W., Johnson, J. A., Marcy, G. W., Sasselov, D. D., . . . Sári, P. (2012). HAT-P-38b: A Saturn-Mass Planet Transiting a Late G Star. *Publications of the Astronomical Society of Japan*, *64*, Article 97, 97.

Schlaufman, K. C. (2018). Evidence of an Upper Bound on the Masses of Planets and its Implications for Giant Planet Formation. *The Astrophysical Journal*, *853*(1), 37.

Schwartz, J. C., & Cowan, N. B. (2015). Balancing the energy budget of short-period giant planets: Evidence for reflective clouds and optical absorbers. *Monthly Notices of the Royal Astronomical Society*, *449*(4), 4192–4203.

Schwartz, J. C., & Cowan, N. B. (2017). Knot a bad idea: Testing BLISS mapping for Spitzer Space Telescope photometry. *Publications of the Astronomical Society of the Pacific*, *129*(971), 1–20.

Schwartz, J. C., Kashner, Z., Jovmir, D., & Cowan, N. B. (2017). Phase offsets and the energy budgets of hot jupiters. *The Astrophysical Journal*, *850*(2), 154.

Seager, S., & Sasselov, D. D. (2000). Theoretical Transmission Spectra During Extrasolar Giant Planet Transits. *The Astrophysical Journal*, *10*, 916–921.

Sedaghati, E., Boffin, H. M., MacDonald, R. J., Gandhi, S., Madhusudhan, N., Gibson, N. P., Oshagh, M., Claret, A., & Rauer, H. (2017). Detection of titanium oxide in the atmosphere of a hot Jupiter. *Nature*, *549*(7671), 238–241.

Seeliger, M., Kitze, M., Errmann, R., Richter, S., Ohlert, J. M., Chen, W. P., Guo, J. K., Göğüş, E., Güver, T., Aydin, B., Mottola, S., Hellmich, S., Fernandez, M., Aceituno, F. J., Dimitrov, D., Kjurkchieva, D., Jensen, E., Cohen, D., Kundra, E., . . . Neuhäuser, R. (2015). Ground-based transit observations of the HAT-P-18, HAT-P-19, HAT-P-27/WASP40 andWASP-21 systems. *Monthly Notices of the Royal Astronomical Society*, *451*(4), 4060–4072.

Serabyn, E., Huby, E., Matthews, K., Mawet, D., Absil, O., Femenia, B., Wizinowich, P., Karlsson, M., Bottom, M., Campbell, R., Carlomagno, B., Defrère, D., Delacroix, C., Forsberg, P., Gomez Gonzalez, C., Habraken, S., Jolivet, A., Liewer, K., Lilley, S., . . . Wertz, O. (2017). The W. M. Keck Observatory Infrared Vortex Coronagraph and a First Image of HIP 79124 B. *The Astronomical Journal*, *153*(1), Article 43, 43.

Sheppard, K., Mandell, A. M., Tamburo, P., Gandhi, S., Pinhas, A., Madhusudhan, N., & Deming, D. (2017). Evidence for a Dayside Thermal Inversion and High Metallicity for the Hot Jupiter WASP-18b. *Astrophysical Journal Letters*, *850*(2), L32.

Showman, A. P., Lewis, N. K., & Fortney, J. J. (2015). 3D Atmospheric Circulation of Warm and Hot Jupiters. *The Astrophysical Journal*, *801*(2), Article 95, 95.

Shporer, A., O'Rourke, J. G., Knutson, H. A., Szabó, G. M., Zhao, M., Burrows, A., Fortney, J., Agol, E., Cowan, N. B., Desert, J. M., Howard, A. W., Isaacson, H., Lewis, N. K., Showman, A. P., & Todorov, K. O. (2014). Atmospheric characterization of the hot Jupiter Kepler-13Ab. *The Astrophysical Journal*, *788*(1), 92.

Sing, D. K., Fortney, J. J., Nikolov, N., Wakeford, H. R., Kataria, T., Evans, T. M., Aigrain, S., Ballester, G. E., Burrows, A. S., Deming, D., Désert, J. M., Gibson, N. P., Henry, G. W., Huitson, C. M., Knutson, H. A., Etangs, A. L. D., Pont, F., Showman, A. P., Vidal-Madjar, A., . . . Wilson, P. A. (2016). A continuum from clear to cloudy hot-Jupiter exoplanets without primordial water depletion. *Nature*, *529*(7584), 59–62.

Smith, A. M. S., Anderson, D. R., Madhusudhan, N., Southworth, J., Collier Cameron, A., Blecic, J., Harrington, J., Hellier, C., Maxted, P. F. L., Pollacco, D., Queloz, D., Smalley, B., Triaud, A. H. M. . J., & Wheatley, P. J. (2012). Thermal emission from WASP-24b at 3.6 and 4.5 μ m. *Astronomy & Astrophysics*, *545*(2014), A93.

Sousa, S. G., Adibekyan, V., Delgado-Mena, E., Santos, N. C., Andreasen, D. T., Ferreira, A. C. S., Tsantaki, M., Barros, S. C. C., Demangeon, O., Israelian, G., Faria, J. P., Figueira, P., Mortier, A., Brandao, I., Montalto, M., Rojas-Ayala, B., & Santerne, A. (2018). SWEET-Cat updated. New homogenous spectroscopic parameters. *Astronomy & Astrophysics*, *58*.

Southworth, J. (2008). Homogeneous studies of transiting extrasolar planets - I. Light-curve analyses. *Monthly Notices of the Royal Astronomical Society*, *386*(3), 1644–1666.

Southworth, J. (2009). Homogeneous studies of transiting extrasolar planets - II. Physical properties. *Monthly Notices of the Royal Astronomical Society*, *394*(1), 272–294.

Southworth, J. (2010). Homogeneous studies of transiting extrasolar planets - III. Additional planets and stellar models. *Monthly Notices of the Royal Astronomical Society*, *408*(3), 1689–1713.

Southworth, J. (2011). Homogeneous studies of transiting extrasolar planets - IV. Thirty systems with space-based light curves. *Monthly Notices of the Royal Astronomical Society*, *417*(3), 2166–2196.

Southworth, J. (2012). Homogeneous studies of transiting extrasolar planets - V. New results for 38 planets. *Monthly Notices of the Royal Astronomical Society*, *426*(2), 1291–1323.

Southworth, J., Mancini, L., Maxted, P. F., Bruni, I., Tregloan-Reed, J., Barbieri, M., Ruocco, N., & Wheatley, P. J. (2012). Physical properties and radius variations in the HAT-P-5 planetary system from simultaneous four-colour photometry. *Monthly Notices of the Royal Astronomical Society*, *422*(4), 3099–3106.

Steinrueck, M. E., Parmentier, V., Showman, A. P., Lothringer, J. D., Lupu, R. E., & Aug, E. P. (2019). The Effect of Disequilibrium Carbon Chemistry on the Atmospheric Circulation and Phase Curves of Hot Jupiter HD 189733b. *The Astrophysical Journal*, *880*(1), Article 14, 14.

Stetson, P. B. (1987). DAOPHOT: A Computer Program for Crowded-Field Stellar Photometry. *Publications of the Astronomical Society of the Pacific*, *99*, 191.

Stevenson, K. B., Harrington, J., Nymeyer, S., Madhusudhan, N., Seager, S., Bowman, W. C., Hardy, R. A., Deming, D., Rauscher, E., & Lust, N. B. (2010). Possible thermochemical disequilibrium in the atmosphere of the exoplanet GJ 436b. *Nature*, *464*(7292), 1161–1164.

Stevenson, K. B., Bean, J. L., Seifahrt, A., Gilbert, G. J., Line, M. R., Desert, J.-M., & Fortney, J. J. (2016). A Search for Water in the Atmosphere of HAT-P-26b Using LDSS-3C. *The Astrophysical Journal*, *817*(2), 141.

Stone, J. M., Skemer, A. J., Hinz, P. M., Bonavita, M., Kratter, K. M., Maire, A.-L., Defrere, D., Bailey, V. P., Spalding, E., Leisenring, J. M., Desidera, S., Bonnefoy, M., Biller, B., Woodward, C. E., Henning, T., Skrutskie, M. F., Eisner, J. A., Crepp, J. R., Patience, J., . . . Bass, B. (2018). The LEECH Exoplanet Imaging Survey: Limits on Planet Occurrence Rates under Conservative Assumptions. *The Astronomical Journal*, *156*(6), Article 286, 286.

Szulágyi, J., Dullemond, C. P., Pohl, A., & Quanz, S. P. (2019). Observability of forming planets and their circumplanetary discs II. - SEDs and near-infrared fluxes. *Monthly Notices of the Royal Astronomical Society*, *487*(1), 1248–1258.

Teague, R., Bae, J., Bergin, E. A., Birnstiel, T., & Foreman-Mackey, D. (2018). A Kinematical Detection of Two Embedded Jupiter-mass Planets in HD 163296. *The Astrophysical Journal*, *860*(1), Article L12, L12.

Terrien, R. C., Mahadevan, S., Deshpande, R., & Bender, C. F. (2015). A near-infrared spectroscopic survey of 886 nearby M dwarfs. *Astrophysical Journal Supplement Series*, *220*(1), 16.

Terrien, R. C., Mahadevan, S., Bender, C. F., Deshpande, R., Ramsey, L. W., & Bochanski, J. J. (2012). AN H-band spectroscopic metallicity calibration for M dwarfs. *Astrophysical Journal Letters*, *747*(2).

Teske, J. K., Thorngren, D., Fortney, J. J., Hinkel, N., & Brewer, J. M. (2019). Do Metal-rich Stars Make Metal-rich Planets? New Insights on Giant Planet Formation from Host Star Abundances. *The Astronomical Journal*, *158*(6), 239.

Testi, L., Natta, A., Shepherd, D. S., & Wilner, D. J. (2003). Large grains in the disk of CQ Tau. *Astronomy & Astrophysics*, *403*, 323–328.

Gaia Collaboration, Brown, A. G. A., Vallenari, A., Prusti, T., de Bruijne, J. H. J., Babusiaux, C., Biermann, M., Creevey, O. L., Evans, D. W., Eyer, L., & et al. (2021). Gaia Early Data Release 3. Summary of the contents and survey properties. *Astronomy & Astrophysics*, *649*, Article A1, A1.

Thorngren, D. P., & Fortney, J. J. (2018). Bayesian Analysis of Hot Jupiter Radius Anomalies: Evidence for Ohmic Dissipation? *The Astronomical Journal*, *155*(5), 214.

Thorngren, D. P., & Fortney, J. J. (2019). Connecting Giant Planet Atmosphere and Interior Modeling: Constraints on Atmospheric Metal Enrichment. *The Astrophysical Journal Letters*, *874*(2), L31.

Thorngren, D. P., Fortney, J. J., Murray-Clay, R. A., & Lopez, E. D. (2016). The Mass-Metallicity Relation for Giant Planets. *The Astrophysical Journal*, *831*(1), 1–14.

Todorov, K. O., Deming, D., Burrows, A., & Grillmair, C. J. (2014). Updated Spitzer emission spectroscopy of bright transiting hot Jupiter HD 189733b. *The Astrophysical Journal*, *796*(2), 100.

Todorov, K. O., Deming, D., Harrington, J., Stevenson, K. B., Bowman, W. C., Nymeyer, S., Fortney, J. J., & Bakos, G. A. (2010). Spitzer IRAC secondary eclipse photometry of the transiting extrasolar planet HAT-P-1b. *The Astrophysical Journal*, *708*(1), 498–504.

Todorov, K. O., Deming, D., Knutson, H. A., Burrows, A., Sada, P. V., Cowan, N. B., Agol, E., Desert, J. M., Fortney, J. J., Charbonneau, D., Laughlin, G., Langton, J., Showman, A. P., & Lewis, N. K. (2012). Warm Spitzer observations of three hot exoplanets: XO-4b, HAT-P-6b, and HAT-P-8b. *The Astrophysical Journal*, *746*(1), 111.

Todorov, K. O., Deming, D., Knutson, H. A., Burrows, A., Fortney, J. J., Lewis, N. K., Cowan, N. B., Agol, E., Desert, J. M., Sada, P. V., Charbonneau, D., Laughlin, G., Langton, J., & Showman, A. P. (2013). Warm Spitzer photometry of three hot Jupiters: HAT-P-3b, HAT-P-4b and HAT-P-12b. *The Astrophysical Journal*, *770*(2), 102.

Torres, G., Winn, J. N., & Holman, M. J. (2008). Improved Parameters for Extrasolar Transiting Planets. *The Astrophysical Journal*, *677*(2), 1324–1342.

Torres, G., Fischer, D. A., Sozzetti, A., Buchhave, L. A., Winn, J. N., Holman, M. J., & Carter, J. A. (2012). Improved spectroscopic parameters for transiting planet hosts. *The Astrophysical Journal*, *757*(2).

Triaud, A. H., Gillon, M., Ehrenreich, D., Herrero, E., Lendl, M., Anderson, D. R., Cameron, A. C., Delrez, L., Demory, B. O., Hellier, C., Heng, K., Jehin, E., Maxted, P. F., Pollacco, D., Queloz, D., Ribas, I., Smalley, B., Smith, A. M., & Udry, S. (2015). WASP-80b has a dayside within the T-dwarf range. *Monthly Notices of the Royal Astronomical Society*, *450*(3), 2279–2290.

Ubeira Gabellini, M. G., Miotello, A., Facchini, S., Ragusa, E., Lodato, G., Testi, L., Benisty, M., Bruderer, S., T. Kurtovic, N., Andrews, S., Carpenter, J., Corder, S. A., Dipierro, G., Ercolano, B., Fedele, D., Guidi, G., Henning, T., Isella, A., Kwon, W., . . . Wilner, D. (2019). A dust and gas cavity in the disc around CQ Tau revealed by ALMA. *Monthly Notices of the Royal Astronomical Society*, *486*(4), 4638–4654.

Uyama, T., Ren, B., Mawet, D., Ruane, G., Bond, C. Z., Hashimoto, J., Liu, M. C., Muto, T., Ruffio, J.-B., Wallack, N., Baranec, C., Bowler, B. P., Choquet, E., Chun, M., Delorme, J.-R., Fogarty, K., Guyon, O., Jensen-Clem, R., Meshkat, T., . . . Zuckerman, B. (2020). Early High-contrast Imaging Results with Keck/NIRC2-PWFS: The SR 21 Disk. *The Astronomical Journal*, *160*(6), Article 283, 283.

van der Marel, N., van Dishoeck, E. F., Bruderer, S., Andrews, S. M., Pontoppidan, K. M., Herczeg, G. J., van Kempen, T., & Miotello, A. (2016). Resolved gas cavities in transitional disks inferred from CO isotopologs with ALMA. *Astronomy & Astrophysics*, *585*, Article A58, A58.

van der Marel, N., Dong, R., di Francesco, J., Williams, J. P., & Tobin, J. (2019). Protoplanetary Disk Rings and Gaps across Ages and Luminosities. *The Astrophysical Journal*, *872*(1), Article 112, 112.

van der Plas, G., Ménard, F., Canovas, H., Avenhaus, H., Casassus, S., Pinte, C., Caceres, C., & Cieza, L. (2017). An 80 au cavity in the disk around HD 34282. *Astronomy & Astrophysics*, *607*, Article A55, A55.

Villenave, M., Stapelfeldt, K. R., Duchéne, G., Ménard, F., Lambrechts, M., Sierra, A., Flores, C., Dent, W. R. F., Wolff, S., Ribas, Á., Benisty, M., Cuello, N., & Pinte, C. (2022). A Highly Settled Disk around Oph163131. *The Astrophysical Journal*, *930*(1), Article 11, 11.

Visscher, C., Lodders, K., & Fegley, B., Jr. (2010). Atmospheric Chemistry in Giant Planets, Brown Dwarfs, and Low-mass Dwarf Stars. III. Iron, Magnesium, and Silicon. *The Astrophysical Journal*, *716*, 1060–1075.

Wakeford, H. R., Sing, D. K., Kataria, T., Deming, D., Nikolov, N., Lopez, E. D., Tremblin, P., Amundsen, D. S., Lewis, N. K., Mandell, A. M., Fortney, J. J., & Knutson, H. (2017). Heavy Element Abundance. *Science*, *356*(May), 628–631.

Wallack, N. L., Knutson, H. A., Morley, C. V., Moses, J. I., Thomas, N. H., Thorngren, D. P., Deming, D., Désert, J.-M., Fortney, J. J., & Kammer, J. A. (2019). Investigating Trends in Atmospheric Compositions of Cool Gas Giant Planets Using Spitzer Secondary Eclipses. *The Astronomical Journal*, *158*(6), 217. https://doi.org/10.3847/1538-3881/ab2a05.

Wang, J. J., Ruffio, J.-B., De Rosa, R. J., Aguilar, J., Wolff, S. G., & Pueyo, L. (2015). pyKLIP: PSF Subtraction for Exoplanets and Disks.

Wang, J. J., Ginzburg, S., Ren, B., Wallack, N., Gao, P., Mawet, D., Bond, C. Z., Cetre, S., Wizinowich, P., De Rosa, R. J., Ruane, G., Liu, M. C., Absil, O., Alvarez, C., Baranec, C., Choquet, É., Chun, M., Defrère, D., Delorme, J.-R., . . . Zuckerman, B. (2020). Keck/NIRC2 L'-band Imaging of Jovian-mass Accreting Protoplanets around PDS 70. *The Astronomical Journal*, *159*(6), Article 263, 263.

Wang, S., Kanagawa, K. D., & Suto, Y. (2021). Architecture of Planetary Systems Predicted from Protoplanetary Disks Observed with ALMA. I. Mass of the Possible Planets Embedded in the Dust Gap. *The Astrophysical Journal*, *923*(2), Article 165, 165.

Weidenschilling, S. J. (1977). Aerodynamics of solid bodies in the solar nebula. *Monthly Notices of the Royal Astronomical Society*, *180*, 57–70.

Wheatley, P. J., Cameron, A. C., Harrington, J., Fortney, J. J., Simpson, J. M., Anderson, D. R., Smith, A. M. S., Aigrain, S., Clarkson, W. I., Gillon, M., Haswell, C. A., Hebb, L., Hébrard, G., Hellier, C., Hodgkin, S. T., Horne, K. D., Kane, S. R., Maxted, P. F. L., Norton, A. J., . . . Wilson, D. M. (2010). The thermal emission of the exoplanets WASP-1b and WASP-2b. *arXiv:1004.0836*, (April).

Wölfer, L., Facchini, S., Kurtovic, N. T., Teague, R., van Dishoeck, E. F., Benisty, M., Ercolano, B., Lodato, G., Miotello, A., Rosotti, G., Testi, L., & Ubeira Gabellini, M. G. (2021). A highly non-Keplerian protoplanetary disc. Spiral structure in the gas disc of CQ Tau. *Astronomy & Astrophysics*, *648*, Article A19, A19.

Wong, I., Knutson, H. A., Kataria, T., Lewis, N. K., Burrows, A., Fortney, J. J., Schwartz, J., Shporer, A., Agol, E., Cowan, N. B., Deming, D., Désert, J.-M., Fulton, B. J., Howard, A. W., Langton, J., Laughlin, G., Showman, A. P., & Todorov, K. (2016). 3.6 AND 4.5 μ m Spitzer Phase Curves of the Highly-Irradiated Hot Jupiters WASP-19b and HAT-P-7b. *The Astrophysical Journal*, *823*(2), 122.

Xuan, W. J., Mawet, D., Ngo, H., Ruane, G., Bailey, V. P., Choquet, É., Absil, O., Alvarez, C., Bryan, M., Cook, T., Femenía Castellá, B., Gomez Gonzalez, C., Huby, E., Knutson, H. A., Matthews, K., Ragland, S., Serabyn, E., & Zawol, Z. (2018). Characterizing the Performance of the NIRC2 Vortex Coronagraph at W. M. Keck Observatory. *The Astronomical Journal*, *156*(4), Article 156, 156.

Zhang, K., Isella, A., Carpenter, J. M., & Blake, G. A. (2014). Comparison of the Dust and Gas Radial Structure in the Transition Disk [PZ99] J160421.7-213028. *The Astrophysical Journal*, *791*(1), Article 42, 42.

Zhang, S., Zhu, Z., Huang, J., Guzmán, V. V., Andrews, S. M., Birnstiel, T., Dullemond, C. P., Carpenter, J. M., Isella, A., Pérez, L. M., Benisty, M., Wilner, D. J., Baruteau, C., Bai, X.-N., & Ricci, L. (2018). The Disk Substructures at High Angular Resolution Project (DSHARP). VII. The Planet-Disk Interactions Interpretation. *The Astrophysical Journal*, *869*(2), Article L47, L47.

Zhao, M., O'Rourke, J. G., Wright, J. T., Knutson, H. A., Burrows, A., Fortney, J., Ngo, H., Fulton, B. J., Baranec, C., Riddle, R., Law, N. M., Muirhead, P. S., Hinkley, S., Showman, A. P., Curtis, J., & Burruss, R. (2014). Characterization of the atmosphere of the hot Jupiter HAT-P-32Ab and the M-Dwarf companion HAT-P-32B. *The Astrophysical Journal*, *796*(2), 115.

Zhu, Z. (2015). Accreting Circumplanetary Disks: Observational Signatures. *The Astrophysical Journal*, *799*(1), Article 16, 16.

Zhu, Z., Stone, J. M., Rafikov, R. R., & Bai, X.-n. (2014). Particle Concentration at Planet-induced Gap Edges and Vortices. I. Inviscid Three-dimensional Hydro Disks. *The Astrophysical Journal*, *785*(2), Article 122, 122.